Dissertation
submitted to the
Combined Faculties for the Natural Sciences and for Mathematics
of the Ruperto-Carola University of Heidelberg, Germany
for the degree of
Doctor of Natural Sciences

presented by
Diplom-Phys.: Anant Eungwanichayapant
born in: Khon Kaen, Thailand
Oral examination: 2.7.2003

Giant Pair Halos Surrounding
Non-Thermal Extragalactic Objects

Referees: **Prof. Dr. Heinrich J. Völk**
Prof. Dr. Stefan Wagner

Abstract

Very high energy ($E > 100$ GeV) gamma-rays from extragalactic sources are absorbed via $\gamma\gamma$ pair production on the cosmic infrared background (CIB) and initiate electromagnetic cascades involving pair production and inverse Compton interactions. This leads to the formation of an electron-positron pair halo, whose particle distribution is isotropic if a sufficiently strong intergalactic magnetic field ($|\mathrm{B}| > 1$ nG) is present.

In this work, a Monte Carlo method has been adopted. The pair halo energy and angular distributions for many different parameters such as injected distributions, CIB models and red shifts have been studied.

A key result is that the pair halo energy and angular distributions are sensitive to the primary gamma photon energies only up to a certain limit, above which the photons interact with the cosmic microwave background. Also, it is found that at low red shift the spectrum of the CIB has a stronger influence on the pair halo energy distributions than on their angular distributions. For sources at high red shift, pair halo modelling of the angular distribution can be used as indirect means of probing the CIB intensity.

The detection possibility of the pair halo from H1426+428 is also discussed.

Kurzfassung

Hochenergetische ($E > 100\,\mathrm{GeV}$) Gammastrahlen aus extragalaktischen Quellen werden infolge der $\gamma\gamma$-Paarbildung von der kosmischen Infrarot-Hintergrundstrahlung (CIB) absorbiert und lösen elektromagnetische Schauer durch Paarbildung und inverse Comptonstreuung aus. Dies führt zur Ausbildung eines Elektron-Positron-Paarhalos, dessen Teilchenverteilung isotrop ist, falls ein genügend starkes intergalaktisches Magnetfeld ($|B| > 1\,\mathrm{nG}$) vorhanden ist.

In dieser Arbeit wird eine Monte-Carlo Methode angewandt, bei der die Paarhalo-Energie und Winkelverteilungen für viele verschiedene Parameter (einlaufende Teilchenverteilungen, CIB-Modelle und Rotverschiebungen) untersucht werden.

Ein wichtiges Ergebnis ist der Nachweis einer Grenze der Empfindlichkeit der Paarhalo-Energie und der Winkelverteilungen auf die primären Gamma-Energien, oberhalb derer die Photonen mit der kosmischen Mikrowellen-Hintergrundstrahlung wechselwirken. Ausserdem wird gefunden, dass bei geringer Rotverschiebung das Spektrum des CIB einen stärkeren Einfluss auf die Paarhalo-Energie als auf die Winkelverteilungen hat. Für Quellen mit hoher Rotverschiebung kann ein Modellieren der Winkelverteilungen als indirektes Mittel zur Untersuchung der CIB Intensität dienen.

Der mögliche Nachweis eines Paarhalos aus der Quelle H14236+428 wird diskutiert.

Acknowledgments

First of all I would like to thank Prof. Heinrich J. Völk for giving me the opportunity to work in his group. There was a very good atmosphere in the group which made it nice and easy for me to adjust to the new environment. I am also appreciating for all of his advice on my work.

Next I am very indebted to my advisor Felix Aharonian who gave me a very interesting research topic. I am very proud to have worked with him. His great advice was very practical and played an essential role in my work. I have learned many things from my discussions with him. His warm encouragement and suggestions about my scientific life impressed me very much.

My special thank go to Dieter Horns who provided me with very valuable and significant advice on many parts of my work. He is the first person that I would consult with if I ever meet some difficulties in my work.

I also owe my gratitude to Alexander Konopelko who gave me practical advice in the Monte Carlo method.

I really appreciate that Olaf Skjæraasen, Jim Hinton and Conor Masterson helped me with my English many times. I am very lucky that I have very nice friends such as them.

Furthermore I am thankful that Luigi Costamante made a beautiful diagram of the pair halo model and that Gavin Rowell corrected my summary.

I would like to thank Andreas Heusler who help me to translate my abstract from English to German.

Beside I want to thank Joel R.Primack, James S. Bullock and T. M. Kneiske for providing cosmic infrared background data.

Last but not least I thank SFB 439 for their financial support.

Contents

Chapter 1

Introduction

It has been known since 1962 [Nik62] that the intergalactic medium (IGM) is opaque for very high energy (VHE[1]) extragalactic gamma photons. For $E_\gamma > 100$ TeV, the absorption of these photons is primarily due to the 2.7 K cosmic microwave background radiation (CMB) via $\gamma\gamma \rightarrow e^- e^+$ pair production [GS67], hereafter denoted PP. For $E_\gamma < 100$ TeV the absorption caused by the infrared/optical background or cosmic infrared background (CIB) can not be neglected [WTW72, SJS92]. Thus, VHE photons, emitted at a sufficiently large distance to the observer, will inevitably be absorbed.

Whenever a VHE photon is absorbed via PP, the resulting electron-positron ($e^\pm$) pair can interact with the soft photon background via inverse Compton scattering (IC) and produce secondary gamma photons. These secondary photons can be PP absorbed by the same background to create more $e^\pm$ pairs if they are sufficiently energetic. The tandem processes of PP and IC are referred to as an *electromagnetic cascade*. The cascade develops until the Compton upscattered photon can no longer be PP absorbed. The electromagnetic cascade converts one gamma photon into a number of gamma photons with much lower energy. Since the IGM is transparent for these lower-energy gamma photons, they can propagate freely from the source to the observer.

When the intergalactic magnetic field is taken into account, there are two cases of the cascades that can be distinguished by the relation of the gyroradius (R_{gyro}) to the IC mean free path (Λ_{IC}). When $R_{gyro} \gg \Lambda_{IC}$, the cascade develops linearly along the line of sight between the source and the observer [WC96, Hor00]. The other case is when $R_{gyro} \ll \Lambda_{IC}$: the cascaded $e^\pm$s are trapped in a certain region and isotropically emit secondary photons. Actually, this second case can be divided into two sub-cases. One is when the magnetic field is strong : $|\mathbf{B}| > 10^{-6}$ G. In such a high magnetic field the synchrotron cooling rate is comparable to the Compton cooling rate. Since the $e^\pm$s are cooled by both interactions, the cascade can proceed only to several generations [KK03]. In the other case, which is the topic of this work, the magnetic field is of moder-

[1] VHE gamma photon: $E_\gamma > 100$ GeV

ate strength ($10^{-9} < |\mathbf{B}| < 10^{-6}$ G). The synchrotron cooling rate can then be neglected and only the Compton cooling is taken into account. The pairs produced are trapped immediately, isotropize, and isotropically upscatter ambient soft photons to gamma photons [ACV94]. The upscattered photons produce 2nd-generation $e^{\pm}$s which are also trapped and in turn upscatter ambient soft photons initiating electromagnetic cascades. Thus, after the development of a cascade, this scenario leads to the formation of a quasi-spherical $e^{\pm}$ pair halo around the VHE primary gamma source. The important observable quantities are the energy distribution and the angular distribution of the cascade gamma photons.

Observing the gamma photons from the $e^{\pm}$ pair halo is promising for modern VHE gamma-rays astronomy especially from ground-based observatories. In the next section a review[2] of the ground-based VHE gamma-ray astronomy will be presented.

1.1 VHE gamma-ray Astronomy

Ground-based gamma-ray astronomy began in 1948 when Blackett [Bla48] suggested that Čerenkov radiation from cosmic rays would make up for a small fraction of the night sky light. The idea was followed five years later with Galbraith & Jelley [GJ53] observing optical pulses coincident with signals from a Geiger-counter array, confirming the association with cosmic-ray-induced air showers. In 1958, Morrison [Mor58] provided the first arguments for searching for cosmic gamma-rays. Cocconi [Coc60] carried this further with an estimate of the flux of TeV gamma photons from the Crab nebula which was a thousand times higher than the upper limit from the observations by the Crimean group led by Chudakov [C$^+$65]. In 1968, Fazio, Helmken, Rieke & Weekes [F$^+$68] finished the construction of the first high-quality, 10-meter-diameter Čerenkov telescope at Mt. Hopkins in southern Arizona.

In 1977, Turver&Weekes [TW78] used Monte Carlo calculations of air showers initiated by gamma-rays and protons to demonstrate that imaging might provide a new technique for discrimination between the two species. In 1985, Hillas [Hil85] showed that image characterization would substantially enhance gamma-ray signals relative to the hadronic background. He suggested a very powerful method by using the second moment of the air-shower image intensity to distinguish those which were both narrow and aligned with respect to the known source direction. In 1989, the Whipple Collaboration [W$^+$89] by using a 37 pixel camera reported the detection of the Crab nebula with a 9-σ significance. Two years later a 20-σ gamma-ray signal from the Crab nebula using a 109 pixel camera was reported [V$^+$91].

The important developments in VHE gamma-ray astronomy came not only from the ground-based telescopes, but also from space telescopes. In 1991, the Compton Gamma-Ray Observatory (CGRO) which contains among other experiment the Energetic Gamma Ray Experiment Telescope (EGRET) was

[2]The historical part of this review is mostly based on [AA97].

launched. More than 270 identified and unidentified gamma ray sources have been observed and summarized in EGRET catalogues [F$^+$94, T$^+$95, H$^+$99]. The EGRET observational results increase the number of possible targets for ground-based observations. There are several sources, for example Mkn421, that have been detected by both EGRET [L$^+$92] and ground-based gamma-ray telescopes [P$^+$92]. However, most of the gamma-ray sources that have been discovered by EGRET have not been detected in the TeV energy range. Some sources were discovered by ground-based gamma-ray telescopes first and later on found in EGRET observations (for example Mkn501 by the Whipple Collaboration [Q$^+$96]).

Another development of the ground-based gamma-ray telescope is the stereoscopic observation technique with an array of gamma-ray telescopes. This technique, first extensively explored by the HEGRA group (see e.g., [D$^+$97]), will be used for the next generation of ground-based observatories such as H.E.S.S. [A$^+$97a], CANGAROO-III [Mor00], VERITAS [O$^+$03], and presumably also MAGIC [Mir02].

Up to now more than ten TeV gamma-ray sources are known. Except for one unidentified object (Cygnus OB2 [A$^+$02b]), all objects are associated with known Galactic and extra-galactic sources like BL Lacertae (BL Lac) type object, shell-type supernova remnants, plerions, etc. Fig. 1.1 presents these TeV sources together with the gamma sources found by EGRET.

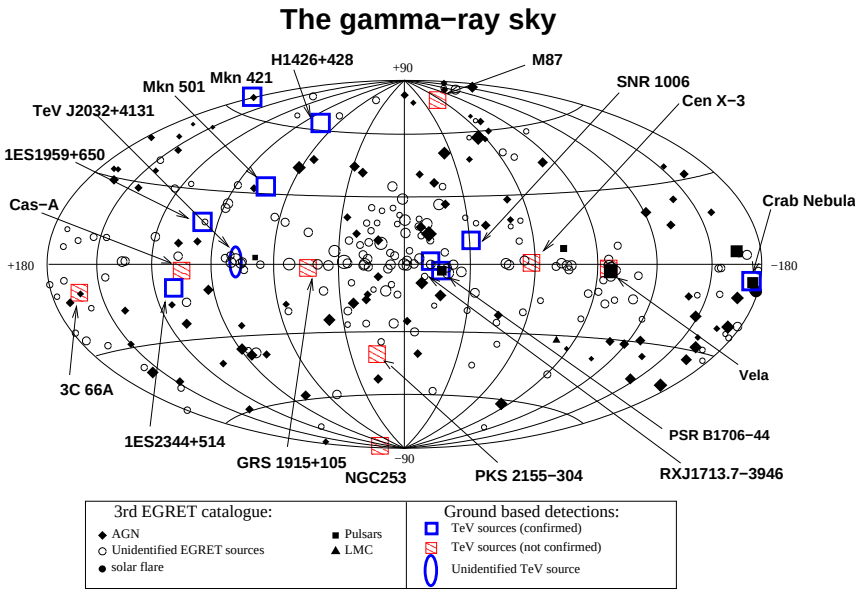

Figure 1.1: All sky gamma-ray sources. Courtesy Dieter Horns.

1.1.1 Extensive Air Showers

Ground-based gamma-ray observations detect extensive air showers that develop in the Earth's atmosphere. The two different types of air showers which can be classified with respect to the initiating particles are gamma-ray and cosmic-ray air showers. The gamma-rays initiate the cascades via PP in the electric field of the nuclei and electrons in the atmosphere, producing the $e^{\pm}$ pairs which in turn generate high energy photons by Bremsstrahlung. The Bremsstrahlung photons behave like the primary gamma photons producing the $e^{\pm}$. The two interaction processes sustain an electromagnetic cascade which is called gamma-ray air shower. The products from the gamma-ray air shower are mainly photons and electrons which differ from the cosmic-ray air showers described in the next paragraph.

For cosmic-ray induced air-showers, the cascade is initiated by high energy cosmic-rays. The showers are started by the cosmic-ray collisions with atmospheric matter. The main products from the collisions are some nuclear particles and π-mesons. The nuclear particles continue the cascade while the π-mesons will mainly decay into muons and neutrinos:

$$\pi^0 \rightarrow 2\gamma, \tag{1.1}$$

$$\pi^+ \rightarrow \mu^+ + \nu_\mu, \tag{1.2}$$

$$\pi^- \rightarrow \mu^- + \overline{\nu}_\mu. \tag{1.3}$$

Subsequently, $\mu^{+(-)}$ from $\pi^{+(-)}$ decay produce electrons (and muon neutrinos)

$$\mu^+ \rightarrow e^+ + \nu_e + \overline{\nu}_\mu, \tag{1.4}$$

$$\mu^- \rightarrow e^- + \overline{\nu}_e + \nu_\mu. \tag{1.5}$$

The gamma photons from π^0-decay and the $e^{\pm}$ from $\pi^{\pm}$ form electromagnetic cascades. Whereas the electromagnetic cascades produce a number of $e^{\pm}$ pairs, the nucleonic cascades produce a number of muons. The muons from the nucleonic cascades can travel from the atmosphere to the Earth's surface, even though the mean lifetime of muons is very short (2.2×10^{-6} s), because of relativistic time dilation. Also they have virtually no nuclear interaction and their ionization losses are small. One can show that muons with a Lorentz factor of about 20 can travel more than 10 km before they decay. Therefore, for cosmic-ray showers, muons can be observed by the observers on the Earth. Figure 1.2 shows schematic diagrams for both gamma-ray showers and cosmic-ray showers.

There are some differences between the gamma-rays and cosmic-ray showers. Cosmic-ray showers are much wider than the gamma-ray ones because of the transverse momentum given to pions in strong interactions. Another major difference is that cosmic-ray showers produce a number of muons which can penetrate to the ground.

1.1.2 Čerenkov imaging method

Čerenkov light is emitted in a dielectric medium when a charged particle with ve-

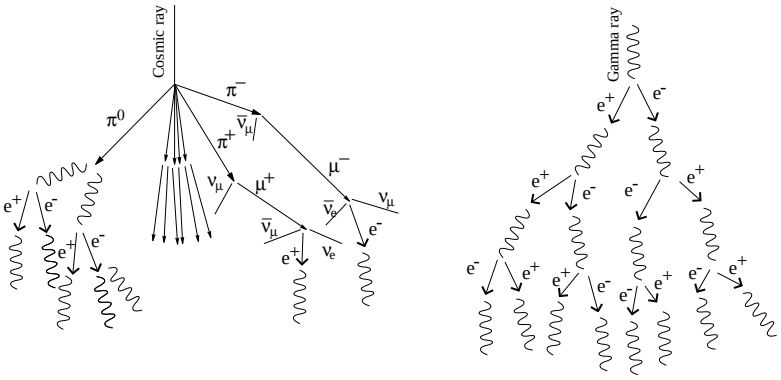

Figure 1.2: This diagram shows a cosmic-ray shower and a gamma-ray shower in the atmosphere.

locity faster than the local speed of light passes through the medium. The form of Čerenkov light emission is analogous to the acoustic shock wave produced by a supersonic aircraft. Fig. 1.3 shows Huygens' construction for determining the direction of propagation of the wavefront of Čerenkov light. The Čerenkov light is emitted at angle θ with respect to the velocity direction of the fast charged particle. The emitting angle can be determined:

$$\cos\theta = \frac{1}{n\beta}, \tag{1.6}$$

where $\beta = v/c$ is the velocity of the particle (relative to speed of light) and n in the refractive index of the medium.

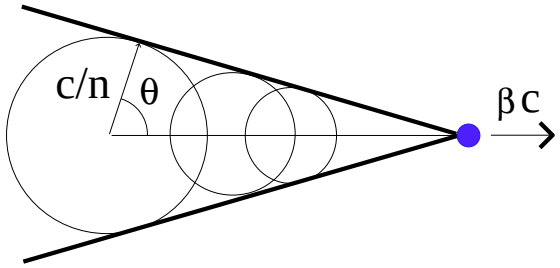

Figure 1.3: This diagram shows the Huygens's picture of Čerenkov emission.

Both cosmic-ray and gamma-ray showers generate high energy charged particles which emit Čerenkov light along the track of the charged particles. The Čerenkov light flash lasts only a few nano-seconds and is intense enough to be observed against the night sky background light [Bla48, GJ53]. Fig. 1.4 shows

the showers and corresponding Čerenkov images in the telescope. A Čerenkov image of the cosmic-ray shower is much wider and more diffuse than the gamma-ray initiated shower image.

The shower Čerenkov images can be parameterized by the second moments and positional angle of the centroid. It has been found [Hil85] that the simple description of the image by using the parameters width, length, orientation, and angular distance from the object observed, combined with possibly other features (compactness) is sufficient to reject most of the background images not due to gamma-rays. The widely used parameters of shower images are presented in Fig 1.5.

Using the shower images from the Čerenkov light is an effective method to exclude the dominant background of cosmic-ray induced air showers. In this way, more than 95% of cosmic-ray showers are rejected[Hil96].

Stereoscopic systems using more than one telescope to observe the same shower in coincidence can filter out the background more effectively than a single telescope. The unambiguous reconstruction of the shower geometry (core position, arrival direction, and position of the shower maximum) for individual events improves the rejection of hadrons, allows gamma-ray spectroscopy with the very good energy resolution ($\Delta E/E \approx 10$ %), and allows to control systematic effects much better.

1.1.3 H.E.S.S.

The High Energy Stereoscopic System (H.E.S.S.) is one of the next generation ground-based gamma-ray telescope array systems. The name H.E.S.S. was chosen in honor of Victor Hess who discovered cosmic radiation in 1912 and received the Nobel Prize in 1936 for his discovery [Hes12]. H.E.S.S. is located near the Gamsberg in the Namibian Khomas highlands at a distance of about 100 km from Windhoek, the capital of Namibia, (23°16′18″ S, 16°30′00″ E) at 1800 m altitudes. H.E.S.S. is one of the two ground-based Čerenkov telescope arrays located in the southern hemisphere.

In the initial phase H.E.S.S. consists of 4 telescopes whereas the second phase will include as many as 16 telescopes. The four telescopes of the first phase are located at the corners of a square area with a side length of about 120 m. The area covered by the telescopes of 120×120 m^2 is comparable to the size of the typical Čerenkov light pool. The first phase is expected to be completed in 2003. The first telescope has already been operated since June 2002.

Each telescope has a mirror dish with a diameter of more than 12 m and 380 individual glass mirrors. Each mirror reflects the light to the camera which is located in the focal plane at a distance of 15 m to the dish [Bo03, C$^+$03]. The telescopes are mounted on a circular rail of $\sim$15 m diameter and can rotate around the vertical axis. It takes one to three minutes to slew the telescope from the parking position to an arbitrary position in the sky. Figure 1.7 shows gamma-ray telescopes in the first phase of H.E.S.S.

The camera converts the light into a digital signal with photomultiplier tubes (PMTs) and a sophisticated electronic read-out chain. The camera has 960

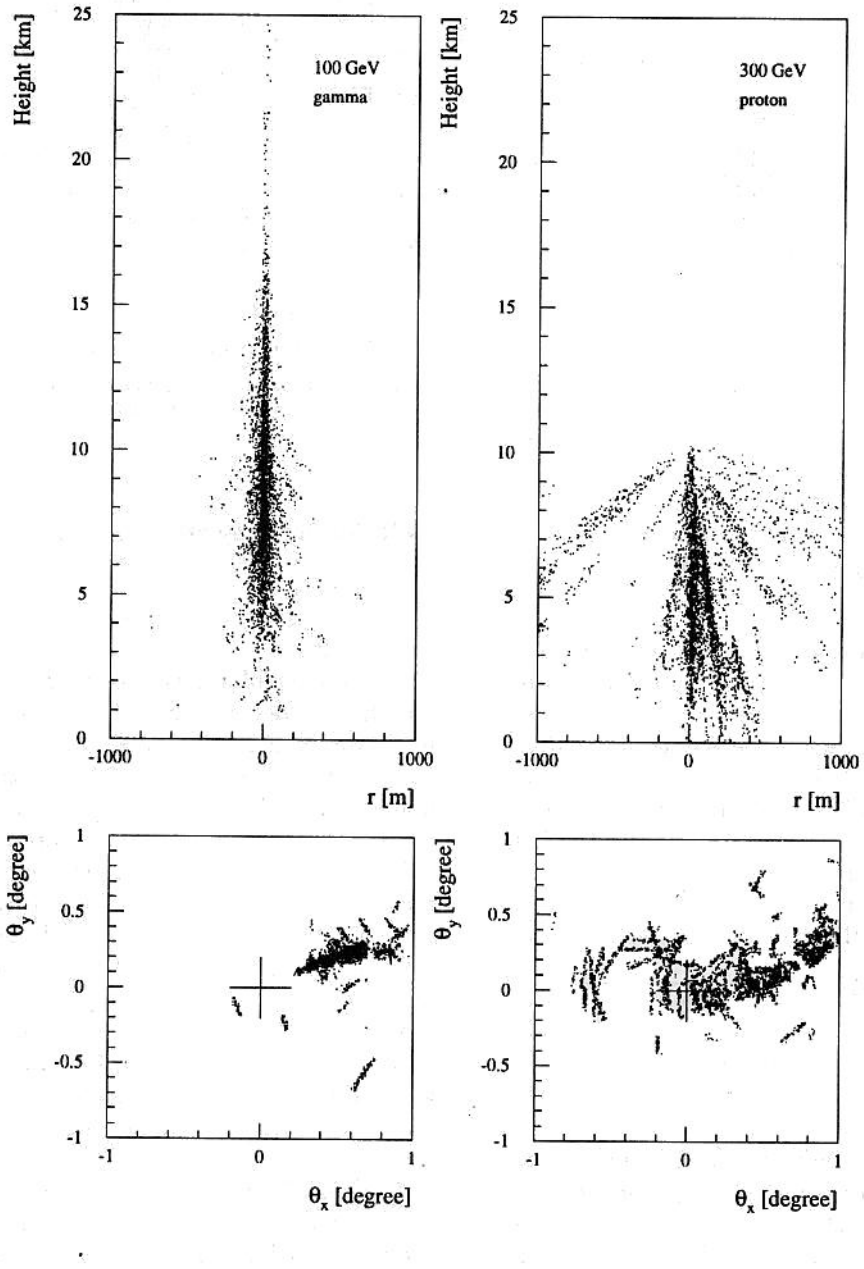

Figure 1.4: The longitudinal development of a simulated gamma-ray and proton shower and their respective Čerenkov images in the focal plane of the telescope. This figure was taken from [A+97b].

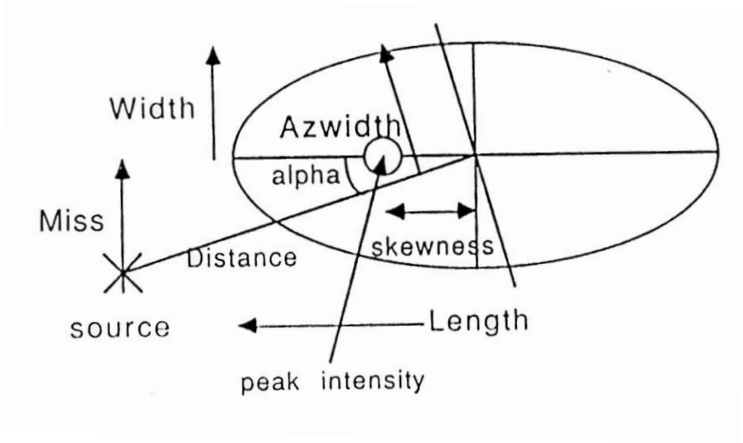

Figure 1.5: Parameters used to describe a shower Čerenkov image. The figure is from [Hil96].

pixels where 16 pixels are grouped together in a so called "drawer". The drawers contain the complete electronic read-out to process the signals. The camera body contains the digital processors and the power supply for the 60 drawers which slide into the camera body. The camera consumes in total 5 kW of electrical power.

With the stereoscopic reconstruction of air showers, the H.E.S.S. telescopes combine very good angular resolution and background rejection, which results in a high flux sensitivity and low energy threshold. The angular resolution calculated from Monte Carlo simulations is expected to $\sigma = 0.1°$ per event [Kon00]. The energy threshold of H.E.S.S. is expected to be lower than 100 GeV with a sensitivity of about 10^{-12} erg cm^{-2} sec^{-1} (or about 10^{-11} cm^{-2} sec^{-1} for 50 hours of observation [Kon00]). At higher energies (1 TeV), the sensitivity reaches a value of about 10^{-13} erg cm^{-2} sec^{-1} (or about10^{-13} cm^{-2} sec^{-1} [Kon00]) as shown in Fig. 1.8.

Because of its performance, H.E.S.S is well suited to observe and resolve extended sources such as the $e^{\pm}$ pair halos from extragalactic sources which will have an angular size of several degrees for sources at redshifts of $z \approx 0.1 \ldots 0.5$. The low energy threshold of 100 GeV and the good flux sensitivity improve the chance of observing the pair halos.

1.2 Cosmic Background Radiation

The existence of the cosmic background radiation (CBR) which is composed of the cosmic infrared (CIB) and cosmic microwave background (CMB) is an essential reason for the formation of the $e^{\pm}$ pair halos. The gamma photons and the $e^{\pm}$ pairs interact with the photons in this radiation field. Most of the

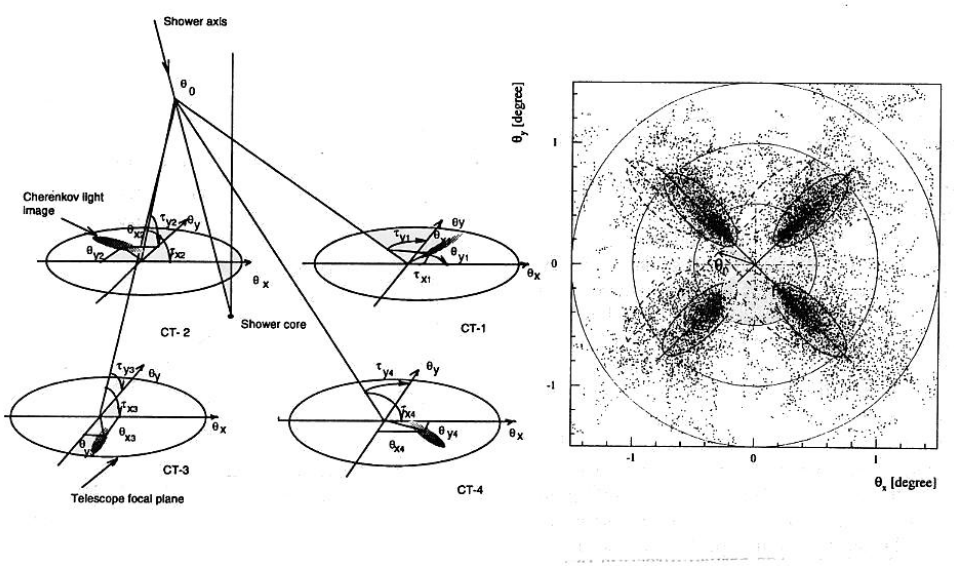

Figure 1.6: Sketch of the stereoscopic reconstruction of the arrival direction of showers. The figure is from [A+97b].

VHE photons interact with the optical/infrared photons in the CIB because of the energy threshold condition and resonance-like character of PP (see Sec. 2.1). On the other hand, the $e^{\pm}$ pairs primarily upscatter microwave photons from the lower energy CMB, because of the nonexistence of a threshold condition for the IC process and the much higher number photon density for the CMB.

The CMB is the radiation field from the thermal equilibrium of the Universe. It is one of the main observational evidences for the Big Bang theory. The spectrum of the CMB can be naturally described by a blackbody radiation characterized by a single temperature T. Its dependence on the cosmological redshift is given by

$$n(\omega_z, z) = \frac{\hbar^{-1}\pi^{-2}c^{-3}\omega_z^2}{\exp(\hbar\omega_z/k_B T(1+z)) - 1}, \tag{1.7}$$

where $n(\omega_z, z)$ is the number of photons per unit comoving volume per unit of energy interval which is measured by a comoving observer at the redshift z, ω_z is the photon angular frequency which is also measured at that epoch, k_B is the Boltzmann constant and the average temperature T at the present epoch is 2.7 K.

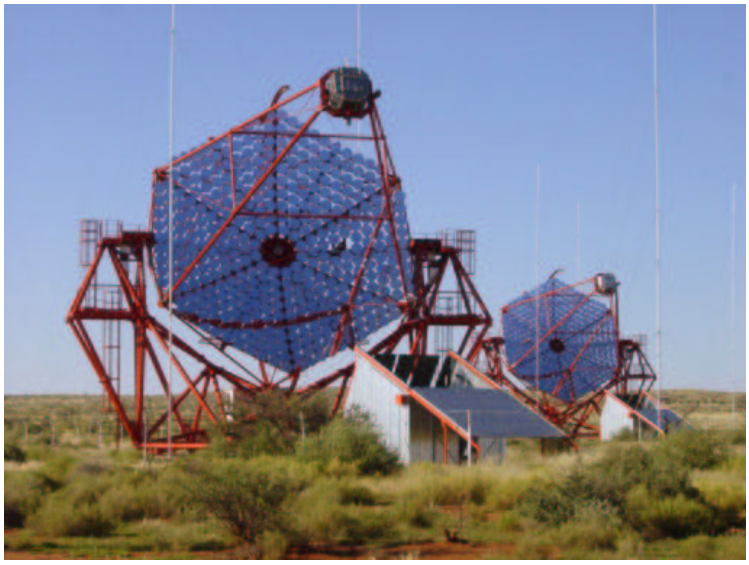

Figure 1.7: The picture shows the first phase of H.E.S.S.

1.2.1 Cosmic Infrared Background

The CIB is in the range of 0.1 μm up to 1 mm and the main sources of these photons are star light and dust absorption/re-emitted photons that are accumulated from all epoches after the Big Bang. It is believed that the information about the star formation history is contained in this field.

Direct Measurement of the CIB

The first direct measurements of CIB were carried out by rocket-borne experiments. There were systematic errors in the measurement from the thermal radiation of the rocket, the Earth's atmosphere and scattered light from the Earth's surface but they could provide upper limits and a claim of possible detection of the CIB [HD01]. The Cosmic Background Explorer (COBE) launched in 1989 was the first observatory that seriously attempted to observe the CIB with two of a total of three experiments on board of COBE: the Diffuse InfraRed Background Experiment (DIRBE) and the Far InfraRed Absolute Spectrophotometer (FIRAS). The COBE satellite was launched into a 900 km altitude, 99.3° inclination orbit.

The DIRBE instrument [HD01] is an absolute photometer which provided maps of the full sky in 10 bands at 1.25, 2.2, 3.5, 4.9, 12, 25, 60, 100, 140, 240 μm. The instantaneous field of view is $0.7° \times 0.7°$. The sensitivity (1σ) of the instrument after cryogenic operation within 10 months is $\sim$ 2 nW m^{-2} sr^{-1} at 1.25 and 2.2 μm, 0.5-1 nW m^{-2} sr^{-1} from 3.5 to 100 μm, 33 nW m^{-2} sr^{-1} and

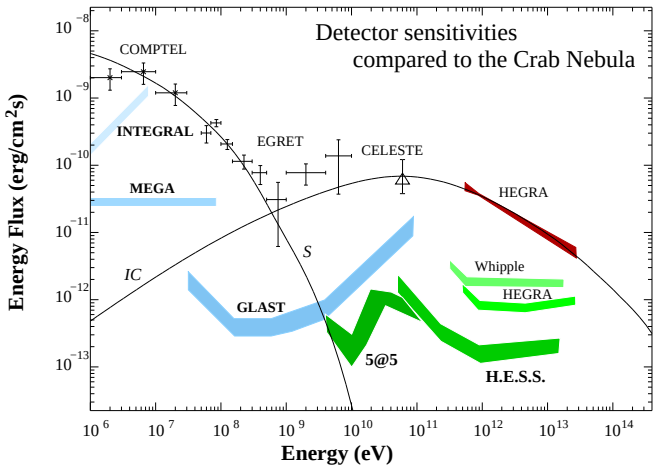

Figure 1.8: H.E.S.S. flux sensitivity together with other gamma-ray observatories and the Crab Nebula flux. Courtesy Dieter Horns.

11 nW m^{-2} sr^{-1} for 140 and 240 μm.

The FIRAS instrument [HD01] is a Fourier transform spectrometer in the form of a polarizing Michelson interferometer. The instrument can provide precise spectral comparison of the sky brightness with that of a very accurate full beam blackbody calibrator at wavelengths from 100 μm to 1 cm. The sensitivity (1σ) from 500 μm to 3 mm was 0.8 nW m^{-2} sr^{-1} and the field of view is 7° diameter.

One of the most recent instruments providing diffuse infrared background measurements is the near infrared spectrometer (NIRS) [N$^+$94] which operated for 30 days in 1995 on the infrared telescope in space (IRTS). The IRTS was flown on a spacecraft which was launched into a 486 km altitude, 28.5° inclination orbit. The NIRS instrument [N$^+$94] was a simple grating spectrometer covering wavelengths from 1.4 to 4.0 μm with a resolution of 0.12 μm. The field of view was 8' × 8'.

To measure this background directly is not trivial. All dominating components of the foreground radiation have to be eliminated. There is foreground radiation from many sources in the local region. The following is a list of the possible sources for the foreground radiation:

1. instrument components themselves
2. Earth atmosphere
3. sources in the solar system
   - the stray light from nearby objects such as the Sun, Moon, and Earth.
   - absorption/re-emission from interplanetary dust (IPD)

4. sources in the local galaxy
    - discrete sources in local galaxy
    - diffuse interstellar medium (ISM).

Some portions of this foreground such as the radiation from the instruments and the Earth atmosphere can be easily eliminated. Cryogenic operation above the Earth's atmosphere like DIRBE, FIRAS and NIRS can reduce the radiation from the instruments and the Earth's atmosphere. For these reasons, the direct measurement for the CIB must be in the outer space above the Earth atmosphere.

Stray light can be reduced by the design of the instruments. For example, the DIRBE can reduce the stray light from wavelength 1.25 to 240 μm to be less than 1 nW cm^{-2} sec^{-1} [HD01].

The foreground radiation from the IPD or the zodiacal light is the most difficult portion of the foreground in order to filter out since it is the main contribution of the total sky brightness in almost all the DIRBE observing bands as shown in Fig. 1.9 and the knowledge of it is poor. To eliminate the zodiacal light contribution, models of the IPD are required. By using the all-sky DIRBE map, a reasonable IPD cloud model was proposed by the DIRBE team in 1998 [K$^+$98].

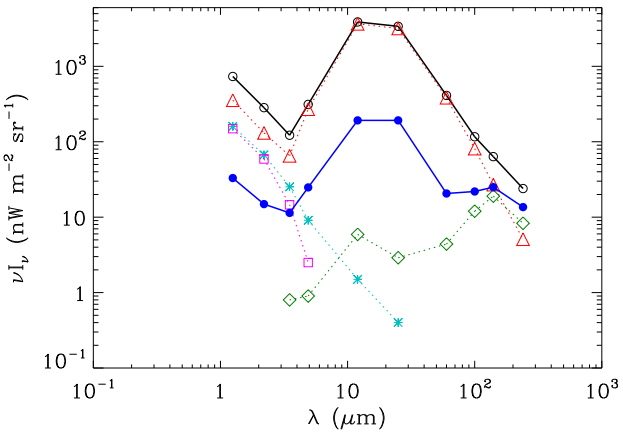

Figure 1.9: Foreground contribution to the DIRBE data at 1.25-240 μm in the Lockman Hole[3] area [LJM86]: the open circles are the observed sky brightness, the triangles are the zodiacal light contribution, the squares are the bright galactic sources contribution, the asterisks are the faint galactic sources contribution, the diamonds are the contribution from ISM, and the solid circles are the residuals after removing all foregrounds from the observed brightness. Figure taken from [HD01].

[3]The region of minimum HI column density at galactic coordinate $(l, b) \sim (150°, +53°)$ or geocentric ecliptic coordinate $(\lambda, \beta) \sim (137°, +45°)$.

The foreground radiation from the galactic discrete sources contributes mostly in the near-infrared region, wavelength 1.25-4.9 μm. These discrete sources were classified into the bright and the faint galactic sources. To eliminate the contribution from bright sources, the localized regions which are much brighter than the average galactic foreground are excluded. The location of these bright sources have been blanked from the maps and were excluded from further analysis. Screening out the contribution of faint galactic sources is more difficult. These sources are sufficiently numerous and evenly distributed that a statistical model well represents their collective emission. The DIRBE team constructed a faint source model based on the statistical model developed by [W$^+$92]. The sky brightness calculated from the faint source models were subtracted from the sky maps (for more detail see [A$^+$98]).

The main contribution to the radiation from ISM occurs in the mid- to far-infrared regions, corresponding to the instrumental wavelength regions 12-100 and 140-240 μm, respectively. The procedure introduced by the DIRBE team [A$^+$98] is as follows. The map from the wavelength 100 μm is used to construct a spatial ISM foreground distribution template for all other wavelengths 12 to 240 μm in the following form. The ISM map at 100 μm is multiplied by an average color factor $\langle \lambda I_\lambda(\lambda)/\lambda I_\lambda(100\mu\text{m})\rangle$ to produce a template at wavelength λ. These template are then subtracted from the corresponding map to produce the final residual maps. The color factor for the wavelength λ is a slope from a linear fitting of the data plot between the intensities of the wavelength λ and of the wavelength 100 μm at the same position taken over the maps.

After modelling and removing the foregrounds, the isotropic distributions of the residuals have to be checked since the background should be, by definition, of extragalactic origin. The isotropy tests from the DIRBE experiment [HD01], for example, include:

1. test of the consistency of the mean residuals on five sky patches near the two galactic poles, the two ecliptic poles, and in the Lockman Hole [LJM86];

2. tests for spatial variations such as gradients with galactic and ecliptic latitude;

3. tests of the residual pixel brightness distributions;

4. test for correlation of the residuals with the foreground models;

5. a two-point correlation function analysis of the residuals on 2% of the sky including areas at high north and south galactic latitudes.

The direct measurement from the COBE was reported in 1998 [D$^+$98]. There are only two wavelengths, the 140 and 240 μm, which are isotropic residuals. Matsumoto et al. (2000) [Mat99] provided direct measurement data from NIRS in the range of 1.4 to 4.0 μm. These direct measurement CIB data are shown in Fig. 1.10 together with other data from indirect measurements and a theoretical calculation from Primack et al. (2000) [PSBD00].

It should be noted that in any case these results only conditionally could be treated as direct measurements because their interpretation depends on the modelling of the foregrounds. Therefore, the direct observations of CIB generally allow derivation of the flux upper limit rather than detection of positive residual signals.

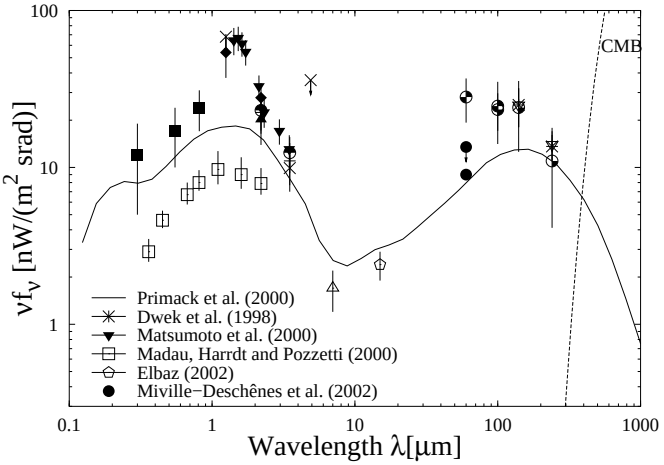

Figure 1.10: Observed CIB data compare with the model. The Figure is based on Aharonian et al., 2003,[A$^+$03]. Courtesy Dieter Horns.

Indirect Measurement

There are several methods to estimate or constrain the CIB fluxes by using, for example, the extragalactic source count. Extragalactic source counts or galaxy counts can provide important constraints on the CIB. The sky brightness calculated by integrating the emitted flux from these sources are used as the lower limit of the CIB. As presented in Fig. 1.10 with a pentagon, Elbaz et al. (2002) [E$^+$02] calculated the lower limit to the 15 μm extragalactic background light of 2.4 ± 0.5 nW m^{-2} sr^{-1} using galaxy counts from the deep extragalactic surveys with ISOCAM.

If one assumes that the main contribution to the CIB comes from extragalactic discrete sources, the spatial fluctuations in the distribution of these should affect the fluctuations in the CIB also. Therefore, conversely, observed spatial fluctuations of the background can give information on the sources' spatial distribution. The fluctuation measurements do not give the CIB flux directly but the CIB flux can be constrained by using several techniques. For example, Miville-Deschênes et al. (2002) [MD$^+$02] analyzed the power spectrum, $P(k)$, which is the absolute value of the Fourier transform of the IRAS ISSA maps at the 60 and 100 μm of 12 fields selected. Miville-Deschênes et al provided the

upper limit of 13.5 nW m^{-2} sr^{-1} and gave an estimate of 9.0 nW m^{-2} sr^{-1} for the flux at 60 μm.

Observing TeV gamma-rays from extragalactic sources is another approach to measure or constrain the CIB. As said at the beginning of the chapter, TeV gamma photons are absorbed by CIB photons. The observed TeV gamma-ray flux ($F_{obs}(E)$) at energy E will relate to the intrinsic source flux ($F_0(E)$) by

$$F_{obs}(E) = F_0(E) \exp(-\tau_{PP}(E)), \tag{1.8}$$

where τ_{PP} is the optical depth for PP. For a given E, the optical depth is proportional to the number density of background photons. Upper limits on the CIB in the mid-infrared region were derived e.g. by Renault et al. (2001) [RBLP01] by using the observed data of the TeV gamma-rays obtained by CAT and HEGRA from Mkn501. The upper limits found by Renault et al. were 4.7 nW m^{-2} sr^{-1} between 5 and 15 μm. The TeV gamma-ray data not only constrain the CIB flux but can constrain the shape spectrum of the CIB also. By using the TeV gamma-ray data from the BL Lac object H1426+428 observed by HEGRA in 1999 and 2000, Aharonian et al. (2002) [A$^+$02a] discussed how the flattening features of the observed TeV spectrum from 1 to 5 TeV reflect the characteristic shape the CIB in the wavelength between 1 and several microns.

The author would like to comment here that all of the CIB measurements, both direct and indirect, can give only the CIB at the present epoch. None of them can measure the CIB at a specific redshift. The $e^{\pm}$ pair halos, however, can provide an opportunity to gain some information of the CIB at a specific redshift, since the interactions that lead to the formation of pair halos take place in the local region nearby the primary gamma-ray sources. Consequently, observing pair halos from many sources at various redshifts might open the possibilities to trace the formation of the CIB and therefore gain information about the star formation history.

The structure of this thesis is as follows. Chapter 2 introduces the pair halo model and its physical basis. Numerical methods based on Monte Carlo schemes are presented in Ch. 3, and numerical results for various situations are given in Ch. 4. Chapter 5 concludes the results from the study and discusses the possibility of detecting pair halos from TeV Blazars. Finally, a summary is given in Ch. 6.

Chapter 2

Giant Electron-Positron Pair Halos

2.1 Interactions

For the electron-positron ($e^{\pm}$) pair halo model, there are two interactions which are relevant. One is $\gamma\gamma$ pair production (PP), and the other is inverse Compton scattering (IC). In the following, the physics of these interactions are discussed.

Three different inertial frames are used, with primes denoting variables in the electron rest frame, "hats" ($\hat{}$) denoting variables in the center-of-momentum (CM) frame. Otherwise the variables are measured in the lab frame.

Note that only in this section, Sec.2.1, the units $m_e = 1$, $\hbar = 1$ and $c = 1$ are used.

2.1.1 $\gamma\gamma$ Pair Production

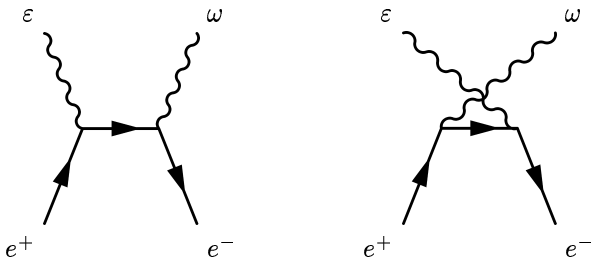

Figure 2.1: Feynman diagrams of $\gamma\gamma$ pair production.

From special relativity one obtains the energy condition by applying conservation of four momentum, p_μ, and the invariance of $p_\mu p^\mu$. The result is

$$2(1-\hat{\beta}^2)^{-1} = \varepsilon\omega(1-\cos\theta), \tag{2.1}$$

where ε and ω represent the lab-frame energy of the colliding photons, θ is the angle between their lab-frame 3-momenta, and $\hat{\beta}$ is the speed of $e^{\pm}$ in the CM frame. The threshold condition is derived by assuming that the photons collide head-on and produce an $e^{\pm}$ pair at rest:

$$\varepsilon_{th} = \frac{1}{\omega}. \tag{2.2}$$

The process of $\gamma\gamma$ pair production is presented as 2 independent Feynman diagrams in Fig. 2.1. Using the standard method of quantum electrodynamics, the PP total cross section can be obtained (e.g., Akhiezer and Berestetskii, 1965 [AB65])

$$\sigma_{PP} = \frac{3}{16}\sigma_T(1-\hat{\beta}^2)\hat{\beta}\left[\frac{(3-\hat{\beta}^4)}{\hat{\beta}}\ln\frac{1+\hat{\beta}}{1-\hat{\beta}} + 2(\hat{\beta}^2-2)\right], \tag{2.3}$$

where

$$\sigma_T = \frac{8}{3}\pi r_0^2 \tag{2.4}$$

is the Thomson cross section and r_0 is the classical electron radius.

From the total cross section, the absorption probability per propagation distance for a photon with energy ε moving through an isotropic photon gas can be formulated. Let $n(\omega)$ be the background photon number density per unit energy in the lab frame. In the interval $(\theta, \theta + d\theta)$ there are $(1/2)n(\omega)\sin\theta d\theta$ soft photons interacting with every hard photon, and one obtains

$$\frac{d\tau_{PP}}{dx}(\varepsilon) = \Lambda_{PP}^{-1}(\varepsilon) = \int_{1/\varepsilon}^{\infty} \overline{\sigma}_{PP} n(\omega) d\omega, \tag{2.5}$$

where τ_{PP} is optical depth, Λ_{PP} is the PP mean free path length of the hard photon, with an angle-averaged cross section

$$\overline{\sigma}_{PP} = \frac{1}{2}\int_{-1}^{1-2/s_0} (1-\mu)\sigma_{PP} d\mu. \tag{2.6}$$

Here, $\mu = \cos\theta$ and $s_0 = \varepsilon\omega$. The quantity $(1-\mu)/2$ represents the relative velocity of the soft photon along the direction of propagation of the hard photon. The analytic solution of Eq.(2.6) was found by Gould and Schréder (1967) [GS67],

$$\overline{\sigma}_{pp} = \frac{3}{8}\sigma_T\left(\frac{1}{s_0}\right)^2 \varphi_{PP}(s_0), \tag{2.7}$$

where

$$\begin{aligned}
\varphi_{PP}(s_0) &= \frac{1+\beta_0^2}{1-\beta_0^2}\ln\alpha_0 - \beta_0^2\ln\alpha_0 - \ln^2\alpha_0 \\
&\quad -\frac{4\beta_0}{1-\beta_0^2} + 2\beta_0 + 4\ln\alpha_0\ln(\alpha_0+1) - 4L(\alpha_0), && (2.8)\\
\beta_0^2 &= 1 - 1/s_0, && (2.9)\\
\alpha_0 &= (1+\beta_0)/(1-\beta_0), && (2.10)
\end{aligned}$$

and $L(\alpha_0)$ is the dilogarithm function,

$$L(\alpha_0) = -\int_0^{\alpha_0} \frac{ln(1-t)}{t} dt, \tag{2.11}$$

which can be written as a series expansion;

$$L(\alpha_0) = \frac{1}{2}\ln^2 \alpha_0 + \frac{\pi^2}{12} - \sum_{n=1}^{\infty} (-1)^{n-1} n^{-2} \alpha_0^{-n}. \tag{2.12}$$

The formula in Eq.(2.8) is computationally costly. However, an approximate

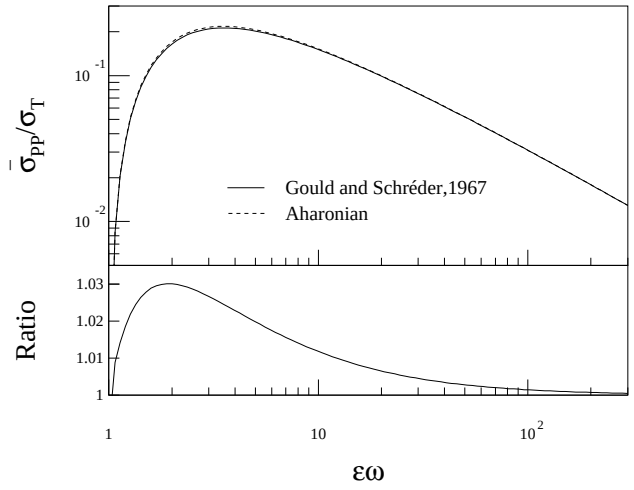

Figure 2.2: The cross section $\overline{\sigma}_{PP}$ as given by Gould&Schréder, 1967 (solid line); i.e., Eq.(2.8), and computed from the approximate formula derived by Aharonian (dashed line); i.e., Eq.(2.13). Both are shown in units of the Thomson cross section σ_T. The approximate formula is accurate to within 3%, as demonstrated in the lower panel.

form is given by (Aharonian, private communication),

$$\begin{aligned} \overline{\sigma}_{PP} &= \frac{3\sigma_T}{2s_0^2}\left[\left(s_0 + \frac{1}{2}\ln s_0 - \frac{1}{6} + \frac{1}{2s_0}\right)\ln(\sqrt{s_0} + \sqrt{s_0 - 1})\right. \\ &\quad \left. - \left(s_0 + \frac{4}{9} - \frac{1}{9s_0}\right)\sqrt{1 - \frac{1}{s_0}}\right], \end{aligned} \tag{2.13}$$

which requires less CPU time, and still has an accuracy of better than 3%, as evident from Fig. 2.2.

The mean free path is a key quantity in the numerical simulation, but from a theoretical point of view, especially for PP, the optical depth is more important. For the simple case, when the background photon field $n(\omega)$ is independent of

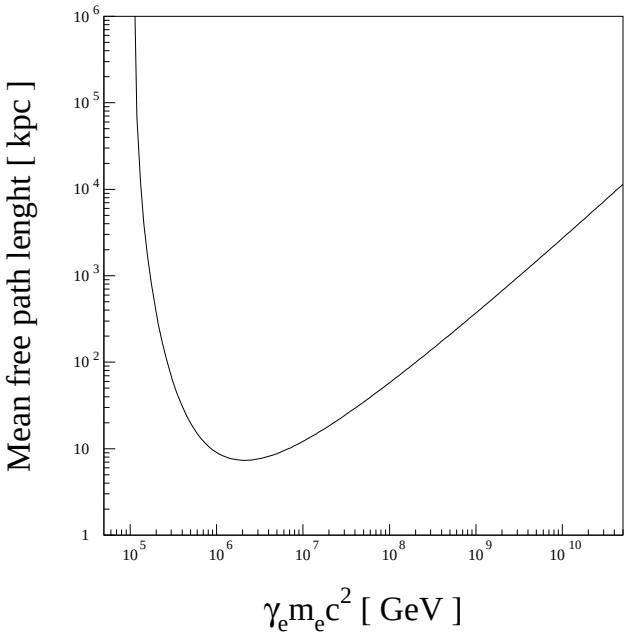

Figure 2.3: The mean free path length of a gamma photon in the 2.7 K microwave background.

redshift, or when the redshift is too small to affect the background, the optical depth becomes

$$\tau_{PP} = \Lambda_{PP}^{-1} d, \tag{2.14}$$

where $d = cz/H_0$ is the source distance corresponding to a redshift z, H_0 being Hubble's constant[1]. The function $\overline{\sigma}_{PP}$ is strongly peaked, with a maximum at

$$\omega_{max} = 4/\varepsilon, \tag{2.15}$$

and a convenient approximation for the PP optical depth [Her74, A$^+$99] can thus be written

$$\tau_{PP} \approx \frac{\sigma_T}{4} \omega_{max} n(\omega_{max}) d. \tag{2.16}$$

The situation gets more complicated when the photons come from sources located at high redshift, such that the effect of cosmological expansion has to be taken into account. In this case, an observed photon with energy ε_0 corresponds to a photon emitted at redshift z with energy ε_z given by

$$\varepsilon_z = \varepsilon_0 (1 + z). \tag{2.17}$$

The same applies to background photons;

$$\omega_z = \omega_0 (1 + z). \tag{2.18}$$

[1]In this work the Hubble constant has been set to $H_0 = 60$ km/s/Mpc.

A natural consequence of the cosmological expansion is that the volume of the universe was smaller in the past by a factor $(1+z)^{-3}$. Thus, if the background photons were already in place at redshift z and no absorption or re-emission occurs, the background photon field , $n(\omega_z, z)$, as seen by a comoving observer in that epoch becomes

$$n(\omega_z, z)d\omega_z = (1+z)^3 n(\omega_0, 0)d\omega_0. \tag{2.19}$$

The PP optical depth associated with the photons from high redshift sources must include the effects of redshift phenomena. The photon energy ε_z from sources at high redshift z travels through the background photon field $n(\omega_z, z)$ in different redshifts before reaching the observer with energy ε. The PP optical depth, therefore, can be calculated by integrating Eq.(2.5) along the propagation distance $dx = -c\ dt/dz\ dz$:

$$\tau_{PP}(z_s, \varepsilon) \quad = \quad -c \int_0^{z_s} \frac{dt}{dz} dz \int_{1/\varepsilon_z}^{\infty} d\omega_z n(\omega_z, z) \overline{\sigma}_{PP}(\varepsilon_z, \omega_z), \tag{2.20}$$

where dt/dz is the cosmic time-redshift relation. The cosmic time relates with redshift through the time derivative of the scaling factor $\dot{R}(t)$ which is model dependent. In the Friedman cosmological model with cosmological constant $\Lambda = 0$ used in this work the cosmic time-redshift relation[2] is [Lon98]

$$\frac{dt}{dz} = -\frac{1}{H_0(1+z)^2(1+2q_0 z)^{1/2}}. \tag{2.21}$$

Therefore,

$$\tau_{PP}(z_s, \varepsilon) = \frac{c}{H_0} \int_0^{z_s} dz(1+z)^{-2}(1+2q_0 z)^{-1/2} \int_{1/\varepsilon_z}^{\infty} d\omega_z n(\omega_z, z) \overline{\sigma}_{PP}(\varepsilon_z, \omega_z), \tag{2.22}$$

where q_0 is the deceleration parameter[3].

Another important function for the model is the resulting $e^{\pm}$ energy distribution. For very different energies between the colliding photons the resulting distribution is given approximately by[4] [AAN83]

$$\begin{aligned} \frac{dN_e(\gamma_e, w, \varepsilon)}{d\gamma_e} \quad = \quad & \frac{3\sigma_T}{32w^2\varepsilon^3} \left[\frac{4\epsilon^2}{(\epsilon - \gamma_e)\gamma_e} \ln \frac{4w(\epsilon - \gamma_e)\gamma_e}{\epsilon} - 8w\epsilon \right. \\ & \left. + \frac{2(2w\epsilon - 1)\epsilon^2}{(\epsilon - \gamma_e)\gamma_e} - \left(1 - \frac{1}{w\epsilon}\right) \frac{\epsilon^4}{(\epsilon - \gamma_e)^2 \gamma_e^2} \right]. \end{aligned} \tag{2.23}$$

In Eq.(2.23), $\gamma_e = E_e/m_e c^2$ represents the electron (positron) energy, and $\epsilon = \varepsilon + \omega \approx \varepsilon$ gives the total lab-frame photon energy. The range of γ_e is

$$\frac{\epsilon}{2}\left(1 - \sqrt{1 - \frac{1}{\epsilon\omega}}\right) \leq \gamma_e \leq \frac{\epsilon}{2}\left(1 + \sqrt{1 - \frac{1}{\epsilon\omega}}\right). \tag{2.24}$$

[2] See more detail in Appendix A.

[3] This work uses $q_0 = 0.5$.

[4] subscript e in the formulas represents electron/positron.

In the current model, the energy difference between the hard and soft photons in the lab frame is greater than 10 orders of magnitude, and Eq.(2.23) is always applicable.

The $e^{\pm}$ spectrum is symmetric about the energy $\epsilon/2$, which is also the minimum point of the function, as shown in Fig. 2.4. One can also see that the larger s_0 is, the more pronounced and the further apart are the maxima of Fig. 2.4. For very large s_0, one of the outcoming particles, e^- or e^+, receives almost all the photon energy (as seen from the lab frame).

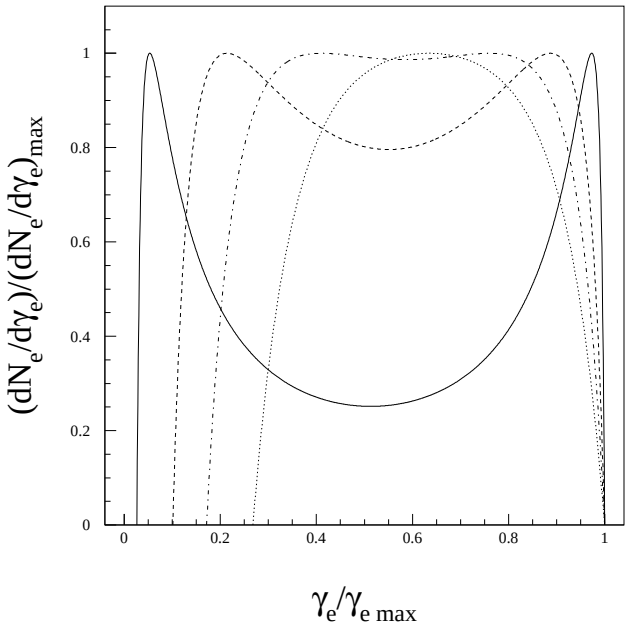

Figure 2.4: Differential spectra of $e^{\pm}$ from $\gamma\gamma$ pair production in different cases: s_0=10 (solid line), $s_0 = 3$ (dashed line), $s_0 = 2$ (dot-dashed line) and $s_0 = 1.5$ (dotted line).

2.1.2 Inverse Compton Scattering

To calculate the energy of a photon in the lab frame after scattering on an $e^{\pm}$, the photon energy can be transformed from the lab frame to the $e^{\pm}$ rest frame,

$$\omega' = \gamma\omega(1 - \beta\cos\theta), \tag{2.25}$$

where $\gamma = (1-\beta^2)^{-1/2}$, θ is the angle between the electron and photon momenta, and β the $e^{\pm}$ speed in the lab frame. Applying the conservation of four momentum in the $e^{\pm}$ rest frame gives a relation between the photon energy

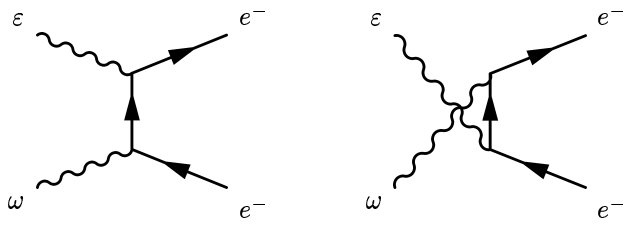

Figure 2.5: Feynman diagrams of IC.

before (ω') and after (ε') scattering;

$$\varepsilon' = \frac{\omega'}{1 + \omega'(1 - \cos\Theta_1')}. \tag{2.26}$$

Here,

$$\cos\Theta_1' = \cos\theta' \cos\theta_1' + \sin\theta' \sin\theta_1' \cos(\phi' - \phi_1'), \tag{2.27}$$

where Θ_1' is the angle between the photon momenta before and after scattering, θ_1' is the angle between the scattered photon and the electron velocity before the scattering, and ϕ' and ϕ_1' are the azimuthal angles of the scattered and incident photon in the rest frame. Transforming back to the lab frame, one obtains

$$\varepsilon = \gamma\varepsilon'(1 + \beta\cos\theta_1'). \tag{2.28}$$

In the special case of a head-on collision, the photon energy gain is given by $\varepsilon_{max} \approx 4\gamma^2\omega$, which is quite large for a photon colliding with a high energy electron. However, it is still small compared with the electron energy; in other words the electron loses a small fraction of its energy in each scattering in the Thomson regime. In the extreme Klein-Nishina regime, on the other hand, the electron loses almost all its energy during one interaction.

In the lab frame, the total cross section for this interaction (e.g., Akhiezer and Berestetskii, 1965 [AB65]) is

$$\sigma_{IC} = \frac{3\sigma_T}{4\chi}\left[\left(1 - \frac{4}{\chi} - \frac{8}{\chi^2}\right)\ln(1+\chi) + \frac{1}{2} + \frac{8}{\chi} - \frac{1}{2(1+\chi)^2}\right], \tag{2.29}$$

where $\chi = 2w\gamma_e(1 - \beta\mu)$.

The collision probability per unit distance for an electron propagating through an isotropic photon gas with density $n(\omega)$ is

$$\frac{d\tau_{IC}}{dx} = \Lambda_{IC}^{-1} = \frac{1}{\beta}\int_0^\infty \overline{\sigma}_{IC} n(\omega) d\omega, \tag{2.30}$$

where τ_{IC} is the $e^\pm$ optical depth, Λ_{IC} is the mean free path length with respect to IC, and the angle-averaged IC total cross section is

$$\overline{\sigma}_{IC} = \frac{1}{2}\int_{-1}^{1} (1 - \beta\mu)\sigma_{IC} d\mu. \tag{2.31}$$

The exact solution for Eq.(2.30) [AKUV85, Pro86] is

$$\overline{\sigma}_{IC} = \frac{3}{8}\sigma_T \left(\frac{1}{\chi_0}\right)^2 \varphi_{IC}(\chi_0), \tag{2.32}$$

with

$$\chi_0 = \gamma_e w, \tag{2.33}$$

$$\varphi_{IC}(\chi_0) = F(\chi_0(1+\beta)) - F(\chi_0(1-\beta)) \tag{2.34}$$

$$F(\xi) = -\frac{\xi}{4} + \left(\frac{9}{4} + \frac{1}{\xi} + \frac{\xi}{2}\right)\ln(1+2\xi) + \frac{1}{8+16\xi} - \frac{3}{8} + \frac{1}{2}\ln^2 2\xi + \frac{\pi^2}{12} - L(-2\xi), \tag{2.35}$$

An approximate formula for Eq.(2.32) was derived by Coppi and Blandford (1990) [CB90]:

$$\overline{\sigma}_{IC} = \frac{3\sigma_T}{8\chi_0}\left[\left(1 - \frac{2}{\chi_0} - \frac{2}{\chi_0^2}\right)\ln(1+2\chi_0) + \frac{1}{2} + \frac{4}{\chi_0} - \frac{1}{2(1+2\chi_0)^2}\right]. \tag{2.36}$$

The functional dependence of $\overline{\sigma}_{IC}$ is shown in Fig. 2.6. In the Thomson regime, $\chi_0 \ll 1$, the total cross section is energy independent. In the Klein-Nishina regime, $\chi_0 \gg 1$, the $e^{\pm}$ total cross section is a decreasing function of the $e^{\pm}$ energy; i.e., $\propto \chi_0^{-1}$. The probability per propagation length for IC of an $e^{\pm}$ passing through an isotropic photon gas is shown in Fig. 2.7.

Due to the fact that in the Thomson regime an $e^{\pm}$ loses only a small fraction of its energy in each interaction, one can compute the associated, effective energy loss rate. It is given by (e.g. [BG70])

$$\frac{d\gamma_e}{dt} = \frac{4}{3}\sigma_T c \gamma_e^2 U_{ph}, \tag{2.37}$$

where U_{ph} is the energy density of the isotropic photon gas

$$U_{ph} = \int_0^\infty \omega\, n(\omega) d\omega. \tag{2.38}$$

The mean energy of the scattered photon is

$$\overline{\varepsilon} = \frac{4}{3}\gamma^2 \overline{\omega}. \tag{2.39}$$

The spectral distribution of the scattered photons via IC for the isotropic photon gas [AA81] is

$$\frac{dN_\varepsilon}{d\varepsilon} = \frac{3\sigma_T}{4w\gamma_e^2}\left[1 + \frac{x^2}{2(1-x)} + \frac{x}{b(1-x)} - \frac{2x^2}{b^2(1-x)^2}\right] - \frac{x^3}{2b(1-x)^2} - \frac{2x}{b(1-x)}\ln\frac{b(1-x)}{x}, \tag{2.40}$$

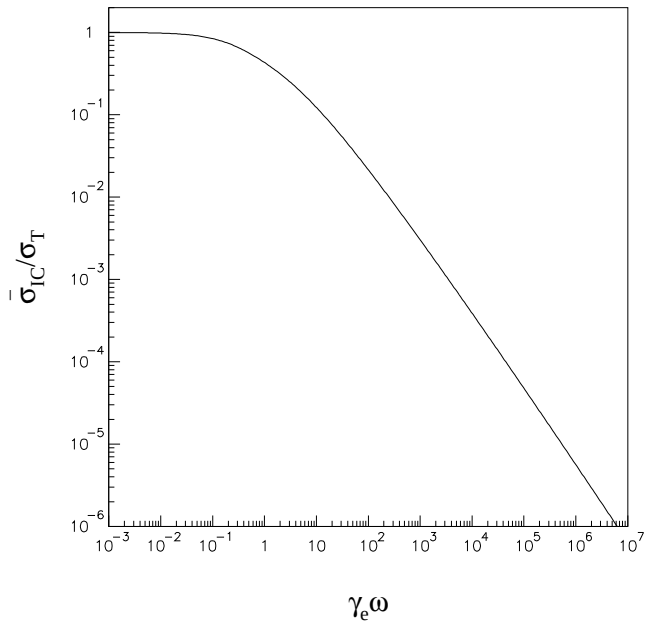

Figure 2.6: The approximation of the angle average IC cross section, $\overline{\sigma}_{IC}$, [CB90] in Eq.(2.36).

$$\frac{\omega}{\gamma_e} \ll x \leq \frac{b}{1+b} = \frac{\varepsilon_{max}}{\gamma_e}, \tag{2.41}$$

$$x \equiv \frac{\varepsilon}{\gamma_e} \tag{2.42}$$

and

$$b \equiv 4\omega\gamma_e. \tag{2.43}$$

The spectrum of upscattered photons depends only on the parameter b, as illustrated in Fig. 2.8. For small b i.e.; in the Thomson regime, the upscattered photon population is predominantly in the low energy regime, whereas for large b, corresponding to the Klein-Nishina regime, the population is shifted towards high energies.

2.2 The Physical Model

The $e^{\pm}$ pair halo model which was proposed by Aharonian, Coppi and Völk (1994) [ACV94] concerns the effect of the intergalactic magnetic field on electromagnetic cascades of VHE gamma rays, 1 TeV $< E_{\varepsilon 0} <$ 1 PeV, from extragalactic sources.

The physical basis of the model is schematically shown in Fig. 2.9. The VHE photons are emitted from an extragalactic source. Absorption of these

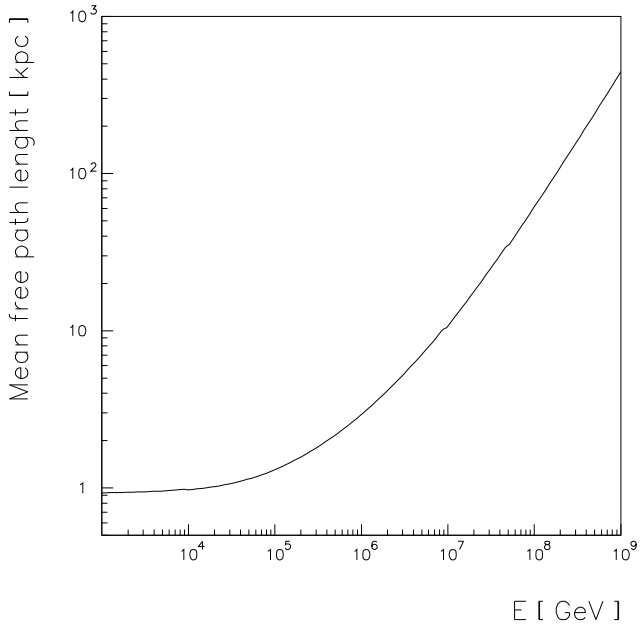

Figure 2.7: Inverse Compton scattering mean free path in 2.7 K black body background photon distribution.

VHE gamma rays via PP with ambient soft photons (e.g., from the cosmic microwave background (CMB) [GS66] and the cosmic infrared background (CIB) [WTW72, SJS92]) is substantial on cosmological propagation scales. Only gamma rays with energies greater than several hundred TeV can interact with CMB photons to produce pairs, whereas those with lower energies can produce pairs in collisions with CIB photons. The number density of the low energy gamma photon population is normally higher than that of the high energy one for a reasonable source spectrum such as a power law. The PP opacity is therefore mainly due to the CIB. Even in the case of a monoenergetic distribution of primary VHE photons at several hundred TeV, the CIB dominates the PP opacity after several cascade generations.

On the other hand, the contribution to the IC opacity is dominated by the CMB, rather than the CIB. The first generation $e^{\pm}$ pairs will interact with soft photons from the same background photon field via IC and produce secondary gamma rays. Almost all soft photons that interact with the $e^{\pm}$ are in the CMB, because it has a much higher number density than the CIB. The IC upscattered gamma photons in the Klein-Nishina regime are absorbed by the CIB, whereas most of the photons from the Thomson regime experience an optically thin background and propagate freely to the observer.

The extragalactic magnetic field plays an important role if it is sufficiently strong, say $|\mathbf{B}| \approx 10^{-9}$ G. The gyroradius R_{gyro} of $e^{\pm}$s of energy E_e in this field

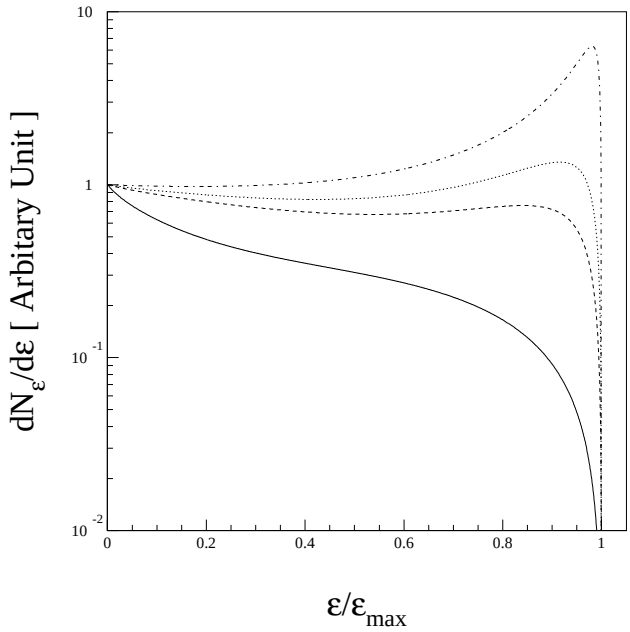

Figure 2.8: Upscattered photon spectral energy distribution in arbitrary units for different cases: b→0 (solid line), b=5 (dashed line), b=10 (dotted line), and b=50 (dot-dashed line).

is about $R_{gyro} = 100$ pc $(E_e/100$ TeV$)(10^{-9}$ G$/|\mathbf{B}|)$. At the same energy, $E_e \approx$ 100 TeV, the IC mean free path length $\Lambda_{IC} \approx 1$ kpc, as shown in Fig. 2.10: $R_{gyro} \ll \Lambda_{IC}$. This means that after the $e^{\pm}$s are produced they will gyrate several times before interacting with soft photons via IC, and therefore the secondary gamma rays will be emitted isotropically. In previous cascade models, which do not take into account the effect of the intergalactic magnetic field, the assumption that all cascade particles travel in a straight line to the observer has been applied.

The isotropically upscattered secondary gamma rays with an energy above the PP threshold will produce a new generation of $e^{\pm}$s, which in turn produce still another generation of isotropic secondary gamma rays. The cascade develops until gamma rays of a later generation have an energy less than the threshold energy, $E_{\varepsilon th} = m_e^2 c^4 / E_\omega$. Gamma photons with lower energies do not interact with the background via PP, and therefore travel directly to the observer. Such low-energy gamma photons are generated by the $e^{\pm}$s via IC in the Thomson regime. After many cascade generations, there are a large number of $e^{\pm}$s distributed isotropically around a VHE gamma ray source, and these pairs produce gamma photons which may be detected by an observer.

Both the spatial and angular distributions of gamma-rays formed during the cascade development in the vicinity of nonthermal extragalactic objects depend

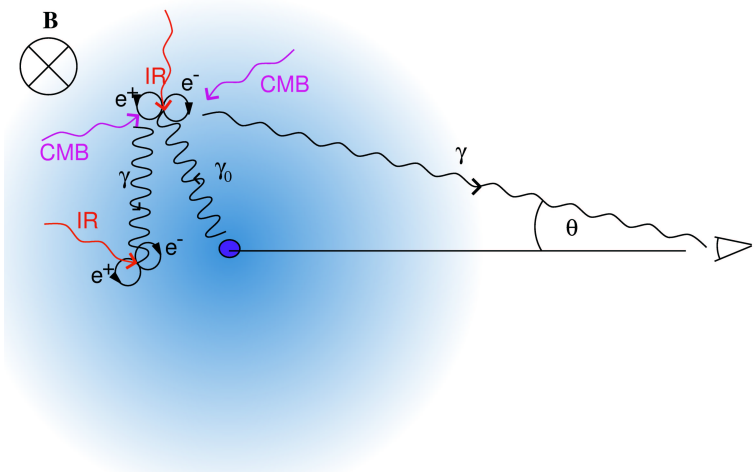

Figure 2.9: Physical picture of $e^{\pm}$ pair halo.

on the CIB at the epoch corresponding to the redshift of the central source. Thus, the detection and study of angular and energy distributions of gamma-rays from Pair Halos surrounding extragalactic objects at different redshifts would provide us with unique information about the CIB at remote cosmological epochs and its evolution in time, not achievable by other means. Indeed, the direct measurements of CIB, as well as the derivation of the CIB, based on the study of absorption of gamma-rays in the intergalactic medium, contain information only about the CIB integrated over large cosmological timescales.

Due to the fact that the radiation from the pair halo is isotropic, it can be observed from any direction. This fact opens interesting possibilities, in that certain types of VHE gamma ray sources have a highly anisotropic radiation field (e.g., BL Lac galaxies) and can only be observed directly if their jet axis is aligned with the observer. The phenomenon of pair halos might open a new search channel for BL Lac galaxies which have not yet been identified.

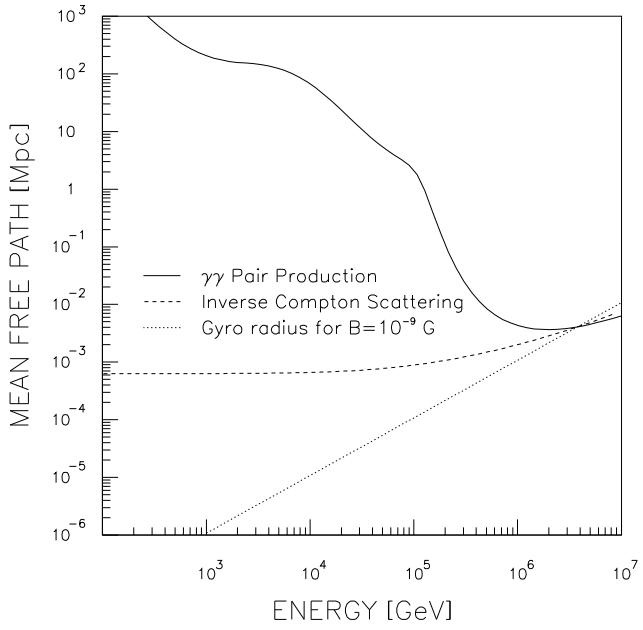

Figure 2.10: The PP and IC mean free path lengths for a specific CBR model, plotted together with the $e^{\pm}$ gyro radius for a magnetic field $|\mathbf{B}| = 10^{-9}$ G.

Chapter 3

Monte Carlo Simulation

From the $e^{\pm}$ pair halo model, the two most important observable quantities are the $e^{\pm}$ pair halo gamma photon energy and angular distribution. To calculate the photon energy distribution from the electromagnetic cascade, most people use the Monte Carlo method and calculation from two transport equations of both $e^{\pm}$s and photons.

The transport equation for the $e^{\pm}$s [Lee98] is

$$\begin{aligned}\frac{d\aleph_e(E_e,t)}{dt} &= -\aleph_e(E_e,t)\cdot c\cdot\int dE_\omega n(E_\omega) \\ &\times\int d\mu\frac{1}{2}(1-\beta\mu)\sigma_{IC}(E_e,E_\omega,\mu) \\ &+c\cdot\int dE_e{}'\aleph_e(E_e{}',t)\int dE_\omega n(E_\omega) \\ &\times\int d\mu\frac{1}{2}(1-\beta'\mu)\frac{d\sigma_{IC}}{dE_e{}'}(E_e;E_e{}',E_\omega,\mu) \\ &+c\cdot\int dE_\varepsilon\aleph_\varepsilon(E_\varepsilon,t)\int dE_\omega n(E_\omega) \\ &\times\int d\mu\frac{1}{2}(1-\mu)\frac{d\sigma_{PP}}{dE_e}(E_e;E_\varepsilon,E_\omega,\mu) \\ &+Q_e(E_e,t),\end{aligned} \tag{3.1}$$

where $\aleph_e(E_e,t)$ is the differential number density of $e^{\pm}$s at energy E_e at time t, $n(E_\omega)$ is the differential number density of background at energy E_ω, $Q_e(E_e,t)$ is an external source term for $e^{\pm}$s at energy E_e at time t, μ is the cosine of the interaction angle between the $e^{\pm}$s and the background photons and β is the velocity of the $e^{\pm}$s. Eq.(3.1) describes the changing of the differential number density within interval time dt. The loss rate in the first term is due to $e^{\pm}$s with energy E_ε changing their energies via the IC. The other terms represent the gain rate of the $e^{\pm}$s differential number density due to: $e^{\pm}$s with energy $E_\varepsilon{}'$ change to be E_ε via the IC (the second term), $e^{\pm}$s produced by the PP (the third term), the external $e^{\pm}$ source $Q_e(E_e,t)$ (the last term).

For photons the equation is

$$\begin{aligned}\frac{d\aleph_\varepsilon(E_\varepsilon,t)}{dt} &= -\aleph_\varepsilon(E_\varepsilon,t)\cdot c\cdot\int dE_\omega n(E_\omega) \\ &\times\int d\mu\frac{1}{2}(1-\mu)\sigma_{PP}(E_\varepsilon,E_\omega,\mu) \\ &+c\cdot\int dE_e\aleph_e(E_e,t)\int dE_\omega n(E_\omega) \\ &\times\int d\mu\frac{1}{2}(1-\beta\mu)\frac{d\sigma_{IC}}{dE_\varepsilon}(E_\varepsilon,E_e,E_\omega,\mu) \\ &+Q_\varepsilon(E_\varepsilon,t),\end{aligned} \tag{3.2}$$

where $\aleph_\varepsilon(E_\varepsilon,t)$ is the differential number density of photons at energy E_ε at time t and $Q_\varepsilon(E_\varepsilon,t)$ is an external source term for photons at energy E_ε at time t. The photon differential number density changes because of the loss rate from the PP. Whereas the gain rate from the IC and the external photon source are represented as the second and third term in the right hand side of Eq.(3.2) respectively.

Using Eq.(3.1) and (3.2) to compute the energy distribution of the pair halo is much more economical than Monte Carlo simulation in terms of computing time. However, It is clear that the $e^{\pm}$ pair halo angular distribution can not be gained by using these two transport equations. Another method that can calculate both the energy and angular distribution of the pair halo. It is the solving of the kinetic equations for different generations of particles produced by the cascade [Kha03]. However, this method is only applicable for the pair halo developing in the high magnetic field ($\approx 10^{-6}$ G) region which synchrotron cooling is not negligible. Monte Carlo simulation is the most suitable method for calculating the pair halo angular distribution.

The Monte Carlo methods have been defined by Halton (1970) [Hal70]: *the Monte Carlo method is defined as representing the solution of a problem as a parameter of a hypothetical population, and using a random sequence of numbers to construct a sample of the population, from which statistical estimates of the parameter can be obtained.*

In the current work, the pair halos were simulated by following all particles, i.e. $e^{\pm}$s and gamma-photons and calculating all interactions that these particle encounter in the electromagnetic cascades. The Monte Carlo method was used to generate parameters for many distributions that are needed for the simulation. Monte Carlo simulation is arguably the best method, since this allows the most comprehensive analysis for an arbitrary background photon field and primary VHE photon spectrum. This Chapter discusses the Monte Carlo scheme which has been used in the current work.

3.1 Simulation of the Pair Halo

Consider a VHE gamma photon source which is located at redshift z_s while the observer is at redshift 0. The distance between the source and the observer, d_s, equals the coordinate distance, D_c (see Appendix A); i.e.,

$$d_s = D_c, \tag{3.3}$$

that can be written as a function of the luminosity distance, D_l, which is more realistic distance,

$$D_c = D_l/(1+z_s). \tag{3.4}$$

The coordinate distance between two objects can be calculated by integrating the line element along the propagation of light which travel from one objects to the other. For the specific cosmology model such as the Friedmann model with cosmological constant $\Lambda = 0$ used in the current work, the coordinate distance can be expressed as [Mat58],

$$D_c = \frac{1}{(1+z_s)}\frac{c}{H_0 q_0^2}\left\{q_0 z_s + (q_0-1)\left[-1+(2q_0 z_s+1)^{1/2}\right]\right\}, \tag{3.5}$$

However, the equivalent expression given by [Ter77],

$$D_c = \frac{1}{(1+z_s)}\frac{cz_s}{H_0}\left[1+\frac{z_s(1-q_0)}{(1+2q_0 z_s)^{1/2}+1+q_0 z_s}\right], \tag{3.6}$$

is better in order to avoid terms that almost cancel at small $q_0 z_s$. In the case of small z, both Eq.(3.5) and Eq.(3.6) reduces to Hubble's law, $d_s \approx cz_s/H_0$.

In the numerical code, there are two conditions which determine when an electromagnetic cascade is stopped:

- The scattering takes place at a distance larger than a maximum value given by $d_c = 10^3 d_s$. This condition ensures that IC scattering beyond the observer which produces radiation returning inward is taken into account.
- The $e^{\pm}$s energy is less than a specified limit, $E_e < E_{emin}$.

In principle, the interactions should be simulated until the $e^{\pm}$s have lost all their kinetic energy. For computational reasons, however, this approach is impossible, and the second condition defined above is used. For most of the simulations of the current work, the pair halo photon energy distribution is considered only at energies E_ε above 10 GeV. In order to achieve good statistics for the spectrum down to this value, the minimum electron Lorentz factor $\gamma_{e,\min}$ is then defined according to

$$\begin{aligned}\gamma_{e,\min} &\approx \sqrt{\frac{3}{4}\frac{0.1\times\overline{E_\varepsilon}_{\min}}{6\times10^{-4}\ \mathrm{eV}}} \\ &\approx 10^6\left(\frac{\overline{E_\varepsilon}_{\min}}{10\,\mathrm{GeV}}\right)^{\frac{1}{2}}.\end{aligned} \tag{3.7}$$

with $\overline{E_{\varepsilon \min}} = 10$ GeV. In Eq.(3.7), the mean soft photon energy has been taken to be approximately 6×10^{-4}, corresponding to the CMB (see, e.g., [MW86]), and an empirical constant factor ("0.1" in the formula) has been introduced. For $\overline{E_{\varepsilon \min}} = 10$ GeV, $\gamma_{e,\min}$ corresponds to an electron energy of $E_{e,\min} \approx 560$ GeV. In Fig. 3.1 the cases of $E_{e,\min} \approx 560$ and 180 GeV are compared.

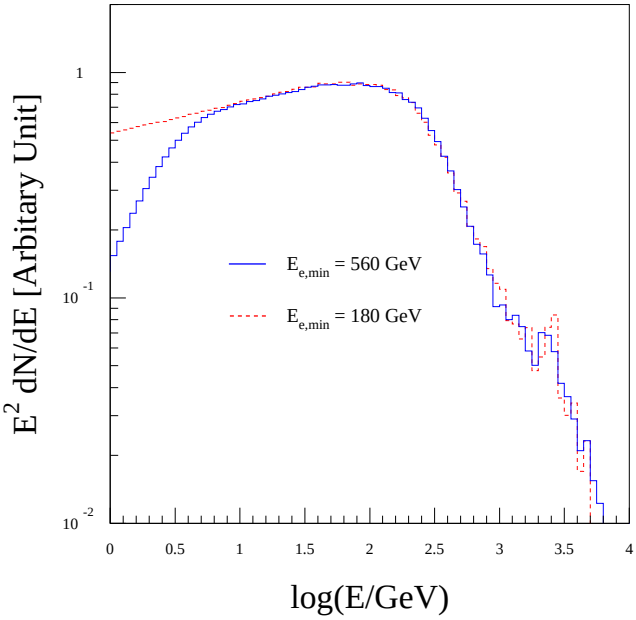

Figure 3.1: The pair halo gamma photon SED computed with $E_{e,\min} \approx 560$ GeV (solid blue line) and with $E_{e,\min} = 180$ GeV (red dashed line).

The computational time consumed for the case $E_{e,\min} \approx 180$ GeV is 5 times longer than that for the case $E_{e,\min} \approx 560$ GeV. If one injects one thousand primary gamma photons at energy 100 GeV, the total run time for one simulation is about 30 minutes for the computer hardware available for the current work. The statistical accuracy in the region $E > 1$ TeV in Fig. 3.1 is still low. To improve the statistical accuracy in the extreme high-energy region, the number of primary gamma photons must be increased, unavoidably increasing the computational time. A compromise can be obtained by considering the pair halo SED in the regions $E < 10$ GeV and $E > 10$ GeV separately. For $E < 10$ GeV, one can use a small number of primary photons but a low value of $E_{e,\min}$, while for $E > 10$ GeV a larger number of primary photons is required, but also a larger value for $E_{e,\min}$ is acceptable. Moreover, the $E > 10$ GeV energy range covers the effective energy region for the next generation imaging atmospheric Cherenkov telescopes system such as H.E.S.S. [Kon00], which is expected to be able to detect pair halos.

For each primary gamma photon, the algorithm follows the cascade devel-

opment through the following procedure:

1. An energy value is given for a primary gamma photon which will start the cascade from a specific source spectrum. Two types of primary photon distributions have been used in the current work. One is monoenergetic,

$$\frac{dN}{dE_\varepsilon} = \delta(E_\varepsilon - E_{\varepsilon 0}), \tag{3.8}$$

and the other is a power law distribution,

$$\frac{dN}{dE_\varepsilon} = \frac{-\alpha + 1}{{E_{\varepsilon 2}}^{-\alpha+1} - {E_{\varepsilon 1}}^{-\alpha+1}} \; {E_\varepsilon}^{-\alpha}, \tag{3.9}$$

where N is a sample number distribution, α is the power index and $E_{\varepsilon 1}$ and $E_{\varepsilon 2}$ are the upper and lower energy limits. The source of the VHE primary gamma photons is located at the origin, (0,0,0).

2. The free path lengths of the gamma photons are generated from the probability distribution

$$\frac{dN}{dr} = \frac{1}{\Lambda_{PP}} \exp(-r/\Lambda_{PP}), \tag{3.10}$$

where Λ_{PP} is a PP mean free path length which depends on the gamma photon energy and the spectrum of the background photon field, as given by Eq.(2.5).

3. The propagation direction for the gamma photon is given in spherical coordinates (r, θ, ϕ). Rather than using θ and ϕ, μ and ϕ are used because of their isotropic distribution in solid angle.

4. The interaction point is computed from the free path and propagation direction. At that point, the PP takes place and produces a $e^\pm$ pair. If the point is located out of the considered sphere with radius d_c, this pair will be abandoned and the algorithm considers other $e^\pm$s in the memory. If there are no $e^\pm$ in the memory, the algorithm will take the actions described in item no. 11. On the other hand, if there is a particle, the program will do as described in item no. 8.

5. A photon to be pair produced is generated. Since the sample space of the background photons that can interact with gamma photons is reduced by the PP cross section, the distribution used is the product of the background photon ($n(z, E_\omega)$) and the angle-averaged PP cross section ($\bar{\sigma}_{PP}$) in Eq.(2.13);

$$\frac{dN}{dE_\omega} = \eta_{PP}(z, E_\varepsilon, E_\omega) = \overline{\sigma}_{PP}(E_\varepsilon, E_\omega) n(z, E_\omega). \tag{3.11}$$

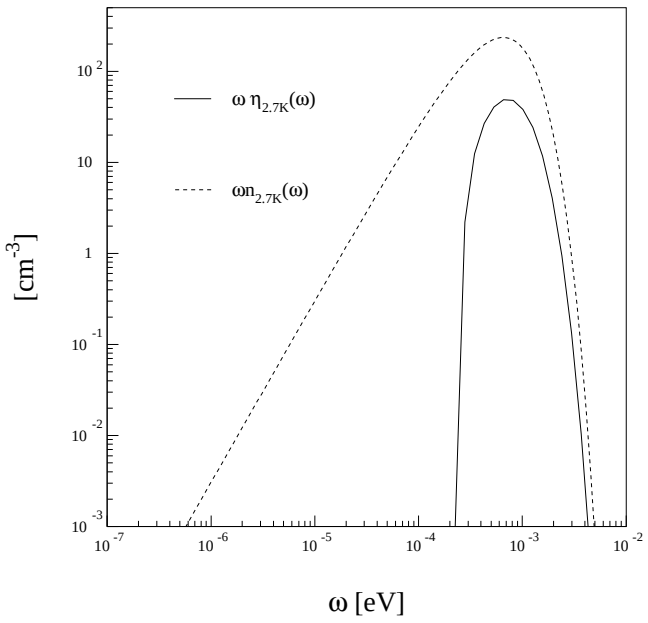

Figure 3.2: Comparison between η_{PP} and n for the case of 2.7 K background with $z = 0$ and gamma photon energy is 100 PeV.

6. Energies for the $e^{\pm}$ pairs are generated. At this stage E_ε and E_ω are known, and the spectrum of the produced $e^{\pm}$ in Eq.(2.23) is used to generate the energies for the $e^{\pm}$ pairs.

7. A particle from the pair, say e^{+}, is recorded. The parameters that need to be recorded are the particle energy and position. The other particle, e^{-}, is followed for the next interaction. This particle will be abandoned in the record when $E_e < E_{emin}$, after which the program looks for a new one. When there are no more particles in the record, the program will do as described in item no. 11.

8. A photon to be upscattered is generated. The distribution

$$\frac{dN}{dE_\omega} = \eta_{IC}(z, E_e, E_\omega) = \overline{\sigma}_{IC}(E_e, E_\omega) n(z, E_\omega), \tag{3.12}$$

is used, with $\overline{\sigma}_{IC}$ from Eq.(2.36). The free path for e^{-} does not need to be generated because in the model the $e^{\pm}$s gyrate only across a region which is very small relative to the size of the pair halo. Thus, it can be assumed that they remain at the point where they are produced. If the e^{-} energy is less than the energy limit in Eq.(3.7), the program will abandon this particle and follow the last $e^{\pm}$s in the record. The action taken by the program if there are no $e^{\pm}$ left in the record is discussed in item no. 11.

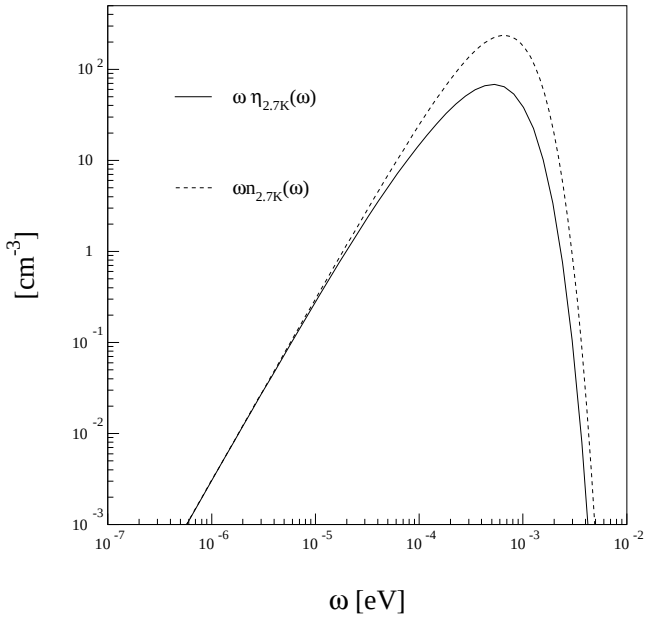

Figure 3.3: Comparison between η_{IC} and n for the case of a 2.7 K background with $z = 0$ and a gamma photon energy of 100 PeV.

9. An upscattered gamma photon is generated. The spectrum of the gamma photons from IC from Eq.(2.40) is used, where the e^- energy and soft photon energy values are already known. After obtaining the gamma photon energy, the energy of the e^- is subtracted.

10. The e^- is recorded, and the program follows the gamma photon. The gamma photon has a higher priority than $e^{\pm}$, in order that the cascade be followed. The gamma photon is followed and the procedure in items no. 2–6 is repeated.

11. When no particles remain in the record, the cascade is aborted and the computations are finished for one primary gamma photon.

During the monitoring of a cascade, several variables have to be computed; e.g., the propagation distances of the particles, the energy of the resulting particles in each interaction, and the soft photon energy w from the background field. The next section discusses the techniques used in the program to compute these variables.

3.2 Random Number Generator

In the current work, the Monte Carlo simulation uses two different random number generators. One is a transformation method, and the other a hit-or-miss method [Jam80].

3.2.1 Transformation Method

In order to generate random numbers from $f(x)$, the transformation method uses a normalized accumulated function of $f(x)$:

$$F(x) = \frac{1}{A}\int_{\acute{x}_{min}}^{x} f(\acute{x})d\acute{x}, \tag{3.13}$$

with a normalization factor

$$A = \int_{\acute{x}_{min}}^{\acute{x}_{max}} f(\acute{x})d\acute{x}. \tag{3.14}$$

The function $F(x)$ is a monotonically increasing function in the range 0 to 1. When a random number ξ has been chosen from a uniform probability distribution on the interval (0,1), the variable x can be calculated. In the case of $F(x)$ being an analytically invertible function, one can find x from

$$x = F^{-1}(\xi). \tag{3.15}$$

However, if $F(x)$ cannot be inverted, one can tabulate $F(x)$ and x and find the x-value corresponding to ξ by interpolation.

This method is used to generate the free path length of the particles, with a probability density which attains an exponential form,

$$f(x) = \Lambda^{-1}e^{-x/\Lambda}. \tag{3.16}$$

The normalized accumulated distribution is

$$F(x) = (1 - e^{-x/\Lambda}), \tag{3.17}$$

and the free path length can be produced by inverting the normalized accumulated function

$$x = -\Lambda \ln \xi, \tag{3.18}$$

where Λ is the free path length from Eq.(2.6) for PP and Eq.(2.30) for IC.

The transformation method is computationally efficient in one-dimensional problems, especially when $F(x)$ is an invertible function. There are, however, disadvantages of the method in multidimensional or many-variable problems, the reason being that in these cases the accumulated distribution cannot generally be inverted with respect to every variable. Typically, interpolating between tabulated values is practical only for functions with up to two variables.

3.2.2 hit-or-miss Method

The hit-or-miss method is the most simple technique for generating random numbers, provided there is a distribution $f(x)$ from which random numbers α can be taken. The procedure is as follows:

1. Two random numbers, α and ξ, within the intervals (x_{min}, x_{max}) and (y_{min}, y_{max}), are independently obtained from a uniform probability distribution.

2. The *hit-or-miss condition* is checked: if $\xi \leq f(\alpha)$ then α is accepted (hit), but if $\xi > f(\alpha)$ then α is rejected (miss).

The distribution of the accepted α will have the same shape as $f(x)$.

The necessary parameters are x_{min}, x_{max}, y_{min}, and y_{max}. However, in practice, at least in this simulation, only y_{max} is an unknown parameter. Hence, in this simulation before the program generates the random number from a distribution function $f(x)$ the program has to find the maximum value of $f(x)$, y_{max}.

The efficiency of the hit-or-miss technique depends on

$$p = \frac{\text{area under } f(x)}{\text{area of sample space}} = \frac{\int_{x_{min}}^{x_{max}} f(x)dx}{(x_{max} - x_{min}) \times (y_{max} - y_{min})}. \qquad (3.19)$$

When $p \approx 1$, the area under the curve $f(x)$; i.e., the "hit" area, is nearly the same as the sample space area. Most of the sample in the sample space is in the hit area. In contrast, if $p < 0.5$, most of the sample is in the "miss" area, and the program has to generate random numbers many times to get a satisfactory value.

One advantage of this technique, and the main reason that it was chosen for the current work, is that it can be applied for many-parameter problems, such as is the case for the pair halo model.

In PP, the hit-or-miss technique is applied for two tasks. One is to generate the energy of the pair produced $e^{\pm}$ from Eq.(2.23), which depends on two parameters (γ and w) and one variable (E_{ee}). From Fig. 2.4, it is seen that this method is very efficient when s_0 is a low value. Fortunately, most of the PP processes in the pair halo model concerns such cases.

The other task is to generate soft photons from the background photon distribution. For this task, the methodology that was suggested in [Pro86] has been applied, where the soft photons are generated from a modified background photon distribution, $\eta_{PP}(E_\varepsilon; w)$ in Eq.(3.11). Here, $p < 0.5$, so this technique is not particularly efficient. However, because the program deals with a number of PP which is much lower than that of IC, it is still acceptable to use this technique for generating soft photons.

In IC, the hit-or-miss technique is applied only in order to generate the energy of the upscatter gamma photons from Eq.(2.40). As seen from Fig. 2.8, this method is not very efficient in the Klein-Nishina regime, but it is quite good

in the Thomson regime, especially in the case of b < 10. Fortunately, most of the IC processes in the cascade are within the last regime.

The hit-or-miss method is not appropriate for generating the IC interacting soft photons from the modified background photon field η_{IC}, as in Eq.(3.12). This is partly due to the fact that $p \ll 1$ for the modified background photon distribution, but also because most of the interactions that occur in the program are IC in the Thomson regime. Thus, the computational demands here are high. The hit-or-miss method together with the comparison function technique; e.g., [PTVF94], is needed to solve this problem.

Such a technique can be used to improve the random number generated from the hit-or-miss method, especially in the case of $p \ll 1$. The idea is to apply a transformation method to generate random numbers α from a distribution function $g(x)$ that has the following properties:

1. $g(x) > f(x)$ for all x

2. $g(x)$ is an integrable function for which the accumulated distribution invertible.

When α is generated, $g(\alpha)$ will be set equal to y_{max}. Then isotropically distributed random numbers ξ from (y_{min}, y_{max}) are generated. The *hit-or-miss condition* is applied to ξ in order to select α from the distribution $f(x)$. The efficiency of this technique depends on how close the function $g(x)$ is to $f(x)$. This technique can be modified for application to problems that have many parameters by finding an integrable function $g(x)$ which satisfies $g(x) > f(x_1, x_2, ..., x_n; x)$ for all x and all parameters $x_1, ..., x_n$.

3.3 Collecting Data

Strategy

A specific strategy has been adopted for collecting data from the simulation, in order to reduce the number of primary gamma photons; i.e., computation time. The strategy is based on the fact that the halo is spherically symmetric, and thus observing from any direction from a given distance yields the same picture. An observer located at a sphere with a radius equal to the distance between the VHE gamma source and the observer, d_s, is formed, with the VHE photon source located at the center of the sphere. During the simulation, whenever gamma photons cross the observer sphere, this implies that the observer can detect these photons. Therefore, information on these gamma photons is recorded. Gamma photons crossing the observer sphere are allowed to continue cascading, and the photons they subsequently produce, can reach the observer.

Following this strategy, there are two important observable quantities from the pair halo that can be computed. One is the energy of the observable gamma photons, and the other is their angular distance from the source, θ. The algorithm used to compute these quantities will be introduced below. Not only does

this scheme reduce the number of particles needed in the simulation, but it also yields a particularly efficient computation of the angular photon distribution.

Pair Halo Angular Distance Determination

As shown in Fig. 3.4, the normal vectors on the observer sphere are always in the same direction as the line of sight. Therefore, the angle between the photon direction of propagation and the normal vector can be interpreted as the angular distance of the observed gamma photons from the VHE source.

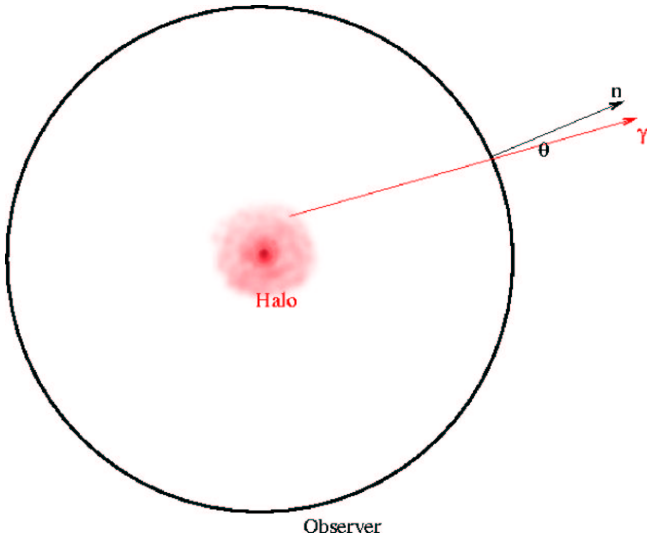

Figure 3.4: Geometry picture shows how to collect data from the simulation.

If gamma photons, produced at $\mathbf{r}_0$ and propagated through a distance D in the direction $\hat{\mathbf{k}}_\gamma$, cross the observer sphere (with radius R), the condition

$$(\mathbf{r}_0 \cdot \hat{\mathbf{k}}_\gamma)^2 + R^2 - r_0^2 > 0 \tag{3.20}$$

has to be satisfied. If Eq.(3.20) is not satisfied, the gamma photons never cross the observer sphere. Otherwise, the distance between the point where the gamma photons were produced and the crossing point can be calculated from

$$d = -(\mathbf{r}_0 \cdot \hat{\mathbf{k}}_\gamma) \pm \sqrt{(\mathbf{r}_0 \cdot \hat{\mathbf{k}}_\gamma)^2 + R^2 - r_0^2}. \tag{3.21}$$

For $d < 0$, the gamma photon propagates in the direction opposite to $\hat{\mathbf{k}}_\gamma$, and this case is rejected. If $d > D$, the gamma photons interact with a soft photon before reaching the crossing point; otherwise the real crossing point can be calculated by

$$\mathbf{r}_1 = \mathbf{r}_0 + d\,\hat{\mathbf{k}}_\gamma. \tag{3.22}$$

At this point the angle θ is given by

$$\cos\theta = \frac{\mathbf{r}_1 \cdot \hat{\mathbf{k}}_\gamma}{|\mathbf{r}_1|}. \tag{3.23}$$

Note that because the probability density in θ-space is proportional to $\cos\theta$, the histogram in this case has to be weighted by the factor $|\cos^{-1}\theta|$. For more detail, see Appendix B.

3.4 Sample Monte Carlo Simulation

In this section, the results of a simulation will be explained in detail, together with the underlying assumptions. The source H1426+428 is a BL Lacertae object at z=0.129, and is here assumed to be a VHE gamma ray source producing a pair halo.

Source luminosity	$L_0 = 10^{45}$ erg/s
Primary gamma photon spectrum	Monoenergetic $(dN/dE)_{source} \propto \delta(E - E_0)$ $E_0 = 100$ TeV
CIB model	Primack et al.,2000
Redshift	0.129

Table 3.1: Summary of the quantities and parameters used in the program for a preliminary simulation run.

The parameters that have been used for the sample Monte Carlo simulation are summarized in Table 3.1. In subsequent sections, these input parameters will be presented in a similar fashion. Several reports on H1426+428 [A$^+$02a, DA$^+$02, H$^+$02] show energy fluxes over several energy bands of order $10^{43} - 10^{44}$ erg/s. For this example, we assume unboosted, isotropic emission, which gives a source luminosity $L_0 \approx 10^{45}$ erg/s. The infrared background photon field from [PSBD00] using the Salpeter initial mass function (IMF), as illustrated in Fig. 3.5(a), is also consistent with the redshift value of $z = 0.129$. The mean free path length with respect to the background photon field for both PP and IC is presented in Fig. 3.5(b). In both figures, the quantities have been calculated from Eq.(2.6) for PP and Eq.(2.30) for IC.

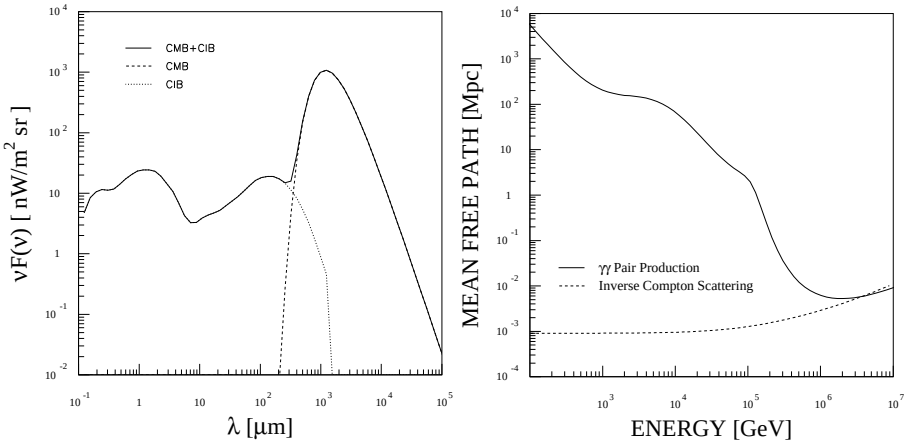

Figure 3.5: Left panel: (a) The background photon field at z=0.129. The CIB component is from [PSBD00]. Right panel: (b) The mean free path length of gamma photons with respect to PP, and of $e^{\pm}$ with respect to IC, given the background photon field.

Figure 3.6(a) and (b) show a sample SED and angular distribution for a pair halo using simulated data. Below, the assumptions and approximations used for producing these figures are discussed.

The main assumption used to obtain the pair halo energy flux is that the cascade is in a steady state, implying a constant primary VHE photon flux from the central source. The steady-state has been used in several previous works on cascades; e.g., [AKUV85, Pro86, Zdz88]. The observed pair halo gamma-ray luminosity is then proportional to the luminosity of the VHE primary gamma photons, and one obtains

$$\mathrm{L}_0 = k\mathrm{E}_s, \tag{3.24}$$

where k is a constant used to convert energy to luminosity, and

$$\mathrm{E}_s = \int_{\mathrm{E}_1}^{\mathrm{E}_2} dE\ E \left(\frac{dN^{\dagger}}{dE}\right)_{source}, \tag{3.25}$$

with $N^{\dagger}$ being the number of primary photons used in the simulation. At this point, it should be noted that in the numerical code the integration in Eq.(3.25) is computed via a summation, which is practical for a histogram representation. Since the histograms are presented in logarithmic scale, the summation is given by

$$\mathrm{E}_s = \sum_{i=1}^{n} \Delta \log E_i\ E_i \left(\frac{N_i^{\dagger}}{\Delta \log E_i}\right)_{source}, \tag{3.26}$$

where $N_i^{\dagger}$, E_i, and $\Delta \log E_i$ are respectively the photon number, the mean energy, and the logarithmic bin size of the i^{th} bin. The mean energy of the first

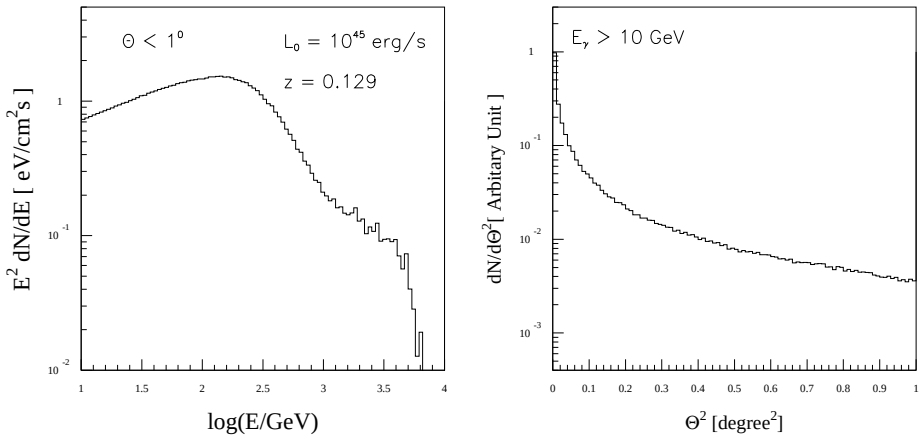

Figure 3.6: Left panel:(a) The spectral energy distribution of the observed gamma photons from the halo within 1°. Right panel:(b) Angular distribution of observed pair halo gamma photons with energy above 10 GeV.

and last bin correspond to $\log \mathrm{E}_1$ and $\log \mathrm{E}_2$, respectively. The corresponding SED becomes

$$E^2 \frac{dN^\dagger}{dE} \approx E_i \left(\frac{N_i^\dagger}{\Delta \log E_i} \right). \tag{3.27}$$

Equation (3.27) is used to represent the energy distribution throughout this work. During a cascade, the total primary gamma photon energy is converted into three forms: pair halo gamma photon energy E_{halo}, pair energy E_e, and survival primary gamma photon energy E'_s;

$$\mathrm{E}_s = \mathrm{E}_{halo} + \mathrm{E}_e + \mathrm{E}'_s. \tag{3.28}$$

Analogously with E_s, E_{halo} can be calculated from

$$\mathrm{E}_{halo} = \sum_{i=1}^{n} \Delta \log E_i \; E_i \left(\frac{N_i^\dagger}{\Delta \log E_i} \right)_{halo}, \tag{3.29}$$

where the first and last bin correspond to 10 GeV (the chosen minimum value) and the pair halo maximum energy, respectively.

The luminosity of the pair halo gamma photons,

$$\mathrm{L}_{halo} = k\mathrm{E}_{halo}, \tag{3.30}$$

is related to the source luminosity via

$$\frac{\mathrm{L}_{halo}}{\mathrm{L}_0} = \frac{\mathrm{E}_{halo}}{\mathrm{E}_s}. \tag{3.31}$$

From this relation, the pair halo luminosity can be found, and the pair halo flux can be calculated via

$$\begin{aligned} \mathrm{F}_{halo} &= \kappa \mathrm{E}_{halo} \\ &= \sum_{i=1}^{n} \Delta \log E_i \; \kappa E_i \left(\frac{N_i^{\dagger}}{\Delta \log E_i} \right)_{halo}, \end{aligned} \tag{3.32}$$

where

$$\kappa = \frac{\mathrm{L}_0}{\mathrm{E}_s 4\pi d_s^2}. \tag{3.33}$$

The factor κ is used to convert the energy into energy flux, and thus yield the pair halo SED:

$$E^2 \left(\frac{dN}{dE} \right)_{halo} = \kappa E_i \left(\frac{N_i^{\dagger}}{\Delta \log E_i} \right)_{halo}, \tag{3.34}$$

where N is the particle flux received at the observer sphere.

The spectral energy distribution of the pair halo gamma photons can be divided into two regions with respect to the SED maximum point, E* [ACV94]. As seen from Fig. 3.6(a), E* $\approx$ 150 GeV. The region of the SED where the photon energies are above E*, hereafter referred to as the *high energy region* (HER), contains information about the CIB.

The flattening at $E > 1$ TeV of the SED, for example, shows the influence of the mid-infrared part of the background photon field, which has the form $n(E_\omega) \propto {E_\omega}^{-1}$, as seen from Fig. 3.5(a). For such the background spectrum, the PP optical depth (see Eq.(2.15) and (2.16)) will not depend on gamma photon energy any more. Therefore, the flattening arises in this energy range. This flattening feature will pay an important role in order to constrain the CIB in mid-infrared region which has the highest uncertainty because of the zodiacal light in local solar system.

Figure 3.7 shows that most of the photons in the HER are in the center of the halo, while photons with energy lower than E*; hereafter referred to as the *low energy region* (LER), come from all angles. This fact is confirmed by the angular distribution, as discussed below.

The photon angular distribution is arguably the most important prediction of the pair halo model. Figure 3.6(b) shows the angular distribution at energies above 10 GeV within 1°. As seen from the figure, the population of gamma photons is concentrated towards the center of the halo. The angular distribution satisfies the normalization

$$\int_{\Omega} \frac{dN(E \geq E_l)}{d\Omega} \, d\Omega = 1, \tag{3.35}$$

where $\Omega = 4\pi$ is the solid angle of the whole sphere and the limiting energy has been set to $E_l = 10$ GeV for every differential angular distribution presented in this work.

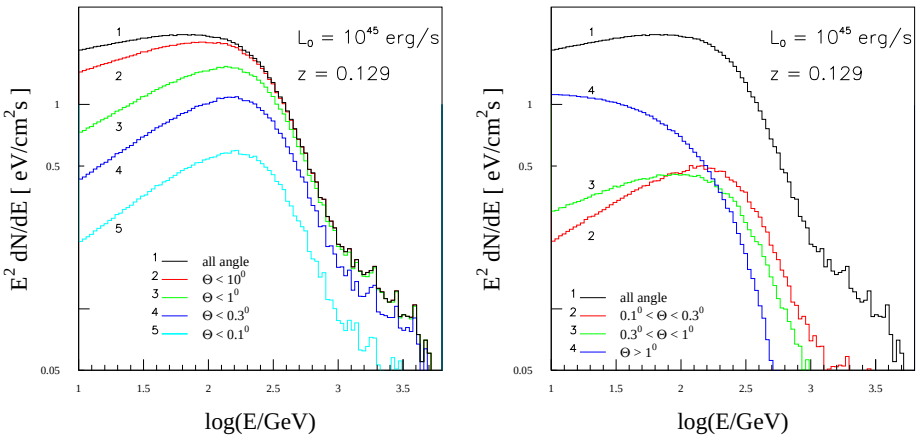

Figure 3.7: Left panel:(a) The pair halo SED for different opening angle size. Right panel:(b) The same SED in different angular regions.

The angular distribution can be fitted by a polynomial function

$$\frac{dN}{d\theta^2} = \frac{a_1}{\theta^2} + \frac{a_2}{\theta} + a_3 + a_4\theta, \tag{3.36}$$

where a1,..., a4 are fitting parameters. For the angular distribution in Fig. 3.6(b), the parameters are presented in Table 3.2. In some simple cases, further dis-

a_1	a_2	a_3	a_4
0.152×10^{-4}	0.521×10^{-1}	4.05	-332.5

Table 3.2: Summary on the fitting parameters of the angular distribution in Fig. 3.6(b). These parameters were calculated using the normalization given by Eq.(3.35).

cussed in Appendix C, the angular distribution is given to a good approximation by using only the second and third terms. The gamma photon angular distribution at different energies is shown in Fig. 3.8(a). The figure reveals that the flux and statistical accuracy decrease with increasing energy. This result is as expected.

However, from an observational point of view a more interesting property is the shape of the angular distribution. For the energies 10 and 100 GeV, the angular distributions do not deviate substantially, while those at 10 GeV and 1 TeV have rather different profiles. For example, at 10 GeV the flux at $\theta = 0°$ is two orders of magnitude above that at $\theta = 1°$, and at 1 TeV the difference is three orders of magnitude. This implies that the larger the angle, the smaller is the high energy flux. This conclusion can be drawn by inspecting the normalized

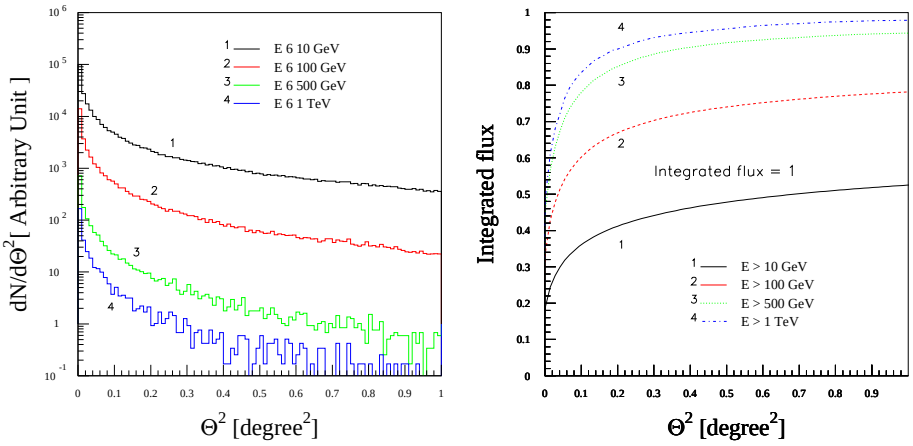

Figure 3.8: Left panel:(a) Gamma photon angular distribution at different energies. Right panel:(b) Cumulative angular distribution at the same energy. Note that " Integrated flux = 1 " implies that the cumulative angular distribution equals unity when $\theta = 180°$.

cumulative angular distribution, which is plotted in Fig. 3.8(b). In this figure, a different normalization has been used for the various curves; with E_l being respectively 10 GeV, 100 GeV, 500 GeV and 1 TeV. The curves reveal how the halo gamma photons with energy above E_l are distributed over the plane of the sky.

The surface brightness of the halo for different energies is represented in Fig. 3.9. Although these plots are less applicable for quantitative analysis, they give crucial keys to how a halo would appear observationally. To obtain the surface brightness, the azimuthal angles ϕ have been randomized from the uniform probability distribution from 0 to 2π. Each observed gamma photon has been put in the x-y plane at a position given by

$$x = \theta \cos\phi \tag{3.37}$$

$$y = \theta \sin\phi. \tag{3.38}$$

Note that the resolution in the figure is $\Delta x = \Delta y = 0.1°$, which is approximately the same as the resolution of HEGRA and H.E.S.S. [Kon00] Čerenkov telescopes.

The very highly concentrated flux at the halo center is seen at every energy range, as evident from Fig. 3.9. Using this property, together with the fact that the specific gamma photon flux increases towards lower energies (as seen from Fig. 3.8), a pair halo is most easily detected via the lower energy gamma photons. This is an advantage for searching after blazar-type objects with their jets not pointing towards the Earth.

It is conceivable that when observing with a gamma ray telescope with a low energy threshold, say 100 GeV as for H.E.S.S., one would see a large number of halos on the sky which unveil hidden blazar-type objects. The flux from the

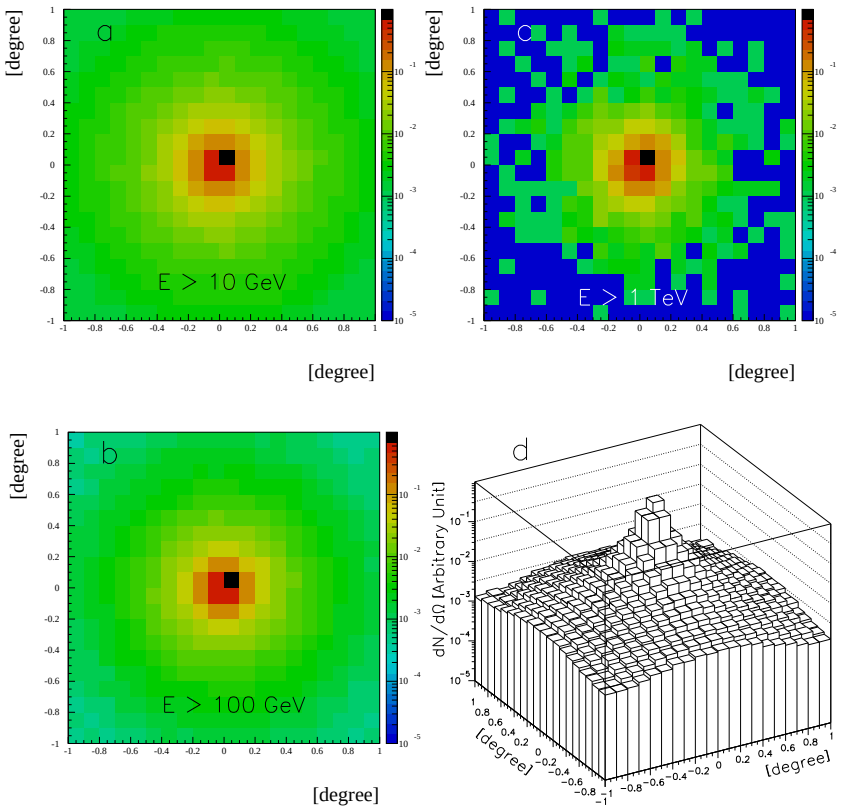

Figure 3.9: Left panel: Surface brightness of the pair halo for energies 10 GeV and 100 GeV. In the text, these plots are referred to as (a) and (b). Right panel: Surface brightness of the pair halo for energy 1 TeV, and a 2-dimensional histogram of the surface brightness corresponding to (a). In the text, the plots are referred to as (c) and (d).

halos can be used to estimate the luminosity of the central engine. Since the photons from the VHE sources cannot be observed directly, the gamma photon flux has a contribution only from the halo.

Figure 3.10 shows the angle-energy relationship for the pair halo gamma photons. As seen from this plot, the characteristic size of the halo decreases with increasing photon energy.

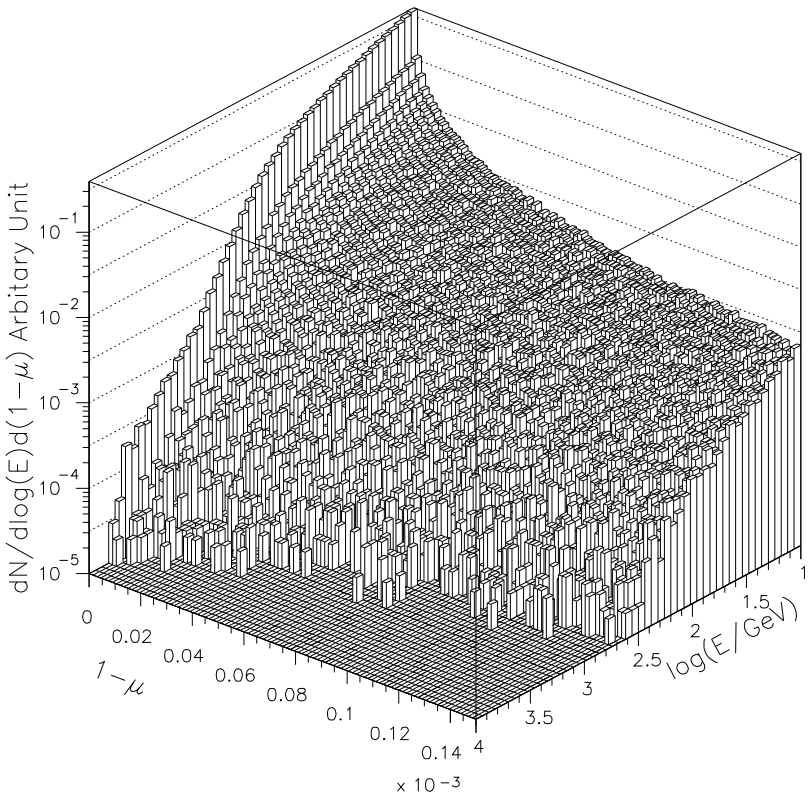

Figure 3.10: Two-dimensional histogram showing the pair halo gamma photon population in $1 - \mu$ (reaching up to 1°) and energy space, for the case of monoenergetic primary gamma photons with an energy of 100 TeV.

3.5 Simulation for High Redshift Sources

Source luminosity	$L_0 = 10^{46}$ erg/s
Primary gamma photon spectrum	Monoenergetic $(dN/dE)_{source} \propto \delta(E - E_0)$ $E_0 = 100$ TeV
CIB model	Primack et al.,2000
Redshift	2

Table 3.3: Summary of the quantities and parameters used in the program for the high redshift case.

In the case of high redshift sources, the Monte Carlo simulations become more involved, because some cosmological effects can no longer be neglected. For high redshift problems, two variables must be modified in the simulation. First of all, one must account for the redshift of the observed photon energy,

$$E_\varepsilon = \frac{E_{\varepsilon z}}{1+z}. \tag{3.39}$$

Secondly, the angular distance involves the cosmological redshift;

$$\Delta\theta = \frac{d(1+z)}{D_c}, \tag{3.40}$$

where d is size of the object and D_c the coordinate distance.

However, a more serious difficulty that arises for high redshift sources is that the assumption of a non-evolving background photon field along the propagation path no longer holds. To account properly for the background photon field, soft photons have to be generated all along the line of propagation, which involves redshifts from z to 0.

Instead of simulating all interactions in the cascade from the source to the observer, the algorithm follows the cascade in a certain region around the source. In the program, this region is defined to be sphere with radius $r = D_c\Delta\theta$, using $\Delta\theta = 5^\circ$ and assuming that within this region the CBR is in the same epoch as the source and does not change significantly.

The flux of gamma photons from a cascade in this region is set to be the primary halo gamma photon flux, $F_1(E_\varepsilon)$, using the relation in Eq.(3.32) with

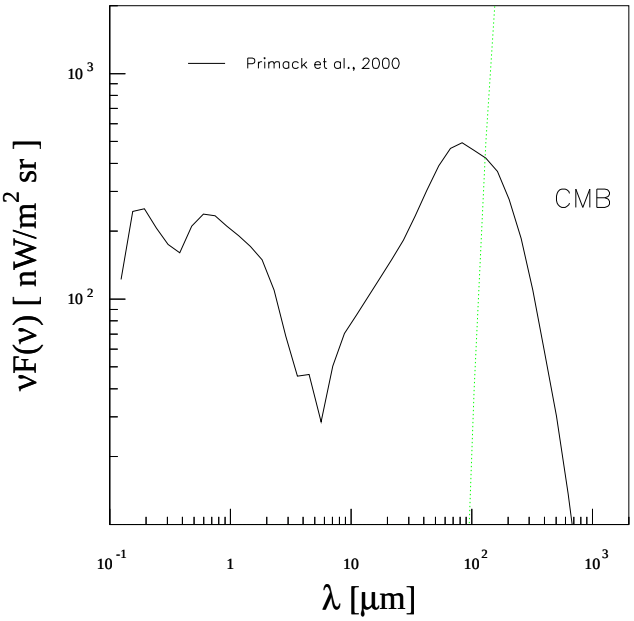

Figure 3.11: Cosmic background radiation at $z = 2$, for the energy range corresponding to the CIB region.

the new flux-energy conversion factor, κ_z, which accounts for the cosmological redshift:

$$\kappa_z = \frac{\kappa}{(1+z)^2}, \tag{3.41}$$

where κ has been defined in Eq.(3.33). The factor $(1+z)^{-2}$ converts the coordinate distance D_c into the luminosity distance, D_l which already includes the cosmological expansion. This is further discussed in Appendix A.

The observed halo gamma photon flux, $\mathrm{F}_{halo}(E_\varepsilon)$, can be calculated by multiplying the primary halo gamma photon flux with the opacity factor, $\exp(-\tau_{PP})$;

$$\mathrm{F}_{halo}(E_\varepsilon) = \mathrm{F}_1(E_\varepsilon)\exp(-\tau_{PP}), \tag{3.42}$$

where τ_{PP} is calculated from Eq.(2.22). This leads to an abrupt high-energy cutoff. However, this method differs from that used in the low-redshift simulations, since it is not entirely self-consistent; the energy of high-energy photons interacting with the CBR via PP is not added to the SED. Nevertheless, at high and moderate energies this method produces accurate results.

The results from the simulation from the above scheme are presented in Figs. 3.11– 3.15, with the parameters given in Table 3.3.

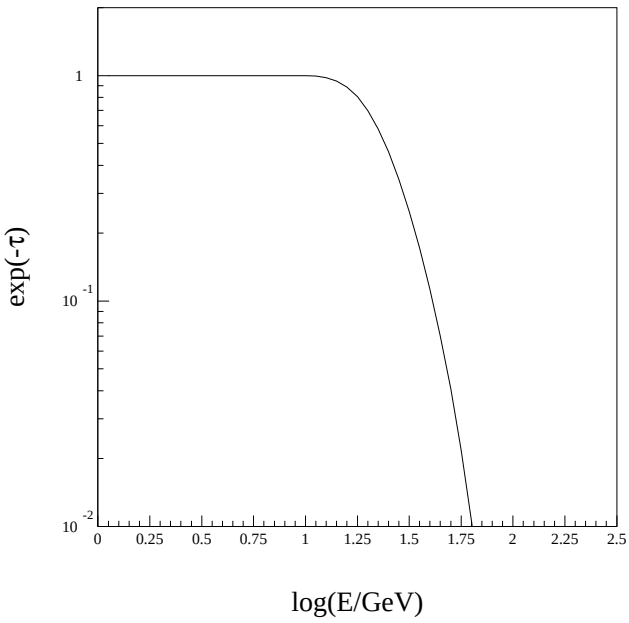

Figure 3.12: Attenuation factor corresponding to the CBR in Fig. 3.11.

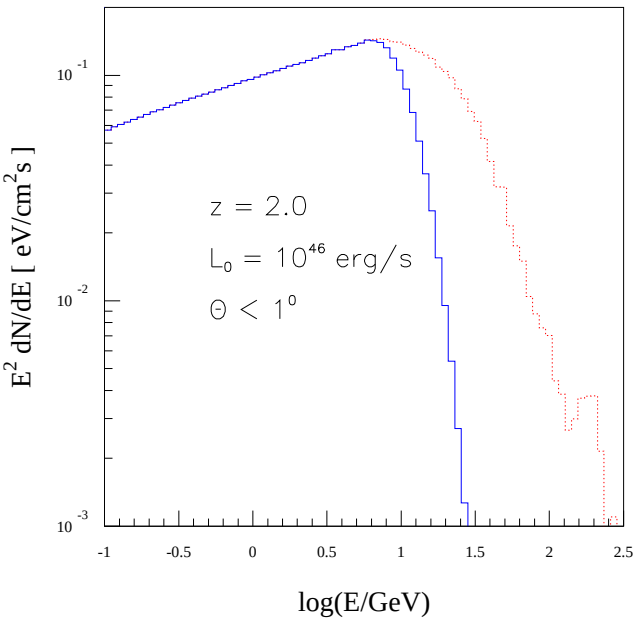

Figure 3.13: The pair halo SEDs from a monoenergetic source at $z = 2$ before (dotted line) and after (solid line) suffering absorption from the IGM.)

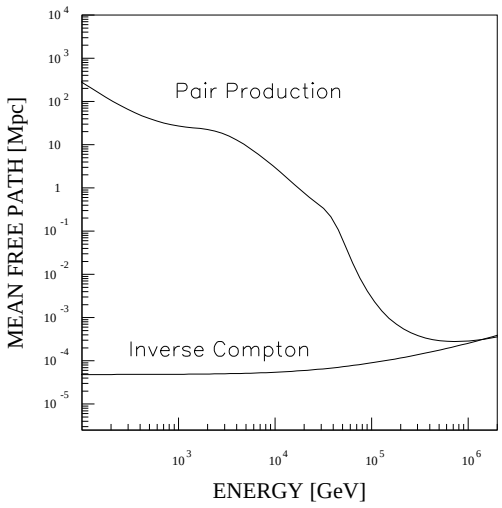

Figure 3.14: The PP and IC mean free path length for different energies corresponding to the CBR in Fig. 3.11.

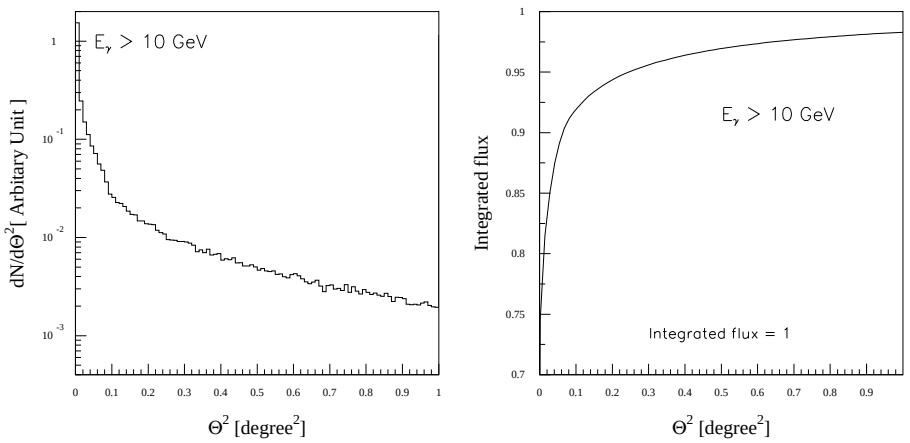

Figure 3.15: Left panel: The differential angular distribution from the pair halo at $z = 2$. Right panel: The corresponding cumulative angular distribution.

Chapter 4

Pair Halo Study

There are three main parameters that can affect the energy and angular distribution of a giant pair halo;

1. the initial primary VHE gamma photon energy distribution
2. the background photon field or the cosmic background radiation (CBR) composed by the cosmic microwave background (CMB) and the cosmic infrared background (CIB),
3. and the distance between the gamma rays source and the observer, indicated by the redshift.

The first two quantities are especially uncertain and not easily accessible by measurements. It is of particular interest to determine how these quantities affect pair halos to study the sensitivity of pair halo characteristics to these parameters.

4.1 Pair Halos from Different Source Spectra

4.1.1 Monoenergetic Distribution Sources

In this section, a pair halo will be studied for different mono-energetic injected primary gamma photons. Table 4.1 summarizes the assumed luminosity (L_0), energy of the injected photons (E_0), CIB model, and redshift. In the second row of the table, E_0-values are shown in different colors and plotted with lines corresponding to those used in other figures. The infrared background photon field model and redshift are the same as in the previous section, for which the background and mean free path are shown in Fig. 3.5.

Table 4.2 shows (for each E_0) the pair halo (L_{halo}) and absorbed flux luminosity (L_{abs}) in percent of the total source luminosity. The E_0 = 100 and 500 TeV cases have no surviving primary gamma photons, and since the number

Source luminosity	$L_0 = 10^{45}$ erg/s
Primary gamma photon spectrum	Monoenergetic $(dN/dE)_{source} \propto \delta(E - E_0)$ E_0 = 10 TeV (solid line) E_0 = 100 TeV (dashed line) E_0 = 500 TeV (dotted line)
CIB model	Primack et al.,2000
Redshift	0.129

Table 4.1: Summary of quantities and parameters used in the simulation program, for the case of halos with (different) monoenergetic sources.

of injected primary gamma photon are 10^4 and 1.8×10^3 respectively, L_{abs} can only be said to be less than 10^{-2}% and 5.6×10^{-2}% respectively.

Consider first the 10 TeV monoenergetic case. Comparing the spectral energy distribution (SED) in Fig. 4.1(a) and (b), it is evident that when one considers pair halo angular distances $\theta \leq 180°$, the SED is higher than when considering only $\theta \leq 1°$ over the whole energy interval. The SED peak is also somewhat higher in the $\theta \leq 180°$ case than in the $\theta \leq 1°$ case.

The situation is different at higher energies. For the cases of monoenergetic injection at 100 or 500 TeV, practically all photons in the high energy region (HER) are produced near the center of the halo. Moreover, Fig. 4.2 shows that within 1° ($1 - \mu \approx 1.5 \times 10^{-4}$) the highest energies for each angle are more or less the same, in contrast with the results shown in Fig. 3.10 where a similar distribution is shown for the case of monoenergetic injection at 100 TeV. This may imply that the corresponding $e^{\pm}$s have roughly the same energy. Note that Fig. 3.10 and Fig. 4.2 show results from identical situations, except for the energy of the primary gamma photons. The $E_0 = 10$ TeV case can be considered as a single-generation cascade pair halo, since the PP mean free path length is about 100 Mpc, which is the same order as the source distance and larger than the radial distance of about 10 Mpc which corresponds to an opening angle is 1°. The next generation PP will take place with more or less the same mean free path, see Fig. 3.5(b). By then most of the second generation $e^{\pm}$s have escaped the region corresponding to 1°. The first generation $e^{\pm}$s interact with the CMB soft photons in the Thomson regime producing continuous secondary gamma

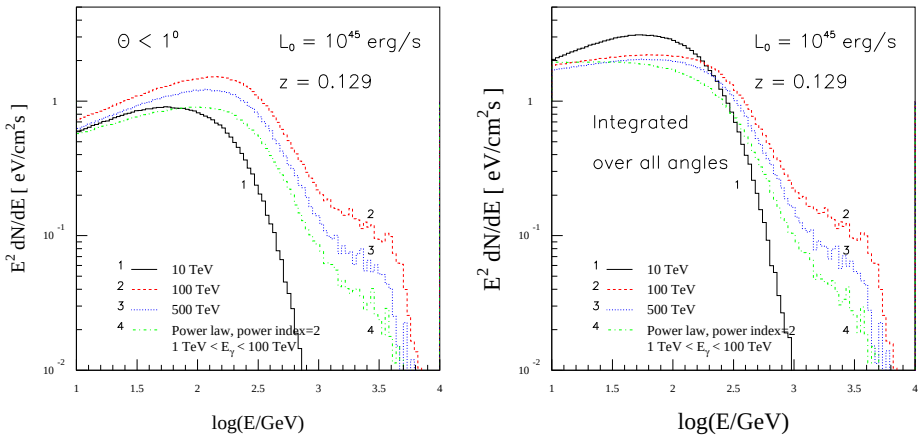

Figure 4.1: Pair halo gamma spectral energy distributions (SEDs) from a source located at $z = 0.129$ with luminosity $L_0 = 10^{45}$ erg/s for the cases of monoenergetic and power-law distributions of emitted primary gamma photons as function of energy in unit GeV; (a) $\theta < 1°$ and (b) $\theta < 180°$ are presented in left and right panels respectively.

photon energy distribution. Therefore, it can be said that the spectrum of the pair halo gamma photons in this case is the IC spectrum of the first generation cascade $e^{\pm}$s.

In the cases of $E_0 = 100$ and 500 TeV the PP mean free path of the primary photons are smaller than 10 Mpc; i.e., 2 Mpc and 10 kpc respectively. This means that several generations of cascades have already developed at the center of the pair halo. Therefore, only gamma photons near the center of the halo have energies up to the maximum, whereas the outer parts of the halo contain only low-energy gamma photons.

An interesting result evident from Fig. 4.1(a) is that in the whole energy range considered, the gamma photon flux from the $E_0 = 100$ TeV case is greater

N_γ	E_0	L_{halo} ($E > 10$ GeV)	L_{abs}	$\Theta_{90\%}$ ($E > 100$ GeV)
10^5	10 TeV	30.1%	0.03%	11.7°
10^4	100 TeV	28.9%	$< 10^{-2}$%	4.6°
1.8×10^3	500 TeV	29.0%	$< 5.6 \times 10^{-2}$%	4.6°

Table 4.2: The Table shows the injected number of photons (N_γ) the luminosity of the pair halo (L_{halo}) and the absorbed (L_{abs}) flux in unit of percent of the source luminosity (L_0), and the angular distance that contains 90% flux of the pair halo gamma photons with energy more than 100 GeV for different monoenergetic distributions with different E_0.

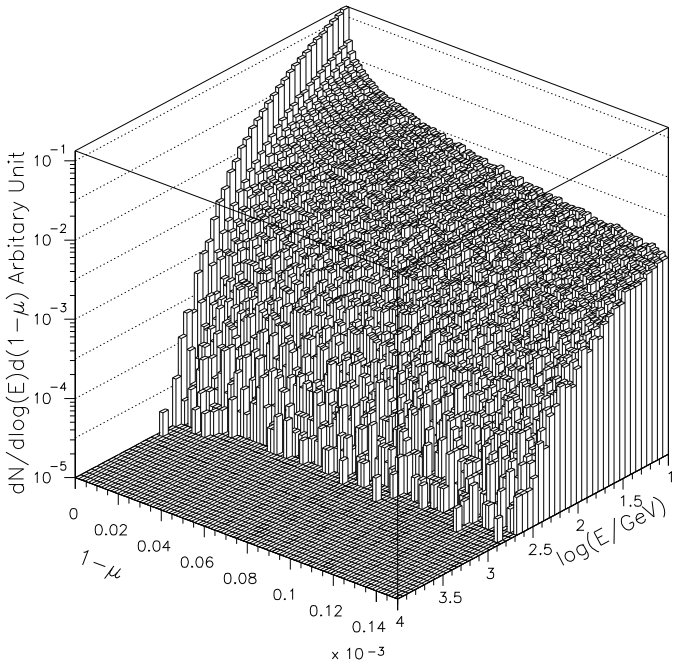

Figure 4.2: The pair halo gamma photon distribution plot in $1-\mu$ (reaching up to 1°) and energy space from the monoenergetic case with an energy of 10 TeV.

than that in the E_0 = 500 TeV case. The reason is that the 500 TeV gamma photons can interact with the CMB which has a much higher number density and consequently the PP mean free path is very short (Λ_{PP}(500 TeV) $\approx$ 10 kpc). Many generations of the cascade are produced at the core of the halo and lead to a rather different energy spectrum for the gamma photons than for the E_0 = 100 TeV case. It is known that the differential energy distribution of the gamma photons from the cascade in an optically thick medium is a power law with index 1.5 [BG70, Zdz88, AAN83] , see more explanation below. While there are several cascade generations in the E_0 = 100 TeV case, the number of the gamma photons which generate observed gamma photons is bigger than in the case of E_0 = 500 TeV. Therefore, the SED from 10 GeV to several TeV of the E_0 = 100 TeV case is higher than the E_0 = 500 TeV case even integrated over all observing angles.

The conclusion from the E_0 = 500 TeV case motivates a comparison with the case E_0 = 1 PeV monoenergetic source. As shown in Fig. 4.3, the SED and the pair halo gamma photon angular distribution are identical in both cases. In both cases the primary gamma photons are totally absorbed close to the source and develop cascades over many generations. After that they form the same energy distribution as the gamma photons. From this result, one can see that the pair halos from a very high energy, say more than about 500 TeV, have the

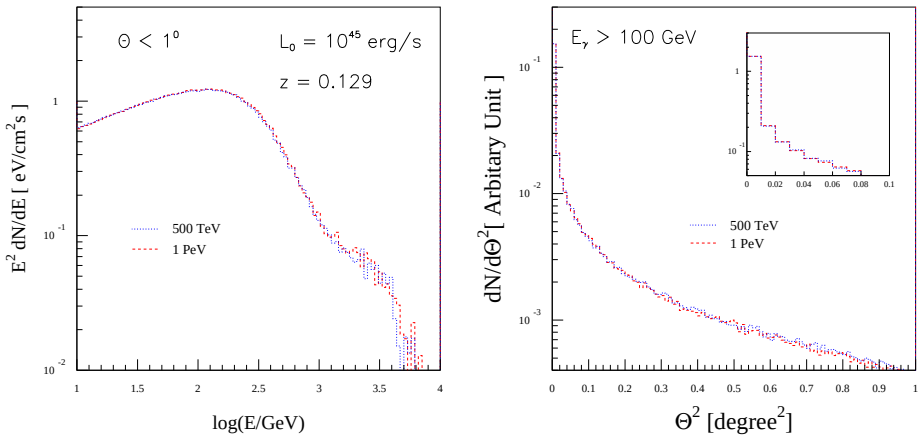

Figure 4.3: Comparison of the SED and angular distribution between the case of 500 TeV and 1 PeV monoenergetic primary gamma photon sources.

identical energy and angular distribution.

The monoenergetic distribution is converted immediately into a power-law distribution which will then in turn produce a larger halo than in the E_0 = 100 TeV case. Since the cascade SED follows a power-law with index 1.5, it is reasonable to expect that the SED and angular distribution of the pair halo gamma photons from both the power law and the 500 TeV monoenergetic case should be approximately the same. Figure 4.4 shows the comparison, and supports this expectation. However, there are some differences between the power law and monoenergetic case, as shown in Fig. 4.4(b). In the first bin of the histogram, the flux from the monoenergetic case is higher than in the power law case, while in other bins it is lower. The essential reason is that in the monoenergetic case the whole first generation cascade is initiated in the first bin, while in the power law case the primary gamma photons may initiate cascades at larger distances.

It might be concluded here that in a monoenergetic source with very high energy, high enough to pair produce with CMB, the first pair halo forms close to the core. The original, monoenergetic injected spectrum is converted into a power-law and initiates in turn a cascade nearby indistinguishable from a power-law injection.

On the other hand, when E_0 is not high ($E_0 < 100$ TeV), the pair halo SEDs are very sensitive to the injected photon energy as shown in Fig. 4.5

The differential and cumulative angular distributions for the E_0 = 10, 100 and 500 TeV monoenergetic cases are shown in Fig. 4.6 in different energy cuts. The E_0 = 10 TeV case is used as a reference, since it gives a single-generation cascade, and thus the corresponding angular distribution can be found analytically (see Appendix C). The deviation of the differential angular distribution in the E_0 = 100 and 500 TeV cases from the E_0 = 10 TeV case is

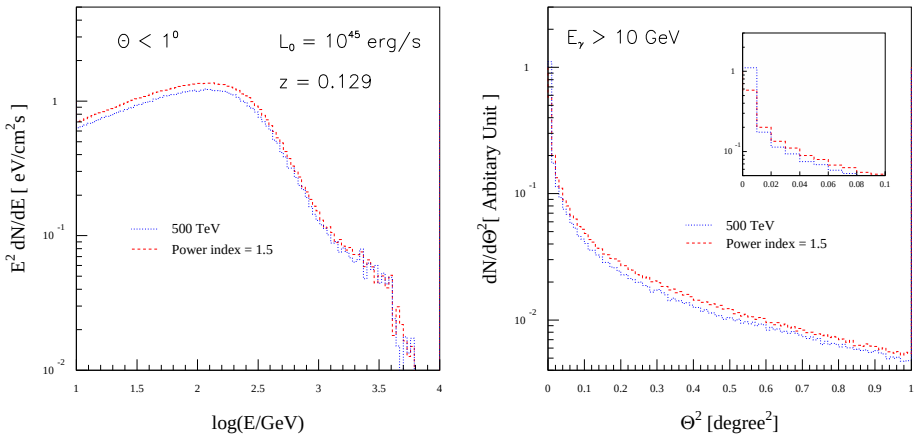

Figure 4.4: Comparison of the SED and angular distribution between the case of 500 TeV monoenergetic and power law distribution with power index 1.5 primary gamma photon sources.

shown in Fig. 4.6(a) and, especially, (b) shows that the fluxes from both the $E_0 = 100$ and the 500 TeV cases are more concentrated at the center of the halo, because their first generation cascade has already developed at the center. Therefore, the pair halo from both these cases is more compact than in the $E_0 = 10$ TeV case.

However, it is not always the case that a higher E_0-value will give a more compact pair halo. For example, Figs. 4.6(e)and (f) show that the pair halo from the $E_0 = 100$ TeV case is more compact than in the $E_0 = 500$ TeV case.

Note that the cumulative angular distribution of the $E_0 = 10$ TeV pair halo gamma photon for the energy cuts 10 and 100 GeV in Fig. 4.6(d) and (e) are exactly the same shape. Since this case is the most simple for formulating the angular distribution, the angular distribution can be described analytically as shown in appendix C.

4.1.2 Formation of the Standard $E_\varepsilon{}^{-1.5}$ Photon Spectrum at Low Energy

As seen in Fig. 4.1(a) at photon energy significantly less than E^* (typically $< 0.1E^*$) where E^* is the energy at which spectral energy distributions achieves its maximum, the photon spectra have standard power-law distribution with photon index 1.5. This behavior can be understood easily from the following simple analytical approach.

The spectral characteristics of electrons and gamma-rays formed during the cascade in the the photon gas with a narrow distribution with a characteristic energy E_ω ($E_\omega \approx 3kT$ in the case of Planckian distribution with temperature T) can be qualitatively derived in the energy regime $E_e, E_\varepsilon \ll m_e^2c^4/E_\omega$. Note that

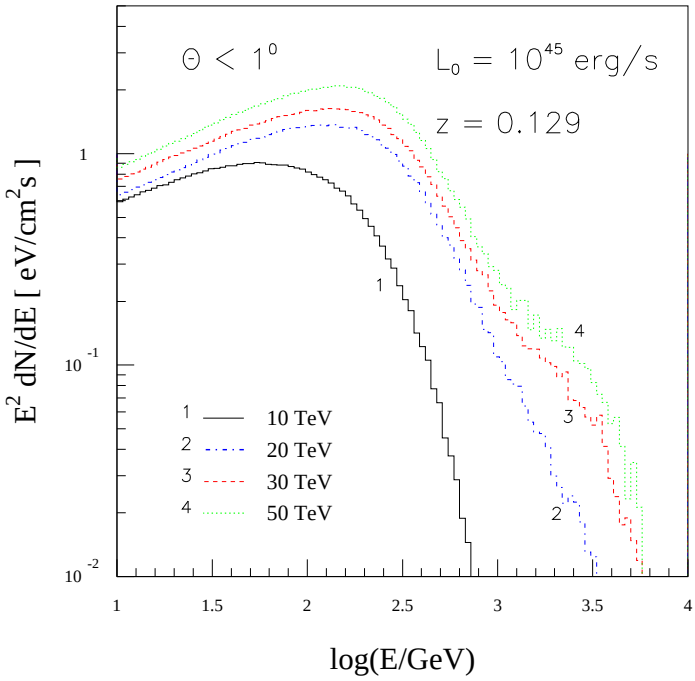

Figure 4.5: The pair halo SED for monoenergetic sources with different E_0.

the energy $m_e^2c^4/E_\omega$ characterizes the energy threshold of the pair production in the case of photon-photon interactions, and the transition region from the Thomson to Klein-Nishina regime in the case of Compton scattering.

Because of the pair-production kinematics, the secondary electrons are produced with energies in the limits

$$\frac{E_\varepsilon}{2}\left(1-\sqrt{1-\frac{m_e^2c^4}{E_\varepsilon E_\omega}}\right) \leq E_e \leq \frac{E_\varepsilon}{2}\left(1+\sqrt{1-\frac{m_e^2c^4}{E_\varepsilon E_\omega}}\right),. \qquad (4.1)$$

From here one finds that the minimum $e^\pm$ energy of the pair-produced electron is

$$E_e \geq \frac{m_e^2c^4}{4E_\omega} \text{ for } E_\varepsilon E_\omega \gg m_e^2c^4. \qquad (4.2)$$

Thus, in the low-energy photon field ($E_\omega \ll m_ec^2$) all electrons are produced with energy significantly exceeding m_ec^2. In fact, this is true also for broad-band target photon distributions, provided that the highest energy target photon which still contribute in pair production is much smaller than m_ec^2. Qualitatively this energy can be defined as $E_{\omega 1} \sim m_e^2c^4/E_\varepsilon$ where E_ε is determined from the condition of PP optical depth $\tau_{PP}(E_\varepsilon) \leq 1$.

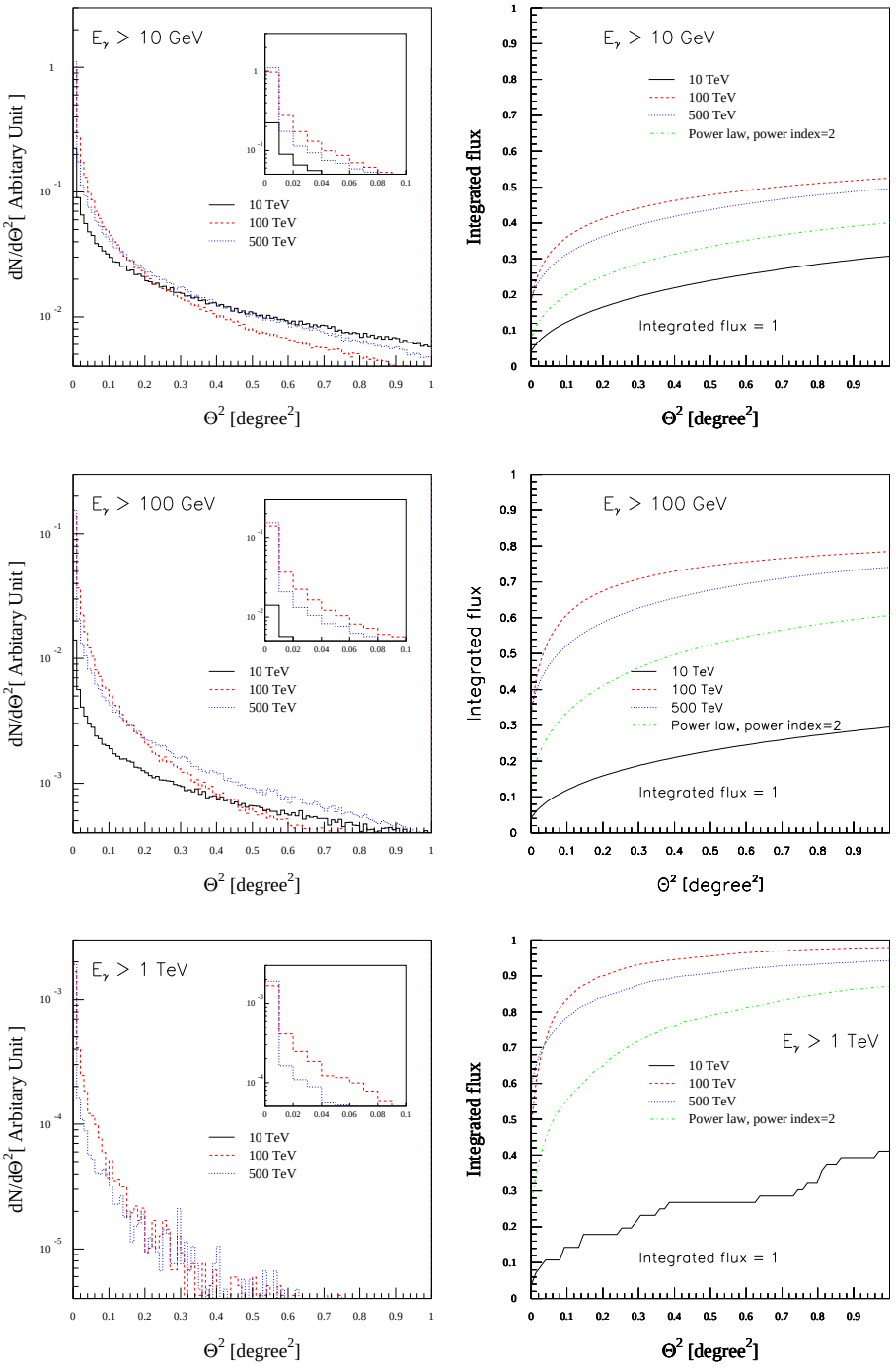

Figure 4.6: Pair halo differential and cumulative gamma angular distributions for different energy cuts, corresponding to different primary gamma photon energies. In the cumulative angular distribution there is a power law primary gamma photon distribution case for comparing. (a), (b) and (c) are the differential angular distributions for energy cuts 10, 100 GeV and 1 TeV, respectively, whereas (d), (e) and (f) are the cumulative angular distributions for energy cut 10, 100 GeV and 1 TeV, respectively.

In the case of a broad-band, e.g. power-law distribution of primary gamma-rays with photon index Γ, the spectrum of electrons have the following characteristic form: starting from the minimum (allowed by kinematics) energy at $E_{e\min} = m_e^2c^4/E_\omega$ the electron spectrum sharply rises, reaching the maximum at ${E_e}^\ddagger \approx 2.4E_{e\min}$, and then at $E_e \gg {E_e}^\ddagger$ it decreases $\propto {E_e}^{-(\Gamma+1)} \ln E_e$. Within accuracy better than 20 % the production spectrum of secondary pairs $Q_e(E_e)$ can be approximated in a simple analytical form [AA91]:

$$Q_e(E_e)\mathrm{d}E_e \propto \frac{\exp[-1/(x-1)]}{E_e \min x(1+0.07x^\Gamma/\ln x)}\mathrm{d}E_e, \tag{4.3}$$

where $x = E_e/E_{e\min}$. For more complex spectra of primary gamma-rays the production spectrum deviates from this simple function, but in any case, independent of the spectrum of primary photons, the production spectrum of electrons has a sharp low-energy cutoff at $m_e^2c^4/E_\omega$.

The cascade electron distribution is determined, in the absence of external electron sources, by the spectrum of pair produced electrons and by energy losses. In the approximation of gradual energy losses, $\Delta E_e/E_e \ll 1$ (typically, ≤ 0.3), the evolution of electrons is described by the continuity equation:

$$\frac{\partial N_e}{\partial t} + \frac{\partial(\dot{E}_e N_e)}{\partial E_e} = Q(E_e), \tag{4.4}$$

where $\dot{E}_e$ is the energy loss rate of electrons. In the radiation dominated medium it is dominated by Compton losses. The steady-state solution reads

$$N_e(E_e) \propto \dot{E}_e \int_{E_e}^{\infty} Q(E_e)\mathrm{d}E_e. \tag{4.5}$$

At ${E_e}^\dagger \leq m_e^2c^4/E_\omega$, $Q(E_e) = 0$. In this energy region the integral in the above equation is constant, and consequently $N_e(E_e) \propto \dot{E}_e \propto {E_e}^{-2}$. Here we take into account that at $E_e \leq m_e^2c^4/E_\omega$, the electron losses proceed in the Thomson regime.

It is known (see e.g. [BG70]) that if $N_e(E_e)$ is a power law, $\propto {E_e}^{-\alpha}$, the spectrum of inverse Compton photons produced in Thomson regime is $N_{E_\varepsilon}(E_\varepsilon) \propto {E_\varepsilon}^{-(\alpha+1)/2}$. Thus, the pair produced electrons with energy spectrum ${E_e}^{-2}$ ($E_e \leq 1/4E_\omega$) will lead to production of inverse Compton gamma-rays in the energy range $E_\varepsilon \leq 4/3E_\omega\gamma_{e\min}^2 \sim 0.1E_\omega$ with spectrum $\propto {E_\varepsilon}^{-3/2}$. Since these gamma-rays do not interact with the ambient photons, and suffer losses only due to (energy-independent) escape losses, their equilibrium spectrum coincides with the production spectrum.

At higher energies, $E_\varepsilon \geq 0.1E_\omega$, the Klein-Nishina effect becomes important both for the formation of the electron spectrum and production of gamma-rays. In addition gamma-rays start to interact with the ambient photons. Therefore the spectra of both electrons and gamma-rays significantly deviate from the above simple analytical expressions.

4.1.3 Power Law Distribution Sources

The Monte Carlo simulation for the pair halo model arguably becomes more realistic when the primary gamma photons are distributed as a power law. The scenario becomes more complicated, however, since in this case the first generation cascade starts with many different gamma photon energies. The characteristic parameters in this distribution are the power index α, the lower energy limit E_1, and the upper energy limit E_2. Because the lower energy limit should have only a limited effect on the SED and angular distributions, the parameters that are varied for this study are only the power index α and the upper energy limit, E_2.

Different Power Indices

Source luminosity	$L_0 = 10^{45}$ erg/s
Primary gamma photon spectrum	Power law $(dN/dE)_{source} \propto E^{\alpha}$ $E_1 \leq E \leq E_2$ $E_1 = 1$ TeV $E_2 = 100$ TeV $\alpha = 1.5$ (dotted line) $\alpha = 2.0$ (solid line) $\alpha = 2.5$ (dashed line)
CIB model	Primack et al.,2000
Redshift	0.129

Table 4.3: Summary of the quantities and parameters used in the simulation, for halo sources with different power indices.

The parameters used in the calculations are given in Table 4.3. The pair halo SEDs for different power law indices are presented in Fig. 4.7. The figures show that the primary gamma photons with $\alpha = 1.5$ produce the highest pair halo flux, while $\alpha = 2$ and 2.5 give lower fluxes. Because the number of absorbed gamma photons for the lower power index is higher than in the higher power index, as seen from Table 4.4, the luminosity of the absorbed flux from the higher power index is always higher.

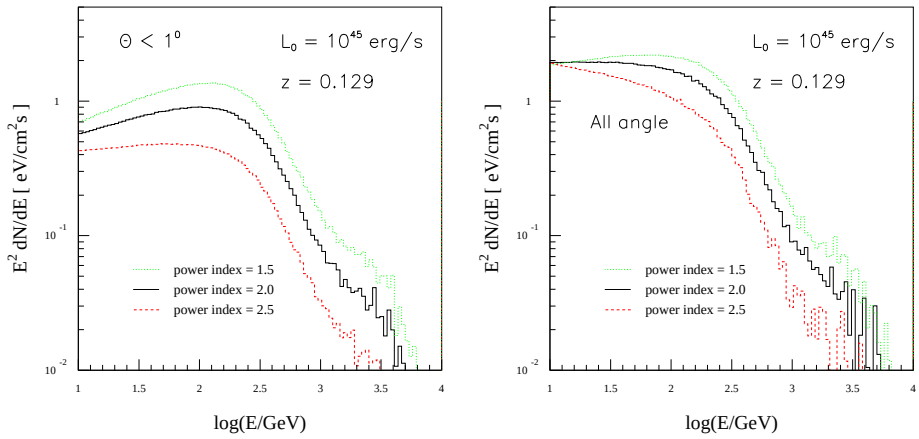

Figure 4.7: Spectral energy distribution of the pair halo from a power law primary energy distribution with power index 1.5, 2 and 2.5 as identified in the figure. Left panel:(a) The SED at open angle 1°. Right panel:(b) The SED at all angles.

α	$L_{halo}(E > 10$ GeV)	L_{abs}
1.5	26.1%	0.4%
2.0	22.8%	1.1%
2.5	16.1%	1.9%

Table 4.4: The luminosity of the pair halo and the absorbed flux compared with the source luminosity, L_0, for power law distributions with different E_2.

For the cases $\alpha = 1.5$ and 2, Fig. 4.7(a) shows that the peak energy $E^* \approx$ 150 GeV. In all three cases shown in the figure, a flattening is evident in the SED at HER, and the spectral shapes are similar for all power-law injection indices α.

The power index, α_1, of the pair halo gamma photon in the low energy region (LER) depends on α. The larger the value of α, the larger is α_1, as seen in Figs. 4.7(a) and (b). A summary of α_1-values for each case is presented in Table 4.5. Note that in the monoenergetic case for $E_0 \geq 100$ TeV, α_1 is nearly equal to the case of a power law distribution with $\alpha = 1.5$.

The angular distribution for power-law-distributed primary VHE gamma photons is presented in Fig. 4.8. As seen from the figure, the pair halo photon fluxes are concentrated at the center, but their fluxes at the center are lower than in the case of monoenergetic primary VHE photons. Figures 4.8(d), (e) and (f) show that the angular distributions in the power law cases are less concentrated at the center than in the monoenergetic case. For the power law injection, the harder the power index the more concentrated towards the center is the flux. However, Figs. 4.8(d), (e) and (f) show the same features as in the

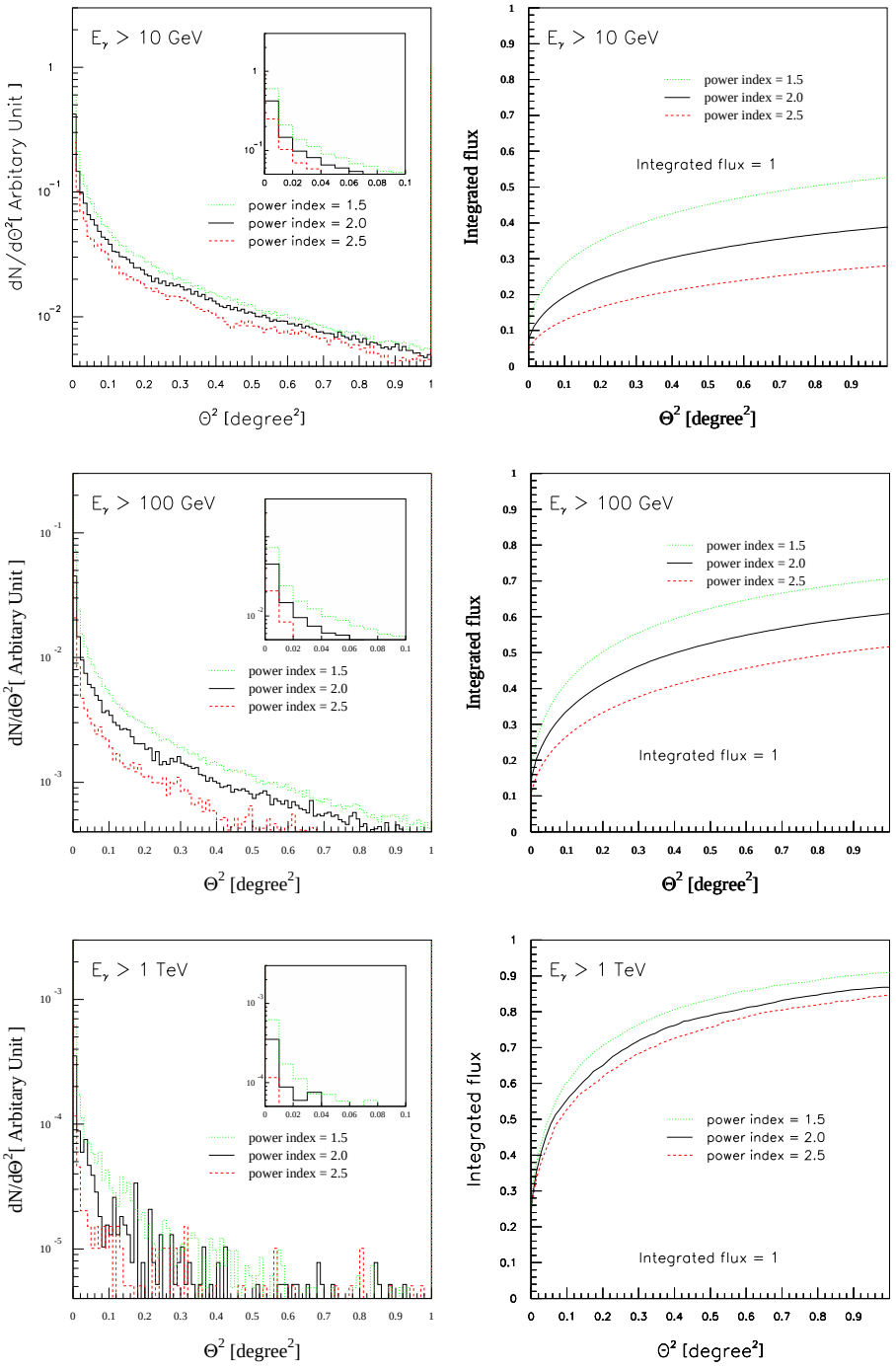

Figure 4.8: Left panels: The pair halo gamma photon differential angular distribution. In the text, the plots are referred to as (a), (b) and (c), from top to bottom. Right panels: The cumulative angular distribution of the gamma photons with energy more than 10 GeV and 100 GeV. The plots are referred to as (d), (e) and (f).

α	α_1	
	$\theta < 1^\circ$	all angle
1.5	1.67	1.89
2.0	1.80	1.95
2.5	1.92	2.20

Table 4.5: The power law index for the LER , α_1, for different power law primary VHE photon distributions. Both for the cases $\theta < 1^\circ$ and all angle.

monoenergetic case, indicating that for a high observed energy the halo is more concentrated towards the center.

Different Upper energy limit

Source luminosity	$L_0 = 10^{45}$ erg/s
Primary gamma photon spectrum	Power law $(dN/dE)_{source} \propto E^{\alpha}$ $E_1 \leq E \leq E_2$ $\alpha = 2.0$ $E_1 = 1$ TeV $E_2 = 10$ TeV (solid line) $E_2 = 100$ TeV (dashed line) $E_2 = 500$ TeV (dotted line)
CIB model	Primack et al.,2000
Redshift	0.129

Table 4.6: Summary of the quantities and parameters used in the numerical code for studying pair halos for sources with different energy upper limits.

Another critical parameter in the power law VHE photon sources is the upper energy limit, E_2. In this study E_2 = 10, 100, and 500 TeV were used to monitor the effect of this parameter on the pair halo.

The SED in Fig. 4.9 and the angular distribution in Fig. 4.10 for E_2 = 100 and 500 TeV show that the effect of the upper energy limit on the pair halo is

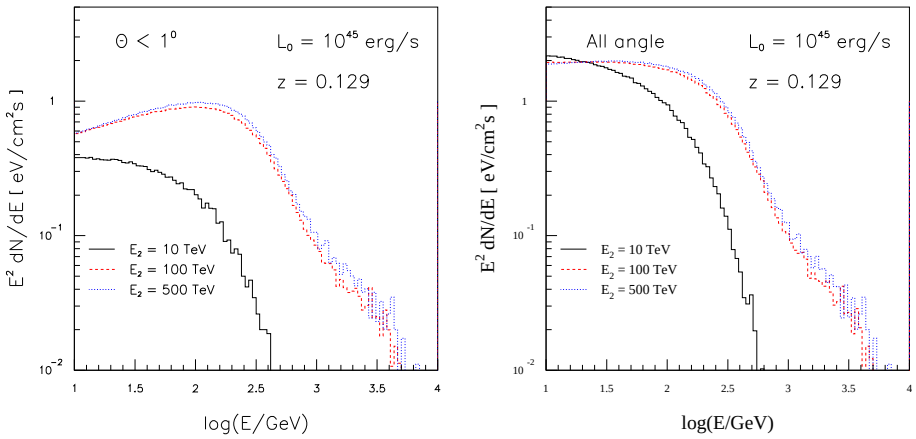

Figure 4.9: SED of the pair halo gamma photons within 1° (left panel) and for all angles (right panel), from power law distributed primary gamma photons with the same power index α but with different energy upper limits E_2.

E_2	$L_{halo}(E > 10$ GeV)	L_{abs}
10 TeV	15.9%	1.9%
100 TeV	22.3%	1.1%
500 TeV	24.1%	0.7%

Table 4.7: The luminosity of the pair halo and the absorbed flux compared with the source luminosity, L_0, for power law distributions with different E_2.

very small. This is especially the case with respect to the angular distributions, which are almost exactly the same in both cases. A substantial difference arises only in the first bin of the histogram, where it is clear that the higher the value of E_2, the more interaction and therefore the higher is the flux at the center. The values in Table 4.7 also show that the pair halo luminosity and the luminosity from the absorbed flux in the 100 and 500 TeV cases are only slightly different, but both differ significantly from the 10 TeV case.

As for the monoenergetic case, the SED and angular distributions for the power-law case with $E_2 = 10$ TeV and 100 TeV are quite different, but those for the 100 and 500 TeV cases are quite similar. This fact implies that the pair halo properties depends sensitively on E_2 when this quantity is below 100 TeV.

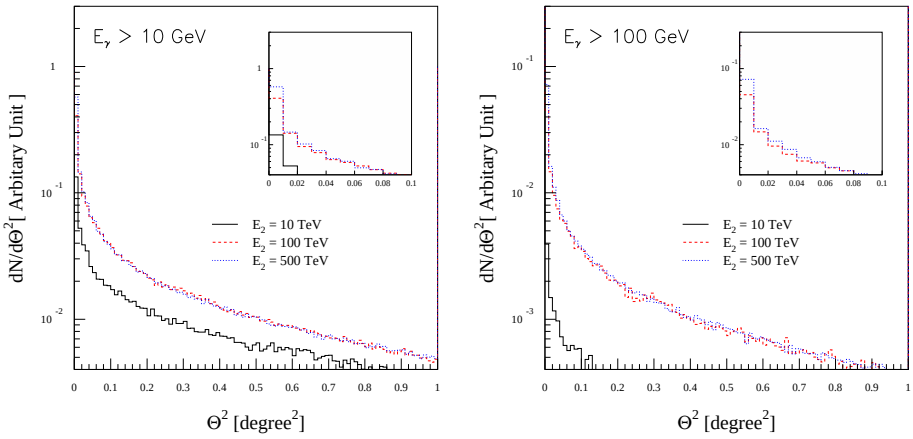

Figure 4.10: Differential angular distribution of the pair halo gamma photons with energy above 10 GeV (left panel) and 100 GeV (right panel) from power-law distributed primary gamma photons with the same power index α but different energy upper limits E_2.

4.2 Pair Halos from Different Redshifts

Source luminosity	$L_0 = 10^{45}$ erg/s
Primary gamma photon spectrum	Monoenergetic $(dN/dE)_{source} \propto \delta(E - E_0)$ $E_0 = 100$ TeV
CIB model	Primack et al.,2000
Redshift	(1) $z = 0.034$ (≈ 160 Mpc) (2) $z = 0.129$ (≈ 633 Mpc) (3) $z = 1$ ($\approx 7 \times 10^3$ Mpc) (4) $z = 2$ ($\approx 1.8 \times 10^4$ Mpc)

Table 4.8: Summary of the quantities and parameters used in the program for monoenergetic pair halo sources located at different redshifts.

A summary of the parameters used in the calculation is given in Table 4.8. In the part of the table giving the redshift values, the corresponding luminosity distance of the source, d_s, is given within parentheses.

Since the CBR evolves together with the universe, the CBR at different redshifts has different profiles, as shown in Fig. 4.11. The background photon field in this figure is the photon field shown in the proper frame; i.e., the comoving frame, where the factor $(1+z)^3$ accounts for the expansion of the universe. At high redshifts, not only is the distance from source to observer higher such that a cascade can develop more generations than at lower redshifts, but also the photon number and energy density in the background photon field are higher. The CMB can be expressed in the analytic form given by Eq.(1.7), and is characterized by the radiation temperature T. The temperature depends on the redshift through the factor $(1+z)$. This can be easily seen from Fig. 4.11 in the so-called Rayleigh-Jeans region.

The higher photon density of the CMB at large redshifts, represented by the factor $(1+z)^3$, leads to a shorter mean free path length, as seen from Fig. 4.12. The IC mean free path length in the Thomson regime, for example, which is constant at energies lower than 10 TeV, is shorter by a factor of about $(1+z)^3$ since the total cross section is constant in this regime. On the other hand, in the Klein-Nishina regime, where the total cross section depends on the photon energy as ω^{-1}, the mean free path length is shorter by a factor $(1+z)^2$

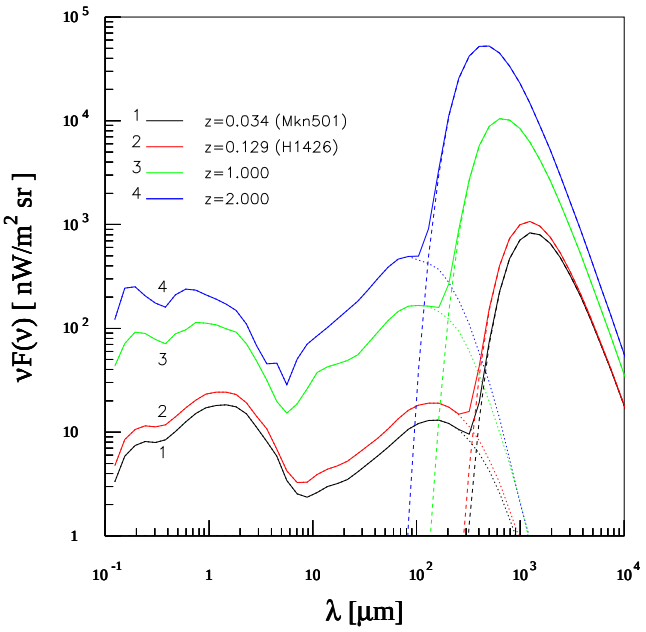

Figure 4.11: Background photon field at different redshifts in the proper frame.

The number of cascade generations increases at high redshifts, both because the source distance increases, and because the PP mean free path length becomes shorter at high redshifts. Therefore, the absorption of the primary gamma photon from the sources at high redshift is more effective.

For this case, the attenuation factors are also presented in Fig. 4.13, since the high redshift simulation needs this factor in order to calculate the observed pair halo energy distributions.

In the high redshift cases, for example $z = 1$ and 2, a cascade develops through the evolution of the CBR. The CBR photon field differs significantly between low and high redshifts, and therefore the assumption of constant CBR along the development of the cascade is not acceptable. For this situation the simulation is slightly different, and the second scheme explained in Sec. 3.5 is applied. The spectrum of the halo for different redshifts can not be presented in SED form like the previous results, because the distances d_ss are different. Another way to represent the pair halo energy distribution is given by the so-called spectral luminosity distribution (SLD), $\mathrm{E\,L}_\nu$, where

$$\mathrm{E\,L}_\nu = 4\pi d_s^2 \nu \mathrm{F}_\nu, \tag{4.6}$$

$$= 4\pi d_s^2 E^2 \left(\frac{dN}{dE} \right). \tag{4.7}$$

The integral over ν of this quantity gives the source luminosity. To obtain the

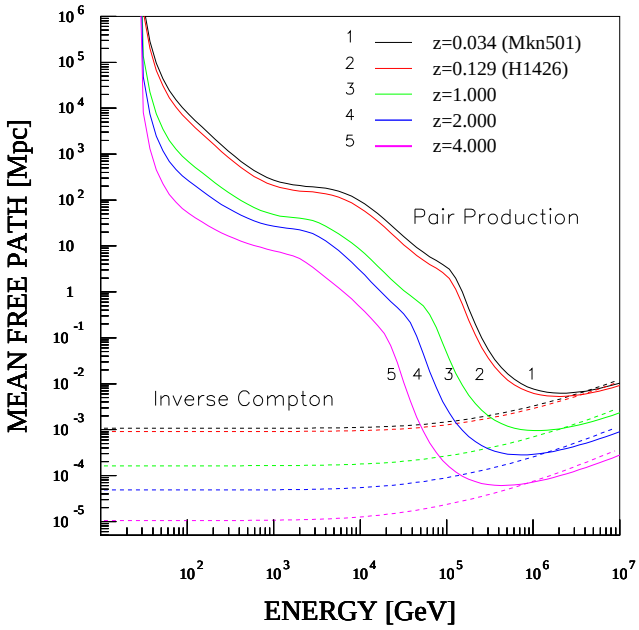

Figure 4.12: The mean free path of both PP and IC for different redshifts, using the background photon field in Fig. 4.11.

energy flux, the result should be divided by $4\pi d_s^2$.

For pair halos located at different redshifts, as presented in Fig. 4.14, the SLDs cannot be shown for all angles, since the scheme used for high redshift sources is only valid over a limited opening angle.

The SLDs obtained for different redshifts show the development of the pair halo with redshift. At $z = 0.034$, most of the pair halo energy, E_{halo}, is in the form of pair halo gamma photons in the HER (above $E^* = 250$ GeV). The flattening in the region around 3-10 TeV corresponding to the CIB at 3-10 μm can still be seen, but is less obvious. At low energies the distribution is a power law with index about 1.5. These features can be seen for an opening angle of 1° as well as 0.1°.

The pair halo SLD for a redshift value of $z = 0.129$ shows that E^* shifts to around 200 GeV, and the pair halo gamma photons in the HER are significantly absorbed. The flattening is pronounced. The luminosity of the gamma photons in the LER is higher than in the case $z = 0.034$ by a factor of two at 10 GeV. The corresponding factor is around four if one considers a small opening angle, as seen by comparing Figs. 4.14(a) and (b).

Even though the luminosity in the LER is higher, the distance has a stronger effect on the observed flux; contributing a factor of 16 for $z = 0.034$ over $z = 0.129$. Therefore the observed pair halo flux from $z = 0.129$ is lower than $z = 0.034$.

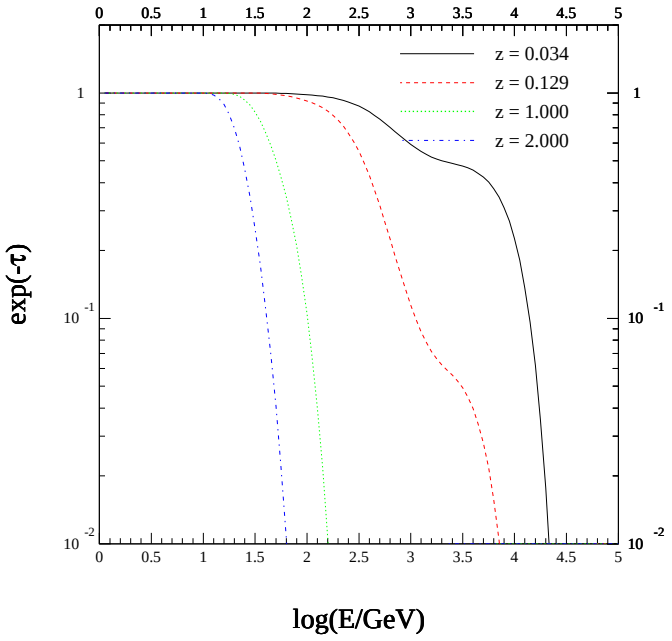

Figure 4.13: The attenuation factor $\exp(-\tau)$ for gamma photons as a function of their energy for CBR at different redshifts, as presented in Fig. 4.11.

From the pair halo SLDs from very high redshift sources, $z = 1$ and 2, the E^* moves to 30 and 10 GeV, respectively.

The pair halo gamma photon angular distributions from different redshifts are presented in Fig. 4.15. In the second scheme, used for the high redshift simulations, the simulation considers a cascade only in the region corresponding to a 5° observing open angle. The cumulative angular distributions in Figs. 4.15(d), (e), and (f) are thus normalized with respect to the fluxes within 5° only.

The angular distribution for a $z = 0.034$ source shows that the angular size of the pair halo is quite large for a gamma photon energy of more than 1 TeV. In fact, the angular distribution for all three energy cuts is more or less the same, as it is evident for the fitting parameter given in Table 4.9. It can be explained by the fact that at this redshift, the considered angular size of 1° corresponds to a distance about 3 Mpc from the source, which is the same as the PP mean free path of $E = 100$ TeV gamma photons. Therefore, most of the observed gamma photons within 1° are generated by the first generation cascaded $e^{\pm}$s.

The angular distribution for $z = 0.129$, 1 and 2 behave similarly. They are more centrally concentrated when observing in higher energy cuts. The angular distribution are more centrally concentrated for higher redshifts.

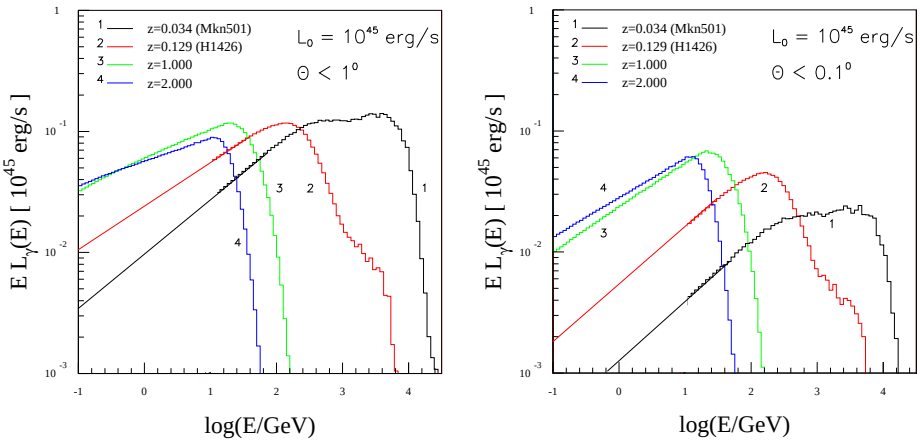

Figure 4.14: Pair halo spectral luminosity distributions at different redshift for opening angle 1° and 0.1°, referred to as (a) and (b), respectively. In the figures, sources at redshift $z = 0.034$ and $z = 0.129$ are calculated down to only 10 GeV and below this energy an extrapolation was applied.

	a_1 $(\times 10^{-11})$	a_2 $(\times 10^{-8})$	a_3 $(\times 10^{-5})$	a_4 $(\times 10^{-3})$
$E_\gamma > 10$ GeV	0.298	0.104	0.650	-0.261
$E_\gamma > 100$ GeV	0.317	0.142	0.653	-0.288
$E_\gamma > 1$ TeV	0.351	0.144	0.661	-0.311

Table 4.9: The fitting parameters of the $z = 0.034$ pair halo differential angular distribution normalized within 1°.

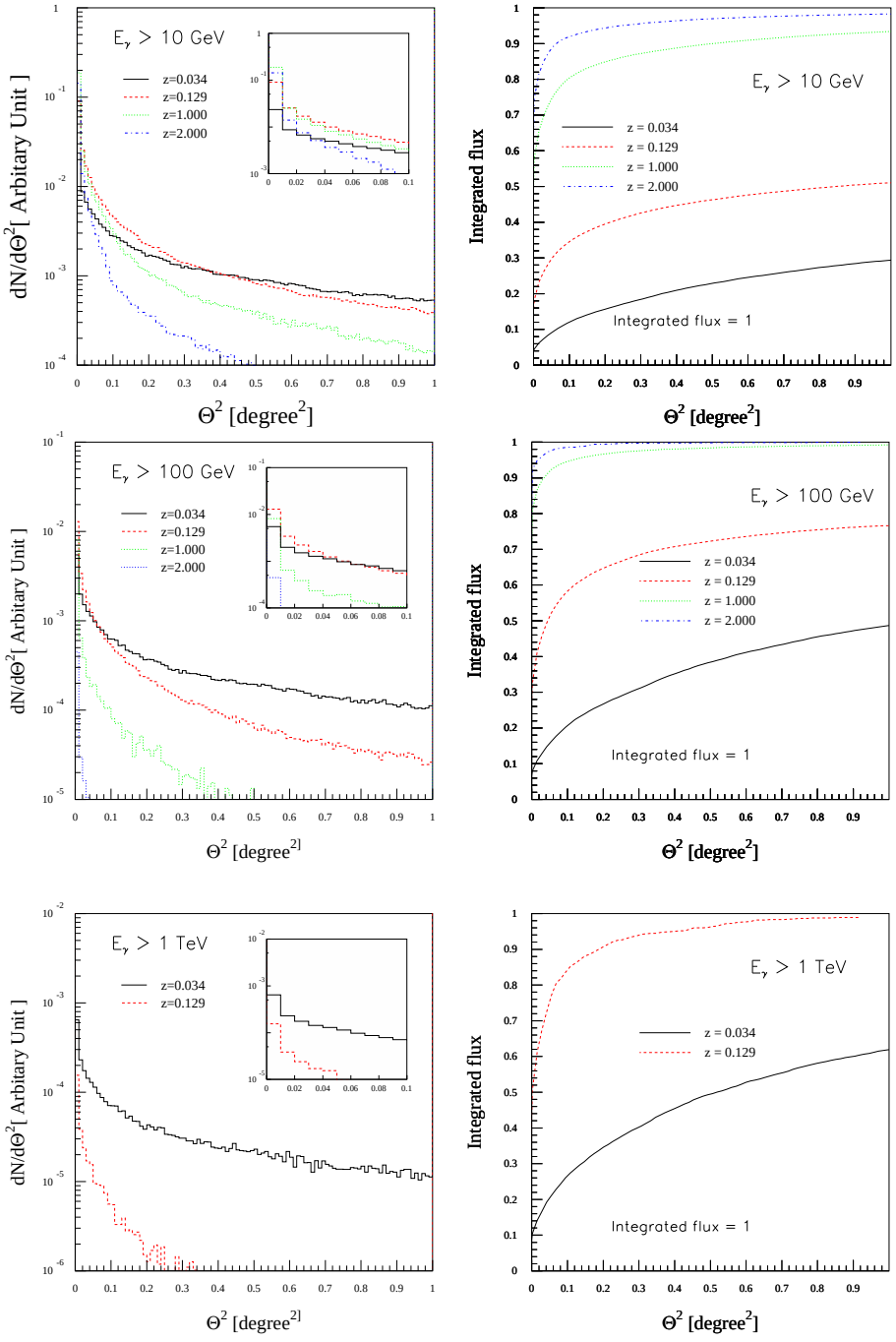

Figure 4.15: Angular distributions for different redshift sources. Left panels: Pair halo gamma photon differential angular distributions. In the text, the plots are referred to as (a), (b) and (c) from top to bottom. Right panels: The cumulative angular distribution of the gamma photon with energy above 10 GeV, 100 GeV, and 1 TeV which are referred to as (d), (e) and (f).

4.3 Pair Halos from Different CIB Intensity

Source luminosity	$L_0 = 10^{45}$ erg/s
Primary gamma photon spectrum	Monoenergetic $(dN/dE)_{source} \propto \delta(E - E_0)$ $E_0 = 100$ TeV
CIB model	Primack et al., 2000 (solid line) 3× Primack et al., 2000 (dashed line) 10× Primack et al., 2000 (dot-dashed line)
Redshift	0.129

Table 4.10: Summary of the quantities and parameters used in the program using the same CIB model but different intensity.

In this section, the effect on the pair halo from the same CIB model but at different intensities is discussed. The used CIB is scaled by a factor three and ten as shown in Fig. 4.16. Figure 4.17 shows the accordingly different PP mean free path length of the gamma photon. The mean free path length for different CIB is reduced proportionally to the increase in the level of the CIB.

The pair halo SEDs for different CIB presented in Fig. 4.18 shows that the gamma photons in the HER are absorbed and the lower energy gamma photons in the LER are produced via the cascade. In the three and ten times CIB cases, there are no TeV gamma photons left and, therefore, there is no flattening in the HER visible. The E^* move from about 150 GeV to be 60 and 30 GeV for the case of three times and ten times respectively.

Both pair halo differential and cumulative angular distributions are presented in Fig. 4.19. The angular distributions are shown only above energies of 10 and 100 GeV since at 1 TeV the gamma photons are already absorbed. At energy 10 GeV, the photon fluxes in the pair halo differential angular distributions for factor of three and ten are higher whereas at energy 100 GeV both are lower. The flux difference compared with the other cases are higher when observing at higher energies as can be seen from Fig. 4.19(a) and (b). It seems to be that the differential angular distribution at low energy is less sensitive to the CIB intensity since the CIB differs by a factor of ten but the corresponding differential angular distributions differ only by a factor of two. However, the cumulative angular distribution at 10 GeV is quite sensitive to the CIB inten-

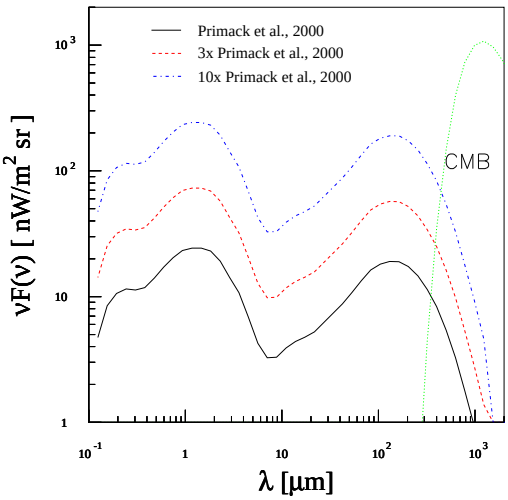

Figure 4.16: The spectral energy distribution of the CIBs which are the same function but different in intensities.

sity as shown in Fig. 4.19(c) and (d). The pair halos are more concentrated at the center when the CIB is at a higher level. The Table 4.11 present $\Theta_{90\%}$ for different observed energies and CIB intensities to demonstrate the size of the pair halo. The angular size of the halo varies linearly with the intensity of the CIB.

CIB	$\Theta_{90\%}$	
	$E > 10$ GeV	$E > 100$ GeV
Primack	13.8°	4.6°
3× Primack	4.0°	1.7°
10× Primack	1.2°	0.73°

Table 4.11: Table shows $\Theta_{90\%}$ for different observed energy and CIB intensity.

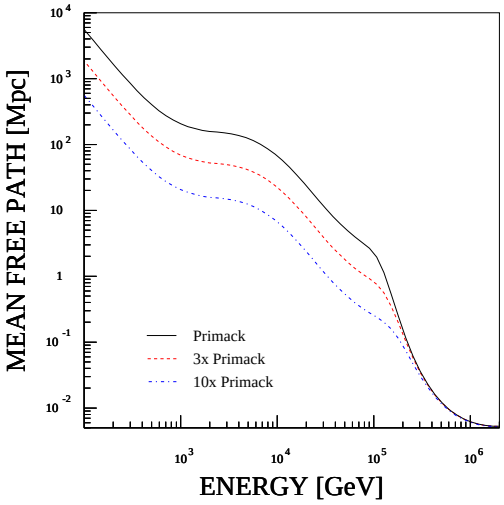

Figure 4.17: The PP mean free path length of the gamma photon for different CIB intensity.

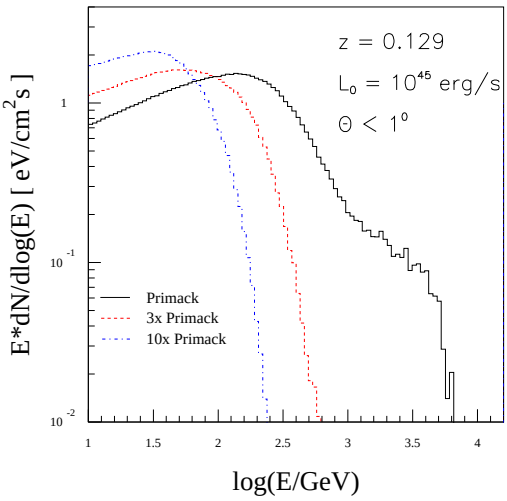

Figure 4.18: The pair halo spectral energy distributions for different CIB intensity.

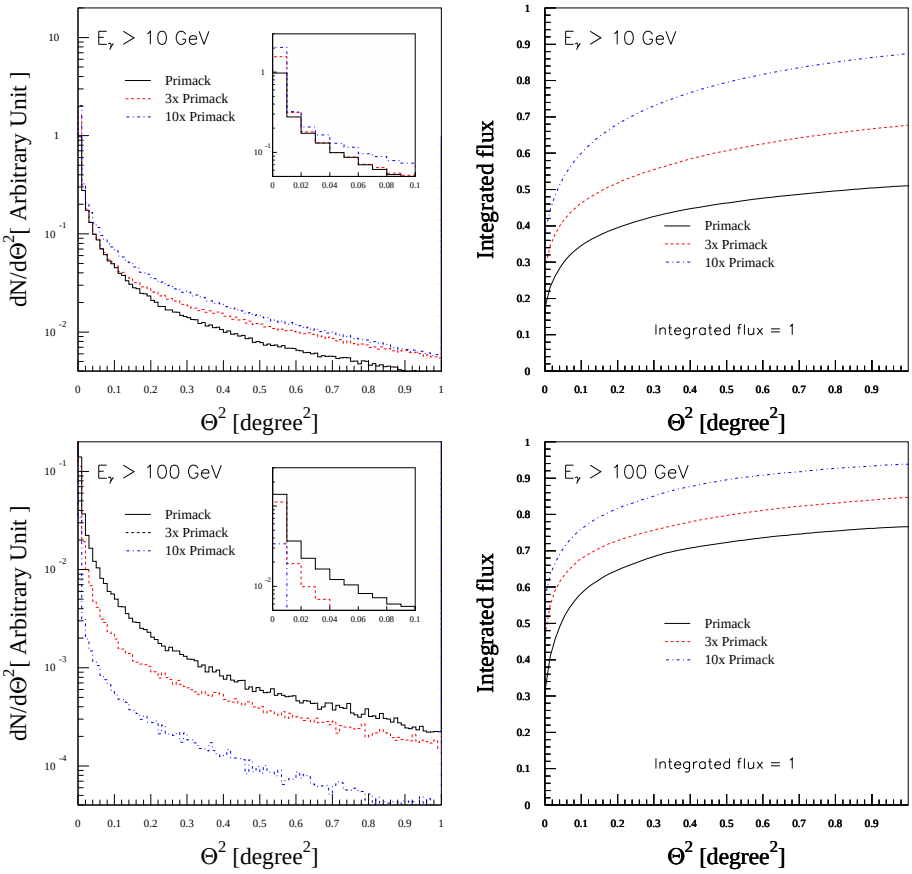

Figure 4.19: Angular distributions for different CIB intensity from monoenergetic source with $E_0 = 100$ TeV at redshift $z = 0.129$. Left panel: Pair halo gamma photon differential angular distributions for different energy. In the text, the plots are referred to as (a) and (b) from top to bottom. Right panel: Pair halo gamma photon cumulative angular distribution for different energy. In the text, the plots are referred to as (c) and (d) from top to bottom.

4.4 Different CIB Models

4.4.1 Low Redshift Sources

Source luminosity	$L_0 = 10^{45}$ erg/s
Primary gamma photon spectrum	Monoenergetic $(dN/dE)_{source} \propto \delta(E - E_0)$ $E_0 = 100$ TeV
CIB model	Primack et al., 2000 (solid line) Malkan & Stecker, 2001 (dashed line) Kneiske et al., 2002 (dot-dashed line)
Redshift	0.129

Table 4.12: Summary of the quantities and parameters used in the program for pair halo sources at low redshift, using different CIB models.

The effect on the pair halo from different CIB models is discussed in this section.

The CIB models used in this calculation are presented in Table 4.12. There are two additional CIB models considered. The CIB from Kneiske (2002) [KMH02], hereafter K02, is calculated by convolution of the radiation from the formation of stars with a specific cosmic star formation rate. The other is a model from Malkan & Stecker (2001) [MS01], hereafter M01. This model uses the assumption that the systematic dependence of galaxy spectra with luminosity which is observed today also applies at earlier cosmic times. Therefore, this model starts with the present day infrared luminosity function of galaxies, and assumed a pure luminosity evolution for each galaxy.

The pair halo SEDs for different CIB models shown in Fig. 4.21 are different in the HER which is quite sensitive to the CIB in the near-infrared range. The CIB model from K02, for example, has the same shape as P00 in near-infrared ($2 < \lambda < 5$ μm). For both models (P00, K02), a flattening of the pair halo SED in the HER is present, whereas this flattening disappears for the model of M01, since the SED in the near-infrared region has a different form. Therefore, observing the pair halo SED in the HER can constrain the CIB in the near-infrared range. The SED in the LER has no significant deviation, but the photons in this region are the main contributor to the pair halo angular

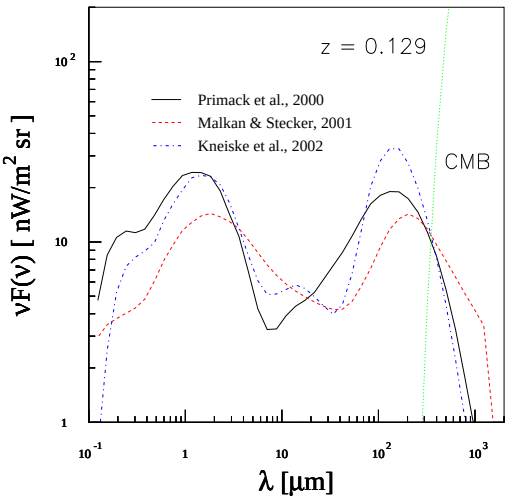

Figure 4.20: Spectral energy distributions of the CBR; close-up of the CIB range. Three CIB models are considered; Primack et al., 2001, Malkan & Stecker, 2001 and Kneiske et al., 2002.

distributions.

Before considering the effect of different CIB models on the pair halo angular distribution, it will be useful to consider the PP mean free paths, as illustrated in Fig. 4.22. The figure has been adjusted to cover the region $E < 100$ TeV, which is the primary VHE gamma energy, and to illustrate the difference of the mean free path length for each model. At $E = 100$ TeV, the gamma photons interact mostly with CIB photons in the far-infrared region. As seen from the Fig. 4.22, the lowest mean free path at 100 TeV is that corresponding to the K02 model. However, the differences between the P00 and M01 results on the mean free path are larger, and are substantial over a larger energy interval, than if one compares the results obtained from the K02 and P00 models. Accordingly, the angular distributions between the P00 and M01 model are more different, as shown in Fig. 4.23.

The pair halo differential angular distributions for the case of P00 and K02 are very similar, whereas in the case of M01, at higher observed energy the differential angular distribution shows larger deviation from the other models. On the other hand, the pair halo cumulative angular distributions for all CIB models are quite similar. The angular sizes of the pair halo for different CIB model are more or less the same as shown in Table 4.13.

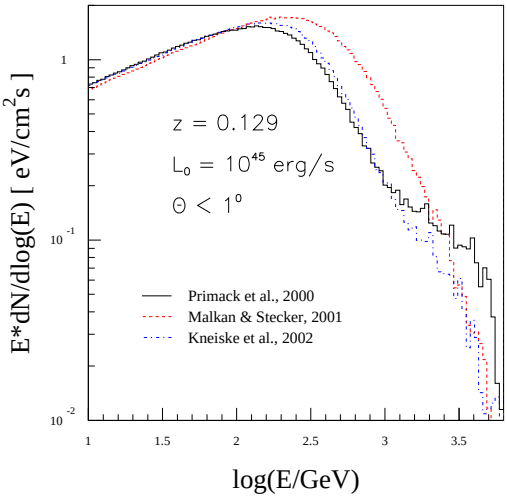

Figure 4.21: Pair halo SEDs for different CIB SEDs as shown in Fig. 4.20.

CIB model	$\Theta_{90\%}$		
	10 GeV	100 GeV	1 TeV
P00	13.8°	4.6°	0.43°
M01	14.6°	4.5°	0.63°
K02	13.7°	4.7°	0.38°

Table 4.13: Table shows $\Theta_{90\%}$ for different observed energy and different CIB model.

4.4.2 High Redshift Sources

In this section the pair halos at high redshift, i.e. $z = 2$, for different CIB models are considered. The models used here were introduced as P00 and K02, and are very different from each another, as shown in Fig. 4.24.

Figure 4.26 shows the pair halo SLDs for different CIB models. The spectral luminosity distribution in both HER and LER are different. The SLD from the P00 CIB model at the HER drops faster than the one from the K02 model, since the P00 CIB at the near-infrared region (which is responsible for the attenuation of the HER gammas) is about 5 times higher than the other model. Because of the very large distance the HER gamma photons are totally absorbed and cannot be used to study the CIB SED as well as the low redshift case. Not only the SLDs in the HER are different, but also that in the LER. Both attain a power law distribution, with power index 1.7 and 1.8 for K02 and P00, respectively.

The P00 CIB is higher than the K02 over the whole energy range, and therefore the corresponding PP mean free path length is different over the whole energy range up to 50 GeV, as shown in Fig. 4.27. This directly affects the

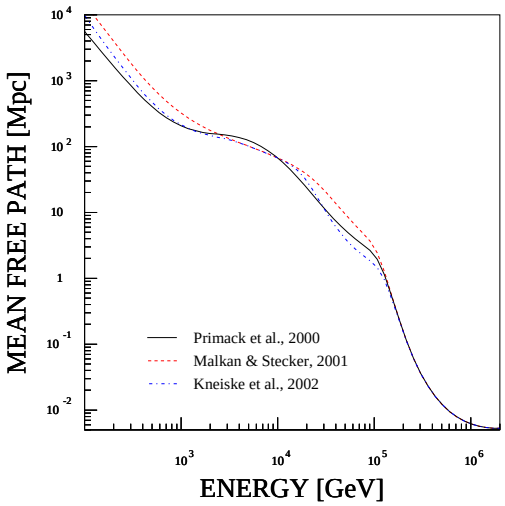

Figure 4.22: The PP mean free path lengths corresponding to specific CIB models in Fig. 4.20.

angular distribution. The pair halo angular distribution for K02 CIB is wider than that of P00 CIB, as shown in Fig 4.28. Since the CIB that the VHE gamma photons interacted with are in the same epoch as the source, this means the pair halo angular distribution is sensitive to the CIB at that epoch.

Source luminosity	$L_0 = 10^{45}$ erg/s
Primary gamma photon spectrum	Monoenergetic $(dN/dE)_{source} \propto \delta(E - E_0)$ $E_0 = 100$ TeV
CIB model	Primack et al., 2000 (solid line) Kneiske et al., 2002 (dot-dashed line)
Redshift	2

Table 4.14: Summary of the quantities and parameters used in this simulation for the case of a pair halo source with different CIB models at high redshift ($z = 2$).

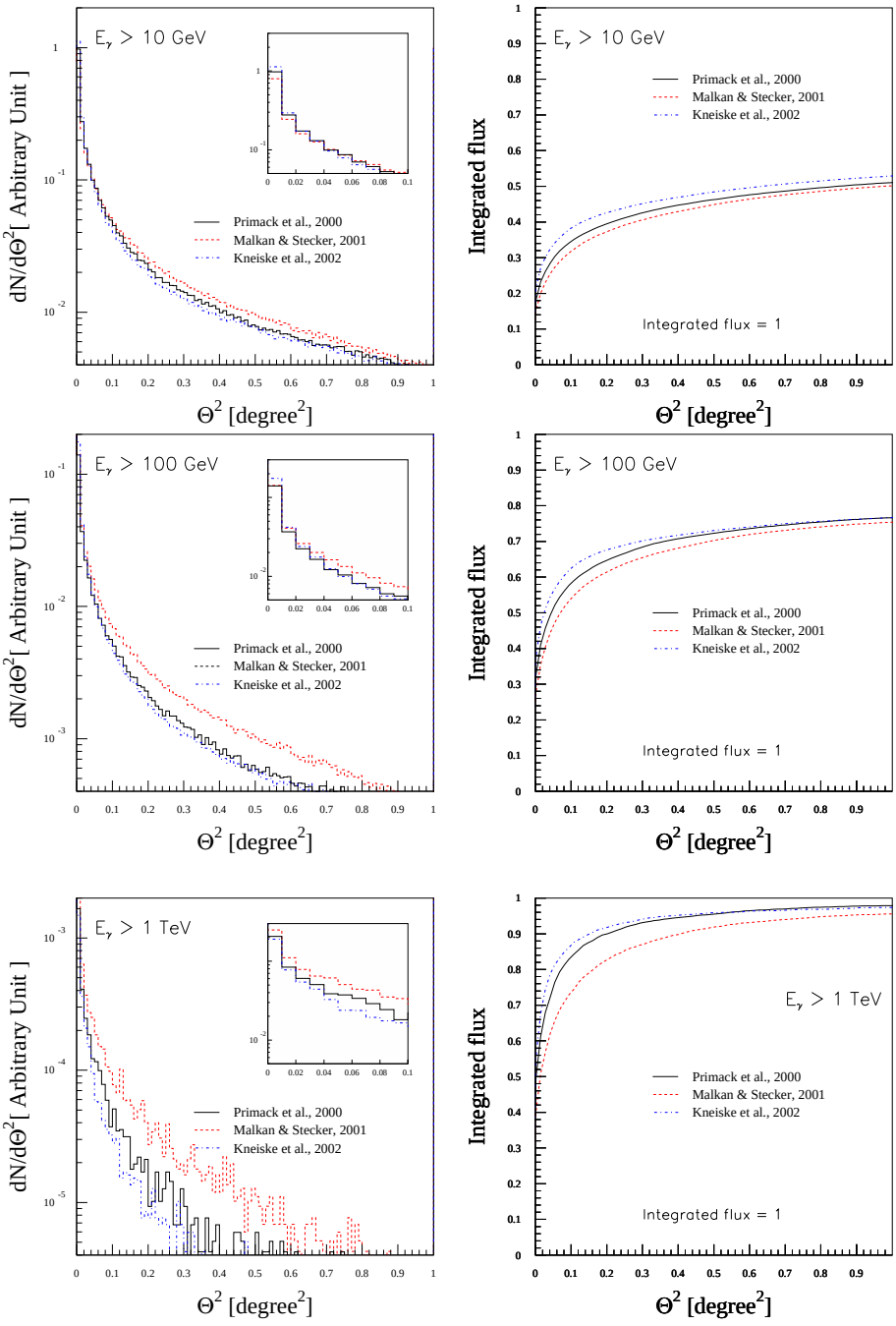

Figure 4.23: Angular distributions for the different CIB models. Left panel: Differential angular distributions referred to as (a), (b) and (c) from top to down. Right panel: Cumulative angular distributions are referred to as (e), (f) and (g) from top to down.

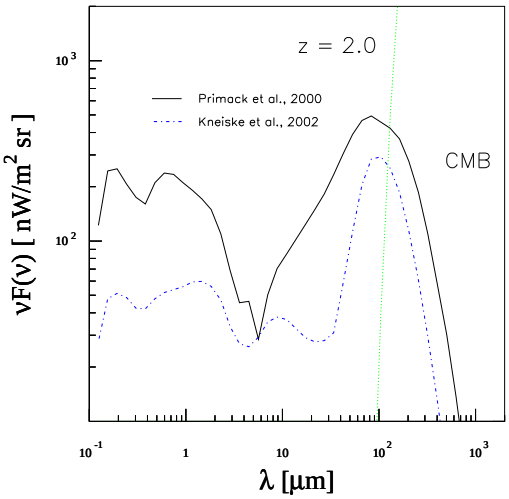

Figure 4.24: The two CIB models used in Sec. 4.4.2, taken from P00 and K02. The models are significantly different from each other because of differing underlying cosmological assumptions; i.e., the models use different star formation rates.

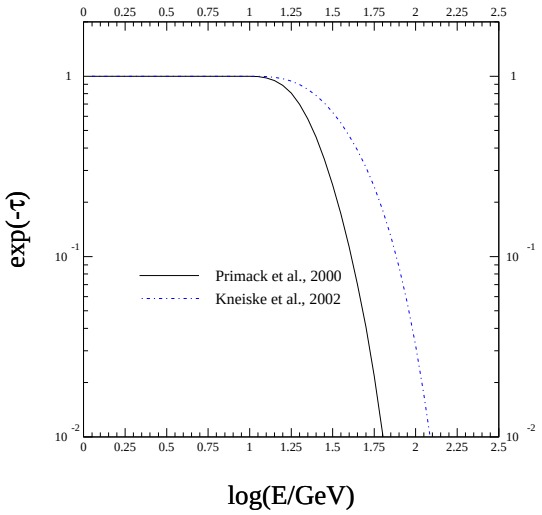

Figure 4.25: The attenuation factor $\exp(-\tau)$ for gamma photons as a function of their energy for the P00 and K02 CIB models.

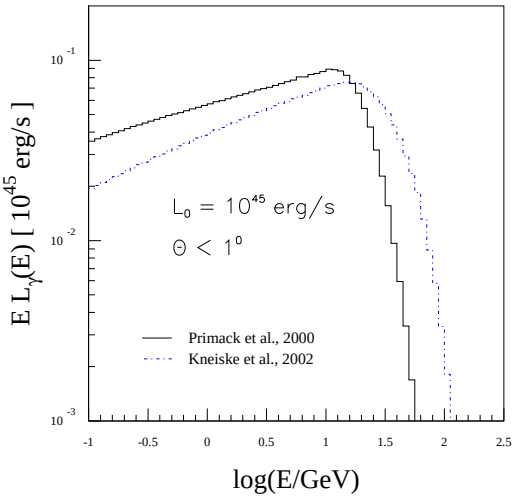

Figure 4.26: The pair halo spectral luminosity distributions for both CIB models.

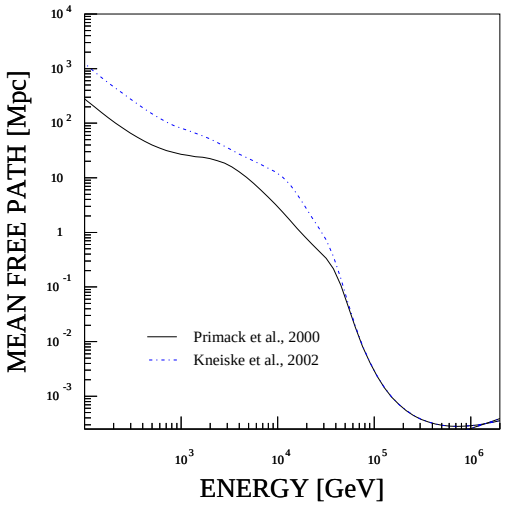

Figure 4.27: The PP mean free path length for the different CIB models up to 50 GeV. Since the P00 spectrum for the CIB is always above that of K02, the mean free path for P00 is always lower than the other for energies up to 50 GeV.

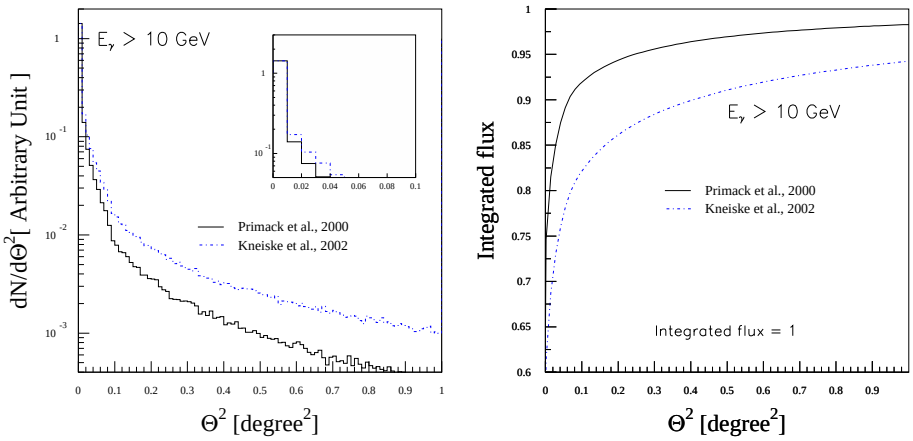

Figure 4.28: Pair halo angular distributions for the P00 and K02 CIB models. Left panel: The differential angular distribution. Right panel: The cumulative angular distribution. Note: Keep in mind that this cumulative angular distribution is normalized with flux within 5°.

Chapter 5

Conclusion and Discussion

In the previous section, different properties of the pair halos like angular distribution and spectral energy distribution have been studied. In particular, the effect of the characteristic high energy injection and the properties of the cosmic infrared background (CIB) on the pair halos have been investigated.

In **monoenergetic sources**, the choice of the primary gamma photon energy influences strongly both the energy and angular distribution. Whenever the energy of the injected photon is large enough to interact with the CMB for a given redshift, the cascade develops in the proximity of the source and converts quickly the injected monoenergetic photon distribution into a power-law distribution with photon index 1.5. The pair halos from such cases are independent of the primary gamma photon energy and behave like the pair halos that are generated from power law distributed primary gamma photons.

For lower energy injection, the mean free path length for interaction with the CIB is considerably larger than for interaction with the CMB. Here, a widening of the halo with decreasing energy E_0 is observed.

For **power-law sources**, the pair halos depend on two parameters of the source spectrum: The endpoint of the energy spectra E_2 and the photon index α. Again, the choice of the endpoint is critical as long as the endpoint is not large enough to allow interaction with the CMB. The other parameter that the pair halo depends on is the primary gamma photon index α. The effect of the photon index on the pair halo SEDs can be seen on the photon index of the pair halo gamma photons in the low energy region (LER) as shown in Fig. 4.5. The pair halo angular size also varies with respect to the primary gamma photon index where a lower photon index implies a smaller pair halo angular size. However, the pair halo angular size is similar when the observed energy is chosen to be higher ($E > 100$ GeV).

For **different redshift sources**, the pair halo SEDs from sources located at low redshift ($z < 1$) can give information about the CIB via their absorption features in the high energy region (HER) of the SED whereas the pair halo gamma photons from the high redshift sources in the HER are totally absorbed. It seems that suitable sources to observe the pair halo angular distribution

should be at redshift $z > 0.034$ because the pair halo angular sizes for sources at low redshift are very extended even for high energy observed gamma photons ($E > 1$ TeV). But also the source redshift should not be very high because the pair halo angular distribution will then be unresolved. However, in some models of the CIB (like Kneiske et al., 2002) an extended tail from the pair halo is present at large redshift ($z = 2$).

The **intensity of the CIB** affects directly the pair halo angular distribution. The pair halo angular sizes presented in Table 4.11 depend almost linearly on the intensity. The differential angular distribution of the pair halo gamma photons is not strongly different for different flux levels of the CIB when observed at low energies (10 GeV), but is quite different when the observed energy is increased to 100 GeV. This is explainable by the fact that the pair halo gamma photons suffer from the absorption on the CIB. This case is a good example to demonstrate that the pair halo angular distributions for the observed energy in the HER will give more information about the CIB than in the LER. Therefore, the pair halo angular distribution may be used to probe the intensity of the CIB.

The **differential models** describing the **CIB** and their evolution over redshift are very similar in their present day value. Even though the overall intensity of the CIB in these models is nearly the same, some differences of the shape of the SED are present. The pair halo SED seems to be more sensitive to the CIB shape than the pair halo angular distribution. For example, the pair halo angular sizes for different CIB models shown in Fig. 4.13 are nearly the same. The small remaining difference that can be seen in the differential angular distribution for high observed energies ($E > 100$ GeV), might be difficult to observe. It should be concluded here that the pair halo angular distribution is not a sensitive probe of the shape of the CIB.

However, the different CIB models at high redshift can be probed by the pair halo angular distribution. The CIBs at high redshift are rather different, they are quite model dependent and not constrained by the observed data. The intensity of the CIB depends on the cosmic star formation rate. In this work two different CIB models which have different intensities for larger redshift have been shown. The pair halo angular distributions look quite different and the pair halo angular sizes differ for the two models.

Halo Angular Size

The angular size of the pair halo provides information on the CIB around the VHE photon source, since the characteristic angular size at a certain gamma energy (E_γ) can be used to estimate the PP mean free path of their "grandparent" gamma photons [Aha01] ($\Lambda_{PP}(E_{\gamma 0})$). The average energy of these photons can be estimated as

$$E_{\gamma 0} \approx 2\sqrt{\frac{E_\gamma}{4kT_0}} \times m_e c^2 \tag{5.1}$$

where $T_0 = 2.7$ K Therefore, one can estimate the intensity of the CIB at the PP-resonant wavelength, as suggested by Aharonian (2001) [Aha01].

At different observed energies, an observer sees different halo sizes, and thus one can obtain information on the CBR at various wavelengths.

E_γ [GeV]	$E_{\gamma 0}$ [TeV]	$\Lambda_{PP}(E_{\gamma 0})$ [Mpc]
10	3.5	130
30	6	100
100	10	70
300	17	30
500	22	23
1000	30	10

Table 5.1: The observed gamma photon energy (E_γ), the corresponding "grandparent" photon energy ($E_{\gamma 0}$) in Eq.(5.1) and the PP mean free path of the "grandparent" photons.

Table 5.1 shows the photon energy at the observer sphere together with their corresponding "grandparent" photon energy and mean free path. Table 5.2 shows the pair halo angular size, $\Theta_{90\%}$, defined as the opening angle that contains 90% flux of the total halo flux. For this table a pair halo from a monoenergetic source with two different E_0-values at redshift $z = 0.129$ has been used together with Primack's CIB model.

E_γ [GeV]	E_0 = 100 TeV		E_0 = 500 TeV	
	$\Theta_{90\%}$ [degree]	$d \times \Theta_{90\%}$ [Mpc]	$\Theta_{90\%}$ [degree]	$d \times \Theta_{90\%}$ [Mpc]
10	13.8	152	13.9	153
30	9.8	107	9.2	101
100	4.6	50	4.6	50
300	1.4	15	1.95	21
500	0.58	6.3	1.26	13
1000	0.43	5	0.6	6

Table 5.2: The pair halo angular size for different energies, using a source distance of $d_s = 630$ Mpc ($z = 0.129$), and monoenergetic injection with E_0= 100 and 500 TeV.

The physical halo sizes estimated from Table 5.2 with the PP mean free path length of Table 5.1 are comparable, and very close when the observed gamma energy is low. For injection at $E_0 = 500$ TeV, one obtains a better estimate for the mean free path than in the case of injection at 100 TeV, especially at high energies.

H1426+428

H1426+428 is expected to be a TeV gamma source since, as predicted in the frame work synchrotron self-Compton scenario [C$^+$01], the X-ray peak at 100 keV implies of the broad Compton spectrum in the TeV energy region. Additionally, with its redshift of $z = 0.129$, the intergalactic absorption can start the cascade to form a pair halo. Recently, signals indicating intergalactic absorption of photons from H1426+428 have been reported [A$^+$02a, A$^+$03]. These measurements provide further evidence that this source might contain an observable pair halo.

In Fig. 5.1, the pair halo SED and angular distribution is plotted together with the sensitivity limit [Kon00] of a next generation IACT array, such as H.E.S.S., and demonstrates that a pair halo might be detected around H1426+428, if the gamma luminosity is 10^{45} erg/s or higher. Unfortunately, the gamma lu-

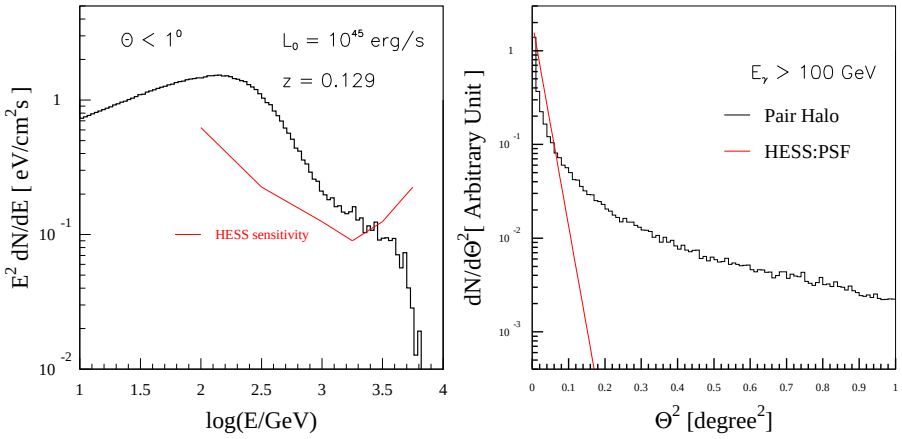

Figure 5.1: Left panel: (a) The pair halo SED from a monoenergetic source with $E_0 = 100$ TeV within 1° compared with the H.E.S.S. point source sensitivity. Right panel: (b) The corresponding pair halo angular distribution for gamma photon energy more than 100 TeV compared with the H.E.S.S. point spread function.

minosity of H1426+428 is most likely much lower than this isotropic value, since the source is believed to emit gamma-rays within a small solid angle, possibly as small as $10^{-2} - 10^{-4}$ sr , with a relativistic jet pointing towards the observer.

Generally speaking, it will probably be difficult to detect pair halos around TeV Blazars in the near future. However, since the intrinsic luminosity of these sources is uncertain, and since injected photon energies of several hundred TeV are totally absorbed by the CBR, one should not totally reject the possibility.

Chapter 6

Summary

In this work, the pair halo energy and angular distributions for many different parameters such as injected distributions, cosmic infrared background (CIB) models and redshifts were studied. A Monte Carlo method was employed to obtain these distributions from the pair halo.

The intergalactic medium (IGM) is not transparent to very high energy (VHE, $E > 100$ GeV) gamma-rays from extragalactic sources for which the propagation length is at the cosmological scale. Very high energy gamma-rays are absorbed by $\gamma\gamma$ pair production (PP) on the background photon field. However, the energy of the VHE gamma-rays is not lost because the resulting $e^{\pm}$ pair can interact with soft background photons via inverse Compton scattering (IC). Therefore, these two processes will take place again if the energy of the upscattered gamma photons is higher than the PP threshold energy. The sequence of PP and IC processes is called the electromagnetic cascade.

The $e^{\pm}$ pair halos are formed when the effect of magnetic fields on the electromagnetic cascade is taken into account. A magnetic field $|\mathbf{B}| > 10^{-9}$ G, which is required for the model, will isotropize the $e^{\pm}$ pairs from the cascade and hence the secondary gamma photons. Consequently, the cascade will develop as a halo around the VHE gamma photon source. The physical quantities related to observations are the gamma photon energy distribution and the angular distribution of the pair halo. Very high energy gamma-rays are absorbed by the soft background photons via PP and the PP mean free path length Λ_{PP} is much larger than that for IC (Λ_{IC}). The angular distribution should contain information about the background photon field around the source.

The background photon field of relevance for the cascade is composed of two components: The cosmic microwave background (CMB), which is the relic photon field from the Big Bang, and the cosmic infrared background (CIB) which mainly comprises photons from the formation of stars and from dust reemission. Therefore, the CIB contains information about the star formation history since the Big Bang. The CMB is known very well but the CIB is still relatively unknown. To directly observe the CIB is also quite difficult because of the dominant foreground radiation such as zodiacal light.

Because of the energy condition of PP, the VHE gamma photons are predominantly absorbed by the soft photons of the CIB. The characteristic properties of the CIB influence the development of the halo. Moreover, the CIB properties at the redshift of the source are accessible by observing halos.

To calculate the energy and angular distribution of the pair halo, Monte Carlo method, which allows a comprehensive analysis for an arbitrary form of the CIB has been chosen. The algorithm follows every particle in the cascade (gamma photon and $e^{\pm}$) until the upscattered photons travel very far from the observer, or the $e^{\pm}$ energies drop below a certain limit. The angular distance of the observed gamma photon can be calculated by using the reasonable assumption of spherical symmetry of the pair halo. The observer's sphere with radius equal to the source distance d_s where the VHE gamma source is located at the origin is produced. Whenever gamma photons cross this sphere, the angles between the propagation vector of the photons and the normal vector of the sphere at the crossing point are calculated. The normal vector of the observer's sphere can be interpreted as the line of sight of the observer. Therefore, the angles (θ) can be interpreted as the angular distance of the observed gamma photons. For high redshift sources ($z > 1$), the simulation scheme was modified because the z-dependence of the background during the development of the cascade is not negligible. In this case, the cascades are followed in a certain region around the source where the background can be assumed to be constant. To get the observed pair halo energy distribution and angular distribution, the PP attenuation factor ($\exp(d_s/\Lambda_{PP})$) is applied to the energy and angular distribution from the cascade in this region.

To study the pair halo in detail, three parameters that affect the pair halo were considered:

- **The primary gamma photon energy spectrum**: In the current work monoenergetic gamma rays (which are parametized by the injected photon energy E_0) and a power law (parameterized by a cutoff energy E_2 and photon index α) are used as study cases. The redshift $z = 0.129$ and the CIB model from Primack et al. (2000) [PSBD00] are the fixed quantities in this case.

  For the monoenergetic source study, the injected energies E_0 = 10, 100 and 500 TeV are the principle considered cases. The case of E_0 = 10 TeV could be considered as a single-generation cascade since the PP mean free path length at this energy (Λ_{PP}(10 TeV) $\approx$ 100 Mpc) is very large and the 2nd generation cascade will take place behind the observer. The single-generation case is the simplest case for the pair halo. Therefore it was used to formulate the angular distribution fitting function analytically. The function was modified to fit other angular distributions in the more complicated pair halo cascade. Studying the E_0 = 500 TeV case led to the conclusion that the pair halos from monoenergetic sources, with E_0 high enough to interact with CMB for a given redshift, will be independent of the primary gamma photon energy and behave like a pair halo from a power-law source with photon index 1.5. The fact that the pair halo

energy distributions and angular distributions are sensitive to the primary gamma photon energy in a certain range, for example in the study case $10 < E < 100$ TeV, is observed by comparison in these three cases.

For the power law source study, the cutoff energies used in the current work are the same as in the monoenergetic study which are $E_2 = 10$, 100 and 500 TeV (each case using photon index $\alpha = 2$). The conclusion from the E_2 study is similar to the monoenergetic study in that the pair halo depends on E_2 as long as E_2 is not large enough to allow interaction with the CMB. The photon indices used in the study ($\alpha = 1.5$, 2 and 2.5) show that the pair halo angular size is smaller when the photon indices are smaller.

- **The source distance d_s parametized by redshift z.** The redshifts used in the study are $z = 0.034$, 0.129 1 and 2. The fixed quantities are a monoenergetic ($E_0 = 100$ TeV) source spectrum and the Primack CIB model.

  The study shows that the pair halo SED gives information about the CIB when the redshift is not high ($z < 1$). The pair halo angular distributions are more centrally peaked for higher redshift. Moreover, the case $z = 0.034$ shows that the angular distributions are very extended even when observed energies are high ($E > 1$ TeV).

- **The background photon field (especially the CIB).** The effect on the pair halo from the CIB is considered in two cases. One is a scaling of the CIB intensity and the other is the use of different shapes of CIB from different models. In this study the monoenergetic $E_0 = 100$ TeV case is used.

  The Primack CIB model is scaled to different intensities, by a factor of one, three and ten. The results show that the pair halo angular size depends on the intensity quite linearly.

  The pair halo study for different CIB models are separated according to low and high redshift cases. At low redshift ($z = 0.129$), three CIB models are used: Primack et al. (2000), Malkan & Stecker (2001) [MS01] and Kneiske et al. (2002) [KMH02]. The results lead to the conclusion that the pair halo SEDs are more sensitive to the CIB shape than the angular distribution. At high redshift ($z = 2$), only the Primack et al. (2000) and Kneiske et al. (2001) models are used. The CIB from both models are quite different in both shape and intensity. The results show that the angular distribution for the Kneiske et al. (2002) CIB model is more extended than that derived using Primack et al. (2000).

In summary, the application of pair halo angular size at different observed energies to estimate the PP mean free path length of the gamma photons emitted from the source was discussed. Also, the detection possibility for pair halos from TeV blazar sources such as H1426+428 by the next generation IACT arrays such as H.E.S.S. was discussed.

Appendix A

Relevant Aspects of Cosmology

The fundamental Cosmological knowledge used in the current work will be briefly presented.

Robertson-Walker metric

Based on the cosmological postulate that the Universe is isotropic, homogeneous and uniformly expanding on a large scale, the Robertson-Walker metric is

$$ds^2 = c^2dt^2 - R(t)^2\left[\frac{dr^2}{1-kr^2} + r^2(d\theta^2 + \sin^2\theta d\phi^2)\right], \tag{A.1}$$

where r, θ and ϕ are the dimensionless Lagrange coordinates, and $R(t)$ is a scale factor which determines the radius of a curvature of the three-dimensional space. The constant k fixes the sign of the spatial curvature that is the same everywhere in space at a given time. The factor k can take on the values:

$k = 0$ corresponds to the Euclidean space,

$k = +1$ corresponds to the closed spherical or elliptical space of finite volume,

$k = -1$ corresponds to the hyperbolic space,

The coordinate (r, θ, ϕ) is called *the comoving coordinate* because they are constant for an object that is following the expansion of the Universe.

Cosmological Redshift

Consider the light reaching the observer O_0 located at $(0, \theta, \phi)$ at the present time t_0 from the source S_1 located at (r_1, θ, ϕ). Two crests arriving at t_0 and $t_0 + \Delta t_0$ were emitted at t_1 and $t_1 + \Delta t_1$. Because light travels in space-time along a null geodesic which means $ds^2 = 0$ in the Robertson-Walker metric (Eq.(A.1)), the consequent relation is

$$c\ dt = \pm R(t)\frac{dr}{\sqrt{1-kr^2}}. \tag{A.2}$$

Since r decreases as t increases along this null geodesic, the minus sign in the above relation is taken. It can be found that

$$\int_{t_1}^{t_0} \frac{c\ dt}{R(t)} = \int_{t_1+\Delta t_1}^{t_0+\Delta t_0} \frac{c\ dt}{R(t)} = \int_0^{r_1} \frac{dr}{\sqrt{1-kr^2}} \tag{A.3}$$

which implies that

$$\int_{t_1}^{t_0} \frac{c\ dt}{R(t)} - \int_{t_1+\Delta t_1}^{t_0+\Delta t_0} \frac{c\ dt}{R(t)} = 0. \tag{A.4}$$

It is reasonable that within a small time interval Δt_1 and Δt_2 the function $R(t)$ will not change. From the above relation and the fact that the term $c\ \Delta t_0$ and $c\ \Delta t_1$ can be chosen to correspond with wave length λ_0 and λ_1 respectively, it can be written

$$\frac{c\ \Delta t_0}{c\ \Delta t_1} = \frac{R(t_0)}{R(t_1)} = 1 + z, \tag{A.5}$$

where z is a redshift.

The cosmic time-redshift relation

In the Friedmann cosmological model with the cosmological constant $\Lambda = 0$ used in the current work, there are two equations describing the dynamic of the scale factor (see e.g. [Nar83, Lon98]):

$$\ddot{R} = -\frac{4\pi G\rho_0 R_0^3}{3R^2}, \tag{A.6}$$

and

$$\dot{R}^2 = \frac{8\pi G\rho_0 R_0^3}{3R} - k\ c^2, \tag{A.7}$$

where G is the gravitational constant, ρ_0 and R_0 are the total inertial mass density of the matter content of the Universe and the scale factor at the present epoch. Actually, these two equations can be explained by using Newtonian mechanics. One can see easily that Eq.(A.6) is the Newton's law of gravitational whereas Eq.(A.7) can be referred as the energy form of the Eq.(A.6).

It is convenient to represent these equations with some cosmological parameters such as: the present epoch Hubble constant

$$H_0 = \frac{\dot{R}_0}{R_0}, \tag{A.8}$$

the present epoch deceleration parameter

$$q_0 = -\frac{1}{H_0^2}\frac{\ddot{R}_0}{R_0}. \tag{A.9}$$

Consider Eq.(A.6) and (A.7) at present epoch one will easily get

$$\dot{R} = H_0 R_0 (1 + 2q_0 z)^{1/2} \tag{A.10}$$

and by applying the scale factor-redshift relation in Eq.(A.5) one can reach the cosmic time-redshift relation

$$\frac{dt}{dz} = -\frac{1}{H_0(1+z)^2(1+2q_0z)^{1/2}}. \tag{A.11}$$

Coordinate and Luminosity Distance (D_c & D_l)

Without loss of generality the coordinate can be adjusted so that the source S_1 is located at (r_1, θ, ϕ) and the observer O_0 is at $(0, \theta, \phi)$ in the comoving frame. The distance between S_1 and 0_0 in these coordinates is

$$D_c = R(t_0)\ r_1, \tag{A.12}$$

where D_c is the so-called coordinate distance. Now let us consider the simplest case, where the source S_1 emits monoenergetic photons, $E_{\varepsilon 1}$, with a luminosity L_1. There are two effects that affect the observed energy flux. One is the redshift of the observed photon, $E_{\varepsilon 0}$:

$$E_{\varepsilon 0} = \frac{E_{\varepsilon 1}}{(1+z)}. \tag{A.13}$$

The other effect is the difference of the time interval in the epoch of O_0 to S_1 by $(1+z)$ as in Eq.(A.5). Therefore, the observed flux that is observed at O_0 is given by

$$F_0 = \frac{L_1}{4\pi D_l^2}, \tag{A.14}$$

where

$$D_l = (1+z)D_c \tag{A.15}$$

is called the luminosity distance which is an observable quantity.

Angular size

Suppose a galaxy G_1 has a linear size d. Two null geodesics from the points A, B at the extremities of the galaxy G_1 directed toward the observer are considered. The points A and B have the polar coordinate (θ_1, ϕ_1) and $(\theta_1 + \Delta\theta_1, \phi_1)$ respectively. Since the homogeneity and isotropy assumptions are used, the observer is chosen to locate at $(0, 0, \pi)$.

According to the Robertson-Walker metric, the proper distance between A and B is obtained by putting $t = t_1 =$ constant, $r = r_1 =$ constant, $\phi = \phi_1 =$ constant, and $d\theta = \Delta\theta$ in Eq.(A.1). It will be

$$ds^2 = -r_1^2 R^2(t_1)(\Delta\theta)^2 = -d^2, \tag{A.16}$$

since in the rest frame of G_1 the space like separation $AB = d$. Thus

$$\Delta\theta_1 = \frac{d}{r_1 R(t_1)} = \frac{d(1+z)}{r_1 R(t_0)} \tag{A.17}$$

Notice that as r_1 increases the observers are looking at more and more remote galaxies, which must therefore be seen at earlier and earlier epochs t_1. However, $R(t_1)$ decreases at t_1 decreases, so it is not obvious that $r_1 R(t_1)$ should get progressively larger looking at more and more remote galaxies.

Appendix B

Angular Weighting Function

The method used in Sec. 3.3 works very well in order to find the observed angular distance θ for each pair halo gamma photon. However, the probability distribution for the angular distance obtained from that method is not a uniform distribution. A weighting function is needed to unify the distribution.

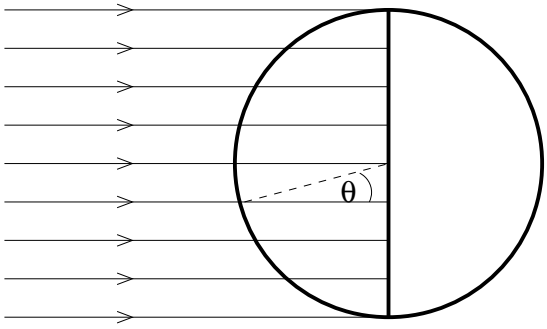

Figure B.1: The diagram shows the crossing points from homogenous fixed direction rays on an arc and a diameter. The crossing points uniformly distribute on the diameter but not on the arc. The diagram also shows that different points on the arc correspond to different angles.

The simplest case is the following: let the direction of the rays to be fixed. Then the angles depend on the positions on the sphere. The problem can be considered in two dimensions if one assumes the azimuthal symmetry. The angle θ depends on the position on the arc of the circle as shown in Fig. B.1. Consider the intersection point distributions of the homogenous rays with the arc,

$$\left(\frac{dN}{ds}\right)_{arc} = \frac{1}{r}\frac{dN}{d\theta}, \tag{B.1}$$

and the diameter of the circle,

$$\left(\frac{dN}{ds}\right)_{dia} = \frac{1}{r\cos\theta}\frac{dN}{d\theta} = \frac{1}{\cos\theta}\left(\frac{dN}{ds}\right)_{arc}, \tag{B.2}$$

It is obvious that the intersection points on the diameter are homogeneously distributed but not on the arc of the circle. Therefore, the distribution on the arc after weighted by the factor $cos^{-1}\theta$ will distribute homogeneously.

Actually, the factor $\left|\cos^{-1}\theta\right|$ is used as a weighting function instead of $\cos^{-1}\theta$. If the angular distribution is considered for small angle, this factor can be neglected since the factor can be approximated as unity. Figure B.2, for example, shows the pair halo angular distribution with and without the weighting function.

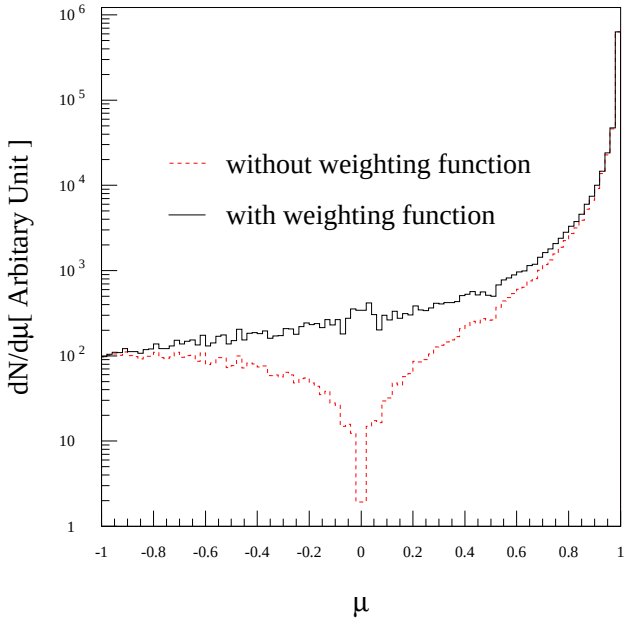

Figure B.2: The non-weighted pair halo angular distribution and the weighted one. Note: The angular distributions are presented in $\mu = \cos\theta$.

Appendix C

Angular Distribution Fitting

The simplest pair halo gamma photon angular distribution arises from the single-generation cascaded $e^{\pm}$s. These $e^{\pm}$ emit gamma photons via IC in the Thomson regime, and produce a large number of low energy gamma photons. Thus, for this case, the angular distribution of the pair halo gamma photons is proportional to the $e^{\pm}$ distribution which is a function of the primary gamma photon propagation distance. Then

$$\frac{dN_\gamma}{dr} \propto \frac{dN_e}{dr} = \frac{2}{\Lambda_{PP}} \exp(-r/\Lambda_{PP}(E_{\gamma_0})), \tag{C.1}$$

where E_{γ_0} is the primary gamma photon energy. The observed quantity is the column density of the gamma photons which scales with the column density of the cascaded $e^{\pm}$s. Consider the density of the $e^{\pm}$s surrounding the source first: the $e^{\pm}$s differential density distribution is

$$\begin{aligned} dN_e &= \frac{dN_e}{dr}\frac{dr}{dV}dV \\ &= \frac{2}{\Lambda_{PP}}\frac{\exp(-r/\Lambda_{PP})}{4\pi r^2}dV. \end{aligned} \tag{C.2}$$

At this stage cylindrical coordinates (ξ, z, ϕ) will be applied to calculate the column differential density:

$$dN_e = \frac{1}{\Lambda_{PP}} \int_{-\infty}^{\infty} dz \frac{\exp(-\sqrt{\xi^2+z^2}/\Lambda_{PP})}{(\xi^2+z^2)} \xi d\xi. \tag{C.3}$$

The integration is nontrivial. However, if the radius of the region being considered at the center of the halo is very small compared with the PP mean free path length, a first order approximation to the exponential can be applied, giving

$$\frac{dN_e}{d\xi} = \frac{1}{\Lambda_{PP}} \int_{-\infty}^{\infty} dz \frac{1}{(\xi^2+z^2)} \xi = \frac{\pi}{\Lambda_{PP}}. \tag{C.4}$$

If the observer is very far from the source, the angular distribution can be written in the form of projection radial distribution:

$$\begin{aligned} \frac{dN_e}{d\theta^2} &= \frac{dN_e}{d\xi}\frac{d\xi}{d\theta^2} \\ &= \frac{\pi d_s}{2\Lambda_{PP}\theta}. \end{aligned} \tag{C.5}$$

With the same assumption which leads to Eq.(C.1), the fitting function in this simple case becomes

$$\frac{dN_\gamma}{d\theta^2} = \frac{\alpha_1}{\theta} + \alpha_2, \tag{C.6}$$

where α_1 and α_2 are fitting parameters. In such a simple case the fitting parameters depend on the PP mean free path, Λ_{PP}. Figure C.1 shows two example distributions for monoenergetic gamma ray sources. In the first case, for $E_0 = 10$ TeV, $\Lambda_{PP} \approx 60$ Mpc and $\alpha_1 \approx 16.5$, the second case, for $E_0 = 5$ TeV, $\Lambda_{PP} \approx 120$ Mpc and $\alpha \approx 8.2$. The fit parameters are presented in Table C.1.

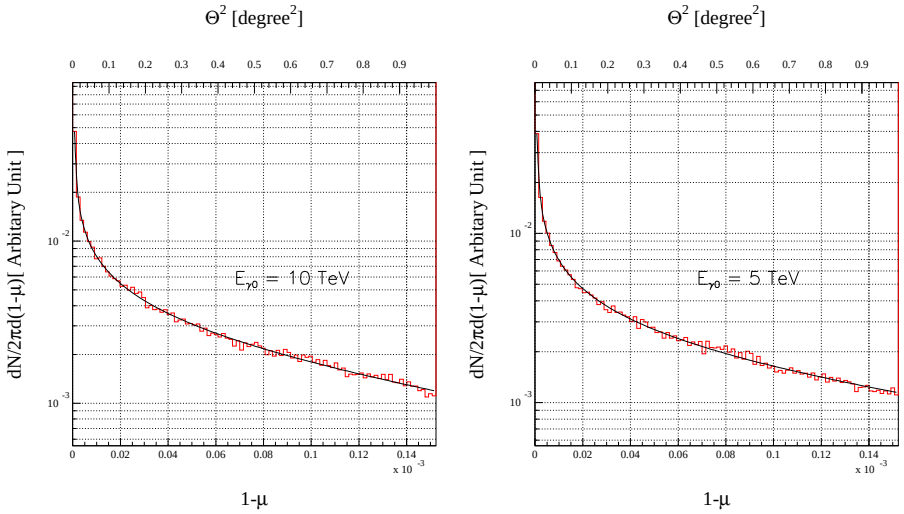

Figure C.1: The pair halo angular distribution for the case of monoenergetic primary gamma photons with $E_0 = 10$ TeV, (a), and $E_0 = 5$ TeV, (b), together with the fitting function are shown in left and right panel respectively.

The fitting parameters in Table C.1 depend on the PP mean free path of the primary gamma photon. In this example the PP mean free path of a photon with energy 5 TeV is larger than that of a 10 TeV photon by a factor of around two. The PP mean free path Λ_{PP}^{-1} has been included in the fitting parameters. Therefore, the fitting parameters for the 10 TeV case are larger than in the 5 TeV case by factor of two approximately.

E_0	α_1	α_2
10 TeV	15.144	-698.13
5 TeV	8.71	-347.98

Table C.1: Fitting parameters that fit the pair halo angular distribution normalized by total number for all angle in Fig. C.1(a) and (b).

Monoenergetic Sources					
Injected energy E_0	Observed energy E	a_1 ($\times 10^{-11}$)	a_2 ($\times 10^{-8}$	a_3 ($\times 10^{-5}$)	a_4 ($\times 10^{-3}$)
10 TeV	$>$ 10 GeV	0.475	-0.404	0.674	-0.280
	$>$ 100 GeV	0.418	-0.308	0.641	-0.256
	$>$ 1 TeV*	-1.161	1.708	-0.454	3.431
100 TeV	$>$ 10 GeV	0.496	1.481	0.121	-0.100
	$>$ 100 GeV	0.522	2.028	0.092	-0.012
	$>$ 1 TeV	0.214	3.100	-0.499	0.222
500 TeV	$>$ 10 GeV	3.248	-1.927	0.974	-0.547
	$>$ 100 GeV	4.029	-2.266	0.954	-0.561
	$>$ 1 TeV	5.573	-2.967	0.848	-0.518

Table C.2: Fitting parameters for the pair halos differential angular distributions in Fig. 4.6(a), (b) and (c). Note that the fitting parameters are calculated based on the differential angular distribution normalized within 1°.

In the other cases the situation is more complicated; e.g., when there are many cascade generations within the considered region, or when the primary gamma photons are not monoenergetic. Then the fitting function is not easy to find. However, by comparing the pair halo photon angular distribution for many cases with this simple case one is lead to the conclusion that for the case of many cascade generations developing in the center of the halo, a higher exponent for θ^{-n} is required. On the other hand, the additional terms make the tail of the distribution drop faster, and therefore some compensation terms are required. Fortunately, the fitting function for the complicated scenario can be fitted by adding empirical term of as follows:

$$\frac{dN_\gamma}{d\theta^2} = \frac{a_1}{\theta^3} + \frac{a_2}{\theta} + a_3 + a_4\theta. \tag{C.7}$$

From this fitting equation, most of the pair halo gamma photon angular distribution within 1° can be accurately fitted.

The Table C.2-C.5 summarize the fitting parameters of the pair halo differential angular distributions for many different parameters as shown in the Ch. 4.

Power-law Sources					
Photon index α	Observed energy E	a_1 ($\times 10^{-11}$)	a_2 ($\times 10^{-8}$)	a_3 ($\times 10^{-5}$)	a_4 ($\times 10^{-3}$)
1.5	$>$ 10 GeV	0.159	0.281	0.294	-0.173
	$>$ 100 GeV	0.263	0.291	0.289	-0.194
	$>$ 1 TeV	0.203	0.596	0.198	-0.180
2.0	$>$ 10 GeV	0.247	0.052	0.332	-0.175
	$>$ 100 GeV	0.239	0.214	0.290	-0.177
	$>$ 1 TeV	0.061	0.695	0.152	-0.138
2.5	$>$ 10 GeV	0.230	-0.008	0.356	-0.164
	$>$ 100 GeV	0.191	0.193	0.311	-0.170
	$>$ 1 TeV	0.073	0.741	0.119	-0.096

Table C.3: Fitting parameters for the pair halos differential angular distributions in Fig. 4.8(a), (b) and (c). Note that the fitting parameters are calculated based on the differential angular distribution normalized within 1°.

Redshifts					
Redshift z	Observed energy E	a_1 ($\times 10^{-11}$)	a_2 ($\times 10^{-8}$)	a_3 ($\times 10^{-5}$)	a_4 ($\times 10^{-3}$)
0.034	$>$ 10 GeV	0.298	0.104	0.650	-0.261
	$>$ 100 GeV	0.317	0.142	0.653	-0.288
	$>$ 1 TeV	0.351	0.144	0.661	-0.311
0.129	$>$ 10 GeV	0.496	1.481	0.121	-0.100
	$>$ 100 GeV	0.522	2.028	0.092	-0.012
	$>$ 1 TeV	0.214	3.100	-0.499	0.222
1.0	$>$ 10 GeV	30.199	-6.228	2.276	-1.340
	$>$ 100 GeV	50.551	-23.526	4.143	-2.111
2.0	$>$ 10 GeV	22.758	-9.073	1.707	-0.882

Table C.4: Fitting parameters for the pair halos differential angular distributions in Fig. 4.15(a), (b) and (c). Note that the fitting parameters are calculated based on the differential angular distribution normalized within 1°.

CIB					
CIB	Observed energy E	a_1 ($\times 10^{-11}$)	a_2 ($\times 10^{-8}$)	a_3 ($\times 10^{-5}$)	a_4 ($\times 10^{-3}$)
Primack et al.	$>$ 10 GeV	0.496	1.481	0.121	-0.100
	$>$ 100 GeV	0.522	2.028	0.092	-0.012
	$>$ 1 TeV	0.214	3.100	-0.499	0.222
3$\times$ Primack et al.	$>$ 10 GeV	2.459	-0.731	0.532	-0.291
	$>$ 100 GeV	3.290	-0.775	0.345	-0.186
10$\times$ Primack et al.	$>$ 10 GeV	2.710	-1.215	0.642	-0.372
	$>$ 100 GeV	4.677	-2.771	0.825	-0.488
Malkan & Stecker	$>$ 10 GeV	0.338	1.147	0.324	-0.232
	$>$ 100 GeV	0.291	1.715	0.129	-0.161
	$>$ 1 TeV	0.179	2.316	-0.088	-0.066
Kneiske et al.	$>$ 10 GeV	0.937	1.333	0.055	-0.038
	$>$ 100 GeV	1.130	1.761	-0.150	0.499
	$>$ 1 TeV	0.941	2.670	-0.524	0.278

Table C.5: Fitting parameters for the pair halos differential angular distributions in Fig. 4.19(a) and (b) and Fig. 4.23(a), (b) and (c). Note that the fitting parameters are calculated based on the differential angular distribution normalized within 1°.

Bibliography

[A+97a] F. A. Aharonian et al. H.E.S.S. (High Energy Stereoscopic System) letter of intent. Technical report, Max-Planck-Institut für Kernphysik, 1997.

[A+97b] F. A. Aharonian et al. The potential of ground based arrays of imaging atmospheric Cherenkov telescopes. I. Determination of shower parameters. *Astroparticle Phys.*, 6:343–371, 1997.

[A+98] R. G. Arendt et al. The COBE diffuse infrared background experiment search for the cosmic infrared background. III. separation of galactic emission from the infrared sky brightness. *ApJ*, 508:74–105, 1998.

[A+99] F. A. Aharonian et al. The time averaged TeV energy spectrum of mkn501 of the extraordinary 1997 outbust as measured with the stereoscopic cherenkov telescope system of hegra. *Astron. Astrophys.*, 349:11–28, 1999.

[A+02a] F. A. Aharonian et al. TeV gamma rays from the Blazer H1426+428 and the diffuse extragalactic background radiation. arXiv:astro-ph/0202072v1, Febuary 2002.

[A+02b] F. A. Aharonian et al. An unidentified TeV source in the vicinity of Cygnus OB2. *A&A*, 393:L37–L40, 2002.

[A+03] F. A. Aharonian et al. Observations of H1426+428 with HEGRA reanalysis of 1999&2000 data, observations in 2002. arXiv:astro-ph/0301437 v1, January 2003.

[AA81] F. A. Aharonian and A. M. Atoyan. Compton scattering of relativistic electrons in compact x-ray sources. *Astrophys. Space Sci.*, 79:321–336, 1981.

[AA91] F. A. Aharonian and A. M. Atoyan. Cosmic ray positrons connected with galactic gamma radiation of high and very high energies. *J. Phys. G: Nucl. Part. Phys.*, 17:1769–1778, 1991.

[AA97] F. A. Aharonian and C. W. Akerlof. Gamma-ray astronomy with imaging atmospheric Čerenkov telescopes. *Rev. Nucl. Part. Sci.*, 47:273–314, 1997.

[AAN83] F. A. Aharonian, A. M. Atoyan, and A. M. Nagapetian. Photoproduction of electron-positron pairs in compact x-rays sources. *Astrofizika*, 19:187–194, 1983.

[AB65] A. I. Akhiezer and V. B. Berestetskii. *Quantum Electrodynamics.* Interscience Publishers, New York, 1965.

[ACV94] F. A. Aharonian, P. S. Coppi, and H. J. Völk. Very high energy gamma rays from active galactic nuclei: Cascading on the cosmic background radiation field and the formation of pair halos. *ApJ*, 423:L5–L8, 1994.

[Aha01] F. A. Aharonian. TeV Blazars and cosmic infrared background radiation. arXiv:astro-ph/0112314 v1, December 2001.

[AKUV85] F. A. Aharonian, V. G. Kirillov-Ugryumov, and V. V. Vardanian. Formation of relativistic electron-photon showers in compact x-ray sources. *Astrophys. Space Sci.*, 115:201–225, 1985.

[BG70] G. R. Blumenthal and R. J. Gould. Bremsstrahlung, synchrotron radiation, and compton scattering of high-energy electrons traversing dilute gases. *Rev. Mod. Phys.*, 42:237–269, 1970.

[Bla48] P. M. S. Blackett. Physical Society of London Gassiot Committee Report, 1948.

[Bo03] K Bernloöhr and other. The optical system of the H.E.S.S. imaging atmospheric Cherenkov telescopes Part I: layout and components of the system. http://www.mpi-hd.mpg.de/hfm/HESS/HESS.html, 2003.

[C+65] A. E. Chudakov et al. In D. V. Skobel'tsyn, editor, *Cosmic Rays, Proceedings of the P. N. Lededev Physics Institute*, volume 26, page 100, 1965.

[C+01] L. Costamante et al. Extreme synchrotron BL Lac objects stretching the blazar sequence. *A&A*, 317:512–526, 2001.

[C+03] R. Cornils et al. The optical system of the H.E.S.S. imaging atmospheric Cherenkov telescopes Part II: mirror alignment and point spread function. http://www.mpi-hd.mpg.de/hfm/HESS/HESS.html, 2003.

[CB90] P. S. Coppi and R. D. Blandford. Reaction rates and energy distributions for elementary processes in relativistic pair plasmas. *Mon. Not. R. astr. Soc.*, 245:453–469, 1990.

[Coc60] G. Cocconi. In B. A. Khrenov, editor, *Proc. Moscow Cosmic Ray Conf.*, page 309, 1960.

[D+97] A. Daum et al. First results on the performance of the HEGRA IACT array. *Astroparticle Phys.*, 8:1–11, 1997.

[D+98] E. Dwek et al. The COBE diffuse infrared background experiment search for the cosmic infrared background. IV. cosmological implications. *ApJ*, 508:106–122, 1998.

[DA+02] Arache Djannati-Ataï et al. Detection of the BL Lac object 1ES 1426+428 in the very high energy gamma-rays band by the CAT telescope from 1998-2000. arXiv:astro-ph/0207618, July 2002.

[E+02] D. Elbaz et al. The bulk of the cosmic infrared background resolved by ISOCAM. *A&A*, 384:848–865, 2002.

[F+68] G. G. Fazio et al. *Can. J. Phys.*, 46:S451, 1968.

[F+94] C. E. Fichtel et al. The first energetic gamma-ray experiment telescope (EGRET) source catalog. *ApJS*, 94:551–581, 1994.

[GJ53] W. Galbraith and J. V. Jelley. *Nature*, 171:349, 1953.

[GS66] R. J. Gould and G. Schréder. Opacity of the universe to high-energy photons. *Phys. Rev. Lett.*, 155:252–254, 1966.

[GS67] R. J. Gould and G. Schréder. Pair production in photon-photon collisions. *Phys. Rev.*, 155:1404–1407, 1967.

[H+99] R. C. Hartman et al. The third EGRET catalog of high-energy gamma-ray sources. *ApJS*, 123:79–202, 1999.

[H+02] D. Horan et al. Detection of the BL Lacertae object H1426+428 at TeV gamma-ray energies. *ApJ*, 571:753–762, 2002.

[Hal70] J. H. Halton. A retrospective and prospective survey of the Monte Carlo method. *Siam Rev.*, 12:1–63, 1970.

[HD01] M. G. Hauser and E. Dwek. The cosmic infrared background: Measurements and implications. *ARA&A*, 39:249, 2001.

[Her74] K. Herterich. Absorption of gamma rays in intense x-rays sources. *Nature*, 250:311–312, 1974.

[Hes12] V. F. Hess. Observation of penetrating radiation of seven ballon flights. *Physikalische Zeitschrift*, 13:1084, 1912.

[Hil85] A. M. Hillas. In *Proc. 19th ICRC (La Jolla)*, volume 3, page 445, 1985.

[Hil96] A. M. Hillas. Differences between gamma-ray and hadronic showers. *Spa. Sci. Rev.*, 75:17–30, 1996.

[Hor00] D. Horns. *Suche nach TeV-Photonen aus intergalaktischen Kasdaden und nach Bose-Einstein-Kondensaten in TeV-Photonen.* PhD thesis, Universität Hamburg, 2000.

[Jam80] F. James. Monte carlo theory and practice. *Rep. Prog. Phys.*, 43:1145–1189, 1980.

[K+98] T. Kelsall et al. The COBE diffuse infrared background experiment search for the cosmic infrared background. II. model of the interplanetary dust cloud. *ApJ*, 508:44–73, 1998.

[Kha03] D. Khangulyan. *Space structure and spectrum of radiation of some astrophysical objects.* PhD thesis, Moscow engineering physics institute, 2003.

[KK03] S. Kelner and D. Khangulyan. Electomagnetic halos of AGNs. In *Science session of MEPhI-2003*, page 182, 2003.

[KMH02] T. M. Kneiske, K. Mannheim, and D. H. Hartmann. Implications of cosmological gamma-ray absorption 1. evolution of the metagalactic radiation field. arXiv:astro-ph/0202104 v1, February 2002.

[Kon00] A. K. Konopelko. Stereo imaging of the VHE γ-rays with HEGRA & H.E.S.S. In F. A. Aharonian and H. J. Völk, editors, *High Energy Gamma-ray Astronomy*, pages 569–573, 2000.

[L+92] Y. C. Lin et al. Detection of high-energy gamma-rays emission from the BL Lacertae object Markarian 421 by the EGRET telescope on the Compton Observatory. *ApJ*, 401:L61–L64, 1992.

[Lee98] S. Lee. Propagation of extragalactic high energy cosmic and γ rays. *Phys. Rev. D.*, 58:043004, 1998.

[LJM86] F. J. Lockman, K. Jahoda, and D. McCammon. The structure of galactic hi in directions of low total column density. *ApJ*, 302:432–449, 1986.

[Lon98] M. S. Longair. *Galaxy Formation*, chapter 7. Springer, Germany, 1998.

[Mat58] W. Mattig. Über den Zusammenhang zwischen Rotverschiebung und scheinbarer Helligkeit. *Astron. Nach.*, 248:109, 1958.

[Mat99] T. Matsumoto. Near infrared extragalactic background. In D. Lemke, M. Stickel, and K. Wilke, editors, *ISO Surveys of a Dusty Universe*, pages 96–105, 1999.

[MD+02] M.-A. Miville-Deschênes et al. Power spectrum of the cosmic infrared background at 60 and 100 μm with iras. *A&A*, 393:749–756, 2002.

[Mir02] R. Mirzoyan. The future of the MAGIC project: Phase II. Talk at the Univ. Tokyo Workshop 2002, September 2002.

[Mor58] P. Morrison. *Nuovo Cim.*, 7:858, 1958.

[Mor00] M. Mori. Status of the CANGAROO-III project. In F. A. Aharonian and H. J. Völk, editors, *High Energy Gamma-Ray Astronomy*, pages 578–581, 2000.

[MS01] M. A. Malkan and F. W. Stecker. An empirically based model for predicting infrared luminosity functions, deep infrared galaxy counts and the diffuse infrared background. arXiv:astro-ph/0009500 v4, February 2001.

[MW86] P. V. Ramana Murthy and Wolfendale. *Gamma-ray astronomy.* Cambridge University Press, England, first edition, 1986.

[N+94] M. Noda et al. Near-infrared spectrometer on the infrared telescope in space. *ApJ*, 428:363–369, 1994.

[Nar83] J. V. Narlikar. *Introduction to cosmology.* Jones and Bartlett Publishers, U.S.A., first edition, 1983.

[Nik62] P. N. Nikishov. Absorption of high-energy photons in the universe. *Soviet Phys. JETP*, 14:393–394, 1962.

[O+03] R. A. Ong et al. The VERITAS project. arXiv:astro-ph/0302610v1, March 2003.

[P+92] M. Punch et al. Detection of TeV photons from the active galaxy Markarian 421. *Nature*, 358:477–478, 1992.

[Pro86] R. J. Protheroe. Effect of electron-photon cascading on the observed energy spectra of extragalactic sources of ultra-high-energy γ-rays. *Mon. Not. R. astr. Soc*, 221:769–788, 1986.

[PSBD00] J. R. Primack, R. S. Somerville, J. S. Bullock, and J. E. G. Devriendt. Probing galaxy formation with high energy gamma-rays. In F. A. Aharonian and H. J. Völk, editors, *High Energy Gamma-Ray Astronomy*, 2000.

[PTVF94] W. H. Press, S. A. Teukolsky, W. T. Vetterling, and B. P. Flannery. *Numerical Recipes in C.* Cambridge university press, New York, second edition, 1994.

[Q+96] J. Quinn et al. Detection of gamma rays with E> 300 GeV from Markarian501. *ApJ*, 456:L83–L86, 1996.

[RBLP01] C. Renault, A. Barrau, G. Lagache, and J.-L. Puget. New constraints on the cosmic mid-infrared background using tev gamma-ray astronomy. *A&A*, 371:771–778, 2001.

[SJS92] F. W. Stecker, O. C. De Jager, and M. H. Salamon. *ApJ*, 390:L49, 1992.

[T+95] D. J. Thompson et al. The second EGRET catalog of high-energy gamma-ray sources. *ApJS*, 101:259–286, 1995.

[Ter77] J. Terrell. The luminosity distance equation in fiedmann cosmology. *Am. J. Phys.*, 45:869–867, 1977.

[TW78] K. E. Turver and T. C. Weekes. *Nuovo Cim.*, 45B:99, 1978.

[V+91] G. Vacanti et al. Gamma-ray observations of the crab nebula at TeV energies. *ApJ*, 377:379–395, 1991.

[W+89] T. C. Weekes et al. Observation of TeV gamma rays from the crab nebula using the atmospheric čerenkov imaging technique. *ApJ*, 342:379–395, 1989.

[W+92] R. J. Wainscoat et al. A model of the 8-25 micron point source infrared sky. *ApJS*, 83:111–146, 1992.

[WC96] E. Waxman and P. Coppi. Delayed GeV-TeV photons from gamma-ray bursts producing high-energy cosmic rays. *ApJ*, 446:L75–L78, 1996.

[WTW72] J. Wdowczyk, A. Tkaczyk, and A. W. Wolfendale. *J. Phys. A.*, 5:1419, 1972.

[Zdz88] A. A. Zdziarski. Saturated pair-photon cascades on isotropic background photons. *ApJ*, 335:786–802, 1988.